UNIVERSITEIT VAN PRETORIA
UNIVERSITY OF PRETORIA
YUNIBESITHI YA PRETORIA

Novel solid phase synthesis of a visible-light-active p-n heterojunction CuS/ZnS photocatalyst for wastewater treatment applications

by

Rachel Mugumo

A dissertation submitted in partial fulfilment of the requirements for the degree.

Master of Science (Applied Science)

Environmental Engineering Technology

in the

Department of Chemical Engineering

Faculty of Engineering, the Built Environment, and Information Technology

University of Pretoria

2023

© University of Pretoria

ABSTRACT

Title:	**Novel solid phase synthesis of a visible-light-active p-n heterojunction CuS/ZnS photocatalyst for wastewater treatment applications**
Author:	Rachel Mugumo
Supervisor:	Professor Evans M.N. Chirwa
Co-supervisor:	Professor Shepherd M. Tichapondwa
Department:	Chemical Engineering
University:	University of Pretoria
Degree:	Master of Science (Environmental Engineering Technology)

Water contamination by toxic organic chemicals is a major global environmental concern leading to photocatalytic technologies applied in wastewater treatment. The aim of this work was to investigate a new, simple one-pot combustion synthesis technique for creating sulphur-based CuS/ZnS p-n heterojunction nanocomposite photocatalysts. The study examined the photocatalytic activity and reusability of these nanocomposites in removing rhodamine B (RhB) dye from aqueous systems under visible light irradiation. Rhodamine B is an azo dye that is widely applied in processing operations such as the colouring process in textile industries which provides significant socioeconomic benefits; however, its minute traces in water antagonistically affect the environment and all life forms.

In this study, a novel heterointerface strategy is proposed for synthesising p-n heterojunction nanoporous agglomerate nanocomposites. This approach involves a simple one-pot one-step combustion method to that attunes the morphology and band gap energy of visible-light-induced nanomaterials. Various characterisation techniques were employed to analyse the physicochemical properties of the synthesised nanocomposite materials. X-Ray Diffraction (XRD) was used to ascertain the crystallinity and purity of the synthesised materials, while X-Ray Fluorescence (XRF) was utilised to determine the composition of the photocatalyst. To confirm the morphology and elemental chemical composition of the synthesised materials,

© University of Pretoria

Scanning Electron Microscopy (SEM), Transmission Electron Microscopy (TEM), and Energy-Dispersive X-Ray Spectroscopy (EDS) were conducted. Braunauer-Emmett-Teller (BET) analysis was employed to measure the surface area and pore size distribution of the materials. Furthermore, the optical properties, including the photo absorption range and band gap energy of the synthesised nanocomposite materials, were determined using Ultraviolet-Visible spectroscopy (UV-vis).

Several intrinsic reaction parameters affecting the photodegradation process were systematically varied to determine the optimal conditions, including the catalyst composition (CuS, ZnS, and CuS/ZnS), catalyst loading (ranging from 0 to 15 gL^{-1}), initial solution pH (ranging from 1 to 13), and initial pollutant concentration (varying from 5 to 100 ppm). The experimental findings revealed that a binary CuS/ZnS catalyst, loaded at 10 gL^{-1} and with a pH of 5, achieved an impressive 97 % degradation of a 5 ppm RhB dye following 270 minutes of visible light exposure. These results highlighted the significant enhancement in photocatalytic degradation efficiency when pristine ZnS is coupled with highly photosensitive CuS. Specifically, the degradation efficiency improved from 67 % to 97 % within 4 hours of solar irradiation.

Moreover, it is noteworthy that the Langmuir-Hinshelwood kinetic model demonstrated the best fit to the data when a loading of 10 gL^{-1} was employed, yielding an impressive R^2 value of 0.99 and a maximum rate constant (k_{max}) value of 0.0186 min^{-1} indicative of pseudo-first-order kinetics rates. Additionally, this composite catalyst exhibited remarkable chemical stability and reusability, as it achieved 83 % RhB dye removal after five recycling runs. Further investigations involving scavenger tests identified the photogenerated holes (h^+) and superoxide free radicals ($\bullet O_2$) as the primary reactive species responsible for degradation process. This comprehensive study provides valuable insight into the design of highly efficient nanomaterials for removing organic pollutants from wastewater, and a possible reaction mechanism is proposed.

Keywords: photodegradation, organic pollutants, textile wastewater, photocatalyst, p-n heterojunction, combustion method, rhodamine B dye, visible light irradiation

© University of Pretoria

DECLARATION

I, RACHEL MUGUMO, hereby declare that all the work provided in this dissertation is to the best of my knowledge original (except where cited) has neither in whole nor in part, been submitted for another degree at this or any other University or tertiary education institution or examining body.

SIGNATURE: ……

DATE: …21/12/2023……..

© University of Pretoria

DEDICATION

To my loving and world best parents,

Mr Menard Mugumo and Mrs Sofia Mugumo

For their endless love, support, trust, and prayers.

To my siblings who are family and more,

Einstein Mugumo, Priscilla Mugumo, Viola Mugumo and nephew, Hughan Mugumo

For always believing in me and being my greatest cheerleaders.

© University of Pretoria

ACKNOWLEDGEMENT

First and foremost, I would like to thank the Lord God Almighty for rooting my identity in Him and beginning a good work in me, for I am convinced beyond a shadow of doubt that He's bringing it to fruition. I stand in awe of Him as I reminisce all the God-stops we've shared, shutting doors nobody can open and opening doors no one can shut (this one included). The journey has been nothing short of purposeful. I have grown intellectually, emotionally, and most importantly spiritually.

I would like to acknowledge and extend my heartfelt gratitude to my supervisor, Prof. Evans M.N. Chirwa and co-supervisor, Prof. Shepherd Tichapondwa for their ever willingness and readiness to guide me, coach me in their excellent expertise and unwavering academic support through their patience, redirection, and words of encouragement towards my success. Your relentless efforts, assistance, kindness and hard work is most truly and highly appreciated. Many thanks to my supervisors for funding my studies throughout the course of my research. This research was funded by National Research Fund (NRF) of South Africa, grant number EQP180503325881 awarded to Prof Evans M. Nkhalambayausi Chirwa, The NRF Thuthuka Grant grant number TTK18024324064 awarded to Prof Shepherd Tichapondwa and Rand Water Chair in Water Utilisation, grant number RW01413/18.

I would like to thank Mrs Elmarie Otto for her motherly concern and Mrs Alette Devega for attending to all my laboratory needs in order to smooth sail my research. I would also like to extend my gratitude to all the Water Utilisation and Environmental research group members especially Dr. Samuel Iwarere and Emmanuel O. Ichipi for their relentless advice, support, and assistance.

A special thanks to my loving parents for their unceasing prayers, love, and support through this journey. My immerse gratitude to my loving and caring siblings, Viola, Einstein, Priscilla and nephew, Hughan for believing in me and cheering me on.

© University of Pretoria

Last, but not least, I would like to extend my heartfelt gratitude to all my friends and well-wishers for directly and/or indirectly supporting me throughout this journey.

© University of Pretoria

TABLE OF CONTENTS

ABSTRACT....ii
DECLARATION....iv
DEDICATION....v
ACKNOWLEDGEMENT....vi
TABLE OF CONTENTS....viii
LIST OF FIGURES....xi
LIST OF TABLES....xiii
RESEARCH OUTPUTS....xvii
CHAPTER 1: INTRODUCTION....1
1.1 Background....1
1.2 Aims and objectives....4
1.3 Study significance....4
1.4 Dissertation scope....5
CHAPTER 2: LITERATURE REVIEW....7
2.1 Organic pollutants....7
2.2 Current water treatment techniques and their drawbacks....10
2.3 Advanced Oxidation Processes....11
2.3.1 Factors Affecting Photocatalysis....11
2.3.1.1 Effect of catalyst loading....11
2.3.1.2 Effect of initial pH....12
2.3.1.3 Effect of initial pollutant concentration....12
2.3.1.4 Effect of light intensity....12
2.3.2 Homogeneous photocatalysis....13
2.3.3 Heterogeneous photocatalysis....14
2.3.3.1 Semiconductor photocatalysis....14

© University of Pretoria

2.3.3.2 Photocatalysis drawbacks and solutions 16
2.4 Strategies for optimising charge separation efficiency 16
2.4.1 Metal/semiconductor heterostructure nanocomposites 16
2.4.2 Coupled semiconductor/semiconductor heterostructure nanocomposites 17
2.5 Heterojunction photocatalysts 20
2.5.1 p-n heterojunction photocatalysts 20
2.5.2 Metal-sulphide -based heterojunction photocatalysts 23
2.5.2.1 ZnS photocatalyst 25
2.5.2.2 CuS photocatalyst 27
2.5.2.3 CuS/ZnS photocatalyst 29
CHAPTER 3: MATERIALS AND METHODS 31
3.1 Materials 31
3.2 Catalyst synthesis 31
3.3 Characterisation 32
3.3.1 X-Ray Diffraction analysis (XRD) 32
3.3.2 X-Ray Fluorescence analysis (XRF) 33
3.3.3 Scanning Electron Microscopy and Energy Dispersive Spectroscopy (SEM/EDS) 33
3.3.4 Transmission Electron Microscopy (TEM) 33
3.3.5 Brunauer-Emmett-Teller (BET) 34
3.3.6 Ultraviolet-Visible Spectrophotometer (UV-Vis) 34
3.4 Analytical methods 34
3.4.1 UV-Vis spectrophotometer 34
3.5 Degradation studies 36
CHAPTER 4: PHOTOCATALYSTS CHARACTERISATION 38
4.1 Catalyst Phase Analysis 38
4.2 Elemental composition 39
4.3 Catalyst morphology 40

© University of Pretoria

4.3 Elemental mapping and distribution analysis....41
4.4 Surface area and pore size analysis....42
4.4 Photo-absorption and band gap analysis....44
4.4.1 Optical band gap measurement....45
CHAPTER 5: DEGRADATION IN-DEPTH STUDIES....48
5.1 Visible light photodegradation study....48
5.2 Photocatalytic performance....49
5.2.1 Effect of individual catalyst composites....50
5.2.2 Effect of initial pH....51
5.2.3 Effect of catalyst loading....53
5.2.4 Effect of initial rhodamine B concentration....55
5.3 Radical scavenging test....56
5.4 Photocatalytic mechanism....58
5.5 Catalyst recyclability....60
CHAPTER 6: CONCLUSIONS AND RECOMMENDATIONS....63
REFERENCES....64

© University of Pretoria

LIST OF FIGURES

Figure 1.1: Research study plan outline. 6

Figure 2.1: The molecular structure of rhodamine B dye. 8

Figure 2.2: Textile industry: wastewater effluent generation, toxicity, and treatment techniques 9

Figure 2.3: Operational parameters influencing the photocatalytic degradation of organanopollutants. 13

Figure 2.4: Basic schematic representation of photocatalytic degradation mechanism of organic pollutants under light irradiation. 15

Figure 2.5: Schematic energy band forms of semiconductor heterojunctions (a) type-I, (b) type-II, and (c) type-III 18

Figure 2.6: Schematic coupled heterostructure composites charge transfer illustration. 19

Figure 2.7: Schematic illustration of the energy band structure and electron-hole pair separation in the p-n heterojunction. 21

Figure 2.8: Metal sulphides advantages in photocatalytic applications. 23

Figure 3.1: Solid phase one – pot CuS/ZnS catalyst synthesis. 32

Figure 3.2: Calibration curve for rhodamine B dye detection. 35

Figure 4.1: XRD patterns of the pristine ZnS and CuS as well as the CuS/ZnS composite. 39

Figure 4.2: SEM images of (a) ZnS, (b) CuS, and (c) CuS/ZnS, and TEM images of (d) ZnS, (e) CuS, and (f) CuS/ZnS. 41

Figure 4.3: EDS elemental analysis and mapping of (a) ZnS, (b) CuS, and (c) CuS/ZnS. 42

Figure 4.4: N_2 adsorption – desorption isotherm of synthesised catalysts. 44

Figure 4.5: UV – vis absorption spectra of synthesised nanoparticles. 45

Figure 4.6: Tauc plot and estimated band gap for ZnS. 46

© University of Pretoria

Figure 4.7: Tauc plot and estimated band gap for CuS. 47

Figure 4.8: Tauc plot and estimated band gap for CuS/ZnS. 47

Figure 5.1: Solar spectrum with respective wavelengths..... 48

Figure 5.2: Control tests and photocatalysis of CuS/ZnS under visible light irradiation. 49

Figure 5.3: Performance of 10 gL^{-1} constituent catalyst on 5 ppm rhodamine B dye solution. 51

Figure 5.4: Reaction kinetics and effect of initial pH in rhodamine B dye degradation with CuS/ZnS photocatalyst..... 53

Figure 5.5: Reaction kinetics and effect of catalyst loading in rhodamine B dye degradation with CuS/ZnS photocatalyst. 54

Figure 5.6: Reaction kinetics and effect of catalyst loading in rhodamine B dye degradation with CuS/ZnS photocatalyst. 56

Figure 5.7: Effect of BA, IPA, EDTA – 2Na and pBZQ scavengers rhodamine B dye degradation efficacy using CuS/ZnS photocatalyst. 57

Figure 5.8: Proposed schematic representation of a p-n CuS/ZnS heterojunction photocatalytic mechanism. 59

Figure 5.9: Stability and recyclability of CuS/ZnS photocatalyst during 5 cycles. 61

Figure 5.10: (a) Zoomed-out and (b) zoomed-in CuS/ZnS SEM images before use and (c) zoomed-out and (d) zoomed-in CuS/ZnS SEM images after 5 recycles. 62

© University of Pretoria

LIST OF TABLES

Table 2.1: Some p-type and n-type semiconductors with their respective crystal structures and band gaps (eV). 22

Table 2.2: Comparative degradation efficacy of metal sulphide photocatalysts..... 24

Table 2.3: Various degradation efficiencies of zinc sulphide photocatalysts. 26

Table 2.4: Various degradation efficiencies of copper sulphide photocatalysts..... 28

Table 2.5: Various degradation efficiencies of CuS/ZnS photocatalysts. 29

Table 3.1: Absorbance values of the prepared standards. 35

Table 4.1: X-ray florescence data for synthesised materials..... 40

Table 4.2: BET analysis surface area and pore size distribution of sorbents. 43

Table 5.1: Photodegradation reaction kinetic parameters for varying binary CuS/ZnS nanocomposite catalyst loading in RhB dye degradation. 55

© University of Pretoria

LIST OF SYMBOLS AND NOMENCLATURE

Symbols

a	absorption coefficient
C_o	initial rhodamine B concentration
C_t	rhodamine B concentration at time t
e^-	conduction band electron
E_g	band gap energy
e^-/h^+	electron/hole pair
eV	electron Volt
h	plank constant
h^+	valence band positively charged hole
K_{max}	maximum rate constant (min^{-1})
min	minutes
mgL^{-1}	milligram per Litre
mL	millilitres
nm	nanometres
ppm	parts per million
r	rate of reaction
RhB	Rhodamine B
rpm	revolutions per minute

© University of Pretoria

LIST OF ABBREVIATIONS

AOPs	Advanced Oxidation Processes
ATZ	Atrazine
BA	Benzoic acid
BCCs	Bio-accumulative chemicals of concern
BET	Braunauer-Emmett-Teller
BOD	Biological Oxygen Demand
CB	Conduction Band
COD	Chemical Oxygen Demand
CPCB	Central Pollution Control Board
DEA	Deethylatrazine
DEHA	Deethyl-2-hydroxyatrazine
DIA	Deisopropylatrazine
DIHA	Deisopropyl-2-hydroxyatrazine
DOC	Dissolved Organic Carbon
EA	Enthalpy
EDS	Energy Dispersive Spectrometer
EDTA-2Na	Ethylenediaminetetraacetic acid disodium salt
EU	European Union
FDA	Food and Drug Administration
FEPA	Federal Environmental Protection Agency
FBRs	Fixed Bed Reactors
FBRs	Fluidised Bed Reactors
FTIR	Fourier Transform Infra-Red

© University of Pretoria

HA	2-hydroxyatrazine
IPA	Isopropyl alcohol
MAL	Maximum Allowed Limit
MB	Methylene Blue
MCL	Maximum Concentration Level
NTPA001	Roman Legal Discharge Standard
$O_2^{\bullet-}$	Superoxide radicals
•OH	Hydroxyl radicals
pBZQ	p-Benzoquinone
PL	Photoluminescence
POPs	Persistent Organic Pollutants
PTBs	Persistent Toxins that Bioaccumulate
TDS	Total Dissolved Solids
TEM	Transmission Electron Spectroscope
TGA	Thermogravimetric Analysis
TSS	Total Suspended Solids
USEPA	United States Environmental Protection Agency
UV	Ultraviolet
UV-Vis	Ultraviolet-visible
VB	Valence Band
WBG	World Bank Group
WHO	World Health Organisation
XRD	X-Ray Diffraction
XRF	X-Ray Fluorescence

© University of Pretoria

RESEARCH OUTPUTS

Journal publications

1. Mugumo, R., Tichapondwa, S.M. and Chirwa, E.M., 2023. Visible-light-induced photocatalytic degradation of Rhodamine B dye using CuS/ZnS p-n heterojunction nanocomposite under visible light irradiation: Catalysts, (Status: Published).
2. Mugumo, R., Ichipi, E., Tichapondwa, S.M. and Chirwa, E.M., 2023. Metal sulphides: Bandgap narrowing dopants for enhanced visible-light-induced photocatalytic water treatment. Chemical Engineering Transactions, (Status: Published)
3. Mugumo, R., Tichapondwa, S.M. and Chirwa, E.M., 2022. Effects of Initial pH and CuS/ZnS Loading in Rhodamine B Photodegradation Under Visible Light Irradiation. Chemical Engineering Transactions, 94, pp.1027-1032. (Status: Published).
4. Mugumo, R., Tichapondwa, S.M. and Chirwa, E.M., 2022. Photocatalytic Degradation of Rhodamine B Using CuS-doped ZnS Under Visible Light Irradiation. Chemical Engineering Transactions, 94, pp.1447-1452. (Status: Published).

Conference presentations

1. The 26th Conference Process Integration, Modelling and Optimisation for Energy Saving and Pollution Reduction (PRES'23), 8-11 October 2023, Thessaloniki, Greece. Bandgap tailoring of ZnO using metallic sulphides for enhanced visible-light-active photocatalytic water treatment. (Status: Oral presentation).
2. The 25th Conference on Process Integration for Energy Saving and Pollution Reduction (PRES'22), 5-8 September 2022, Brac, Croatia. Effects of Initial pH and CuS/ZnS Loading in Rhodamine B Photodegradation Under Visible Light Irradiation. (Status: Oral presentation).
3. The 7th International Conference on Industrial Biotechnology, (IBIC 2022), 5-8 June 2022, Milano, Italy. Photocatalytic Degradation of Rhodamine B Using CuS-doped ZnS Under Visible Light Irradiation. (Status: Oral presentation).

© University of Pretoria

CHAPTER 1: INTRODUCTION

1.1 Background

Water contamination by toxic chemicals is a major global environmental concern. The intensive use of organic chemicals and medicines driven by industrial demand, population growth, and agricultural expansion has led to the mass pollution of aquatic systems world over. A combination of both priority and emerging pollutants are detected at variant concentrations in water bodies (Robles-Molina et al., 2014). This has led to the development of several treatment technologies capable of remediating these toxic compounds from aquatic environments. Textile effluents are regarded as one of the major water polluters. They typically consist of mixtures of dyes, sulphur, nitrates, soaps, naphthol, acetate acid, chromium, and other heavy metals such as mercury, copper, cobalt, arsenic, nickel (Al-Buriahi et al., 2022). Some of these chemicals have mutagenic properties and tend to bioaccumulate resulting in adverse effects to plant, animal and human life (Carmen and Daniela, 2012). Generally, dyes make up the largest component of the organic contaminants in industrial effluents. It has been reported that approximately 20 % of these effluents consist of synthetic dyes such as rhodamine B, methyl red, Congo red and methylene blue that are lost in the dyeing processing steps and discharged into water bodies without further treatment (Hanafi and Sapawe, 2020).

Rhodamine B (RhB) is a cationic xanthene dye that carries an acidic non-esterified phenyl-carboxylic group (Sharifzade et al., 2017). RhB dye is widely used in textiles, paper, food and printing industries as a pigment due to its incredible fluorescence pigment which is highly soluble in water and cost effective (Ajiboye et al., 2021). It is however characterised by a non-biodegradable complex chemical structure that is stable to heat and light (Saigl, 2021). RhB dye is a known neurotoxin and carcinogen, which also causes respiratory diseases such as infection, pneumonia, asthma, lung cancer etc. (Samuel et al., 2021). It is therefore necessary to reduce the undesirable effects that these dyes pose. Various conventional techniques have been widely applied in wastewater treatment, including biodegradation, adsorption, flocculation, chlorination, coagulation, and membrane separation processes to treat wastewater effluent (Saigl, 2021). However, these methods have several limitations, such as high sludge

© University of Pretoria

generation, high operational costs, long processing times, separation difficulties, and chemical instability (Crini and Lichtfouse, 2019). Additionally, they suffer from the stubborn recalcitrant nature of the target pollutants and the generation of secondary pollutants (Naciri et al., 2018). As a result, it is therefore crucial to develop alternative effective methods for removing organic pollutants from wastewater before discharge into water bodies. This has led to an increased focus on Advanced Oxidation Processes (AOPs) due to their inherent advantages, including operation under ambient conditions, non-selective degradation of organic and microbial pollution, elimination of sludge production, and their sunlight harnessing ability (Gedda et al., 2021). Advanced Oxidation Processes (AOPs) such as sonolysis, ozonation, the Fenton process, photolysis, and photocatalysis have shown good potential in degrading and mineralising refractory toxic organic pollutants (Mahamuni and Adewuyi, 2010). These AOPs typically function by producing highly reactive, fast-acting, non-selective free radicals which attack the target organic pollutants to form intermediate products or benign H_2O and CO_2 (Cashman et al., 2019).

Photocatalysis is one of the most researched AOPs due to its high degradation efficiency, continuously evolving nature and it being regarded as a green, sustainable water treatment technology (Samuel et al., 2021). However, the application of common semiconductor photocatalysts such as TiO_2 and ZnO are limited by their wide bandgap energy, which makes them active under UV light irradiation only (Lin et al., 2005). Other significant drawbacks include high recombination rate of the photogenerated electron and hole pairs (e^-/h^+) and poor chemical stability for recycling purposes (Xu et al., 2020). Bandgap engineering to tailor semiconductor materials for inhibition of recombination rate and visible-light activation is a new concept in photocatalytic applications (Zhang et al., 2021). This involves various strategies such as metal doping and heterojunction formation of composite catalysts to enhance their photocatalytic activity under visible-light irradiation (Wu et al., 2016). This concept has proven to be effective in inhibiting e^-/h^+ pair recombination which in turn improves the photocatalytic activity of the material (Guo et al., 2016). Heterojunction based catalysts also promote and accelerate the migration of e^+/h^+ pairs resulting in a more efficient process. Typically, p-n heterojunction semiconductor systems are used in photocatalysis (Low et al., 2017). The photons with energies equal to or higher than the semiconductor photocatalyst band gap energy create a built-in electric field within the space charge region which quickly separates the photoinduced e^-/h^+ pairs during irradiation. This electric field drives the transfer

© University of Pretoria

of electrons to the conduction band (C_B) of n-type and holes to the valence band (V_B) of p-type semiconductors. Some of the advantages of p-n type heterostructures include: (i) rapid charge transfer of catalysts; (ii) effective charge separation; (iii) longer charge carriers lifetime; and (iv) separation of incompatible redox reactions (Wang et al., 2014).

ZnS and CuS are notable examples of sulphur-based semiconductor photocatalysts due to their eco-friendliness, affordability, low toxicity, and exceptional photo-absorption capabilities (Harish et al., 2017). ZnS has a bandgap energy of around 3.7 eV, which is relatively wide, and can only absorb about 4% of total sunlight in the UV range. Additionally, it exhibits rapid recombination rates for photoinduced charge carriers, which limits its practicality as a photocatalyst. On the other hand, although CuS has a narrow bandgap of about 2.2 eV, it is prone to photocorrosion. This drawback can be effectively resolved by coupling CuS with ZnS (Hong et al., 2015). This results in the formation of a p-n heterojunction photocatalyst with superior photoactivity under visible-light irradiation (Mondal et al., 2015). The CuS/ZnS heterojunction nanoparticles are characterised by heterogeneous interfaces and an increased number of lattice defects. These defects introduce vacancies in the crystal lattice, creating impurity states within the bandgap. This enhances the ability of the catalyst to utilise visible light and additionally plays a crucial role in facilitating electron transfer by serving as an electron trap, thereby inhibiting the recombination of photogenerated carriers (Guo et al., 2021). Moreover, the partitioning of sulphur dopants within the CuS/ZnS p-n heterojunction nanocomposite and the presence of lattice defects expose more active sites, leading to a further enhancement in the photocatalytic activity of the catalyst and improved recyclability (Li et al., 2022).

Studies have reported a significant enhancement in the photocatalytic activity of several binary sulphur-based CuS/ZnS nanocomposites using the p-n heterojunction concept. Mondal et al. (2015) reported highly improved methylene blue removal through the coupling of binary p-n heterojunction CuS/ZnS photocatalysts, unlike CuS and ZnS prepared via the ion-exchange hydrothermal method. Another study by Sitinjak et al. (2022) demonstrated the dramatic enhancement of 4-aminophenol degradation under visible light using the binary CuS/ZnS composite (100 %), yet 64 % and 28 % degradation was reported for the individual constituent CuS and ZnS catalysts, respectively.

© University of Pretoria

1.2 Aims and objectives

The primary aim of this study was to examine the effectiveness of a visible-light-active CuS/ZnS p-n heterojunction semiconductor photocatalyst in degrading rhodamine B dye under visible light irradiation exposure. In pursuit of this goal, the study aimed to accomplish the following objectives:

- Synthesis and characterisation of visible light activated photocatalysts (ZnS, CuS and CuS/ZnS) synthesised via an innovative facile one – pot solid phase method.
- Investigation of the as-synthesised photocatalysts on rhodamine B dye removal efficiency under visible light irradiation.
- Process optimisation through variation of extrinsic parameters, kinetic modelling, and forensic degradation studies.
- Degradation mechanism proposition based on achieved results.

Figure 1.1 demonstrates the research study plan outline and various stages during study conduction.

1.3 Study significance

This study provides a vital assessment of the binary CuS/ZnS nanomaterials efficacy in photocatalytic reactions, as well as the potential enhancement of photodegradation through semiconductor surface structure modification using CuS as a dopant onto the pristine ZnS material surface through the formation of a p-n junction. This modification leads to retardation of recombination of photoexcited charge carriers, and to a reduction in the band gap between the valence and conduction bands; thus, allowing visible light to be utilised consequently enhancing the degradation efficacy of rhodamine B dye. The study also establishes parameters that can be utilised for scaling up and for the optimisation and remediation of water treatment plants. To better understand the photocatalysis process, the chemical behaviour, particle

© University of Pretoria

morphology, crystalline phases and bandgap energy of the synthesised nanocomposites were also examined, and a reaction mechanism proposed.

1.4 Dissertation scope

Chapter 1: Introduction

Description of background information and study motivation including its stated aim and specific objectives.

Chapter 2: Literature review

Current and previous literatures used in provision of a holistic review on matter of subject, materials development, and photodegradation of organic pollutants.

Chapter 3: Materials and methods

Focuses on used reagents and employed methods highlighting on the method of synthesis, characterisation and photodegradation studies of the synthesised particles.

Chapter 4: Photocatalysts characterisation

Determination of physicochemical properties of synthesised photocatalysts analysed using different characterisation tests.

Chapter 5: Degradation in-depth studies

Assessment and measurement of the synthesised photocatalysts degradation efficacy in rhodamine B dye degradation under visible light irradiation whilst varying different extrinsic parameters such as catalyst dosage, constituent catalyst, initial pollutant concentration, initial pH, catalyst recyclability and analysis of the respective degradation kinetics.

© University of Pretoria

Chapter 6: Conclusions and recommendations

Presentation of study conclusions, experienced limitations, and further research recommendations on the study topic.

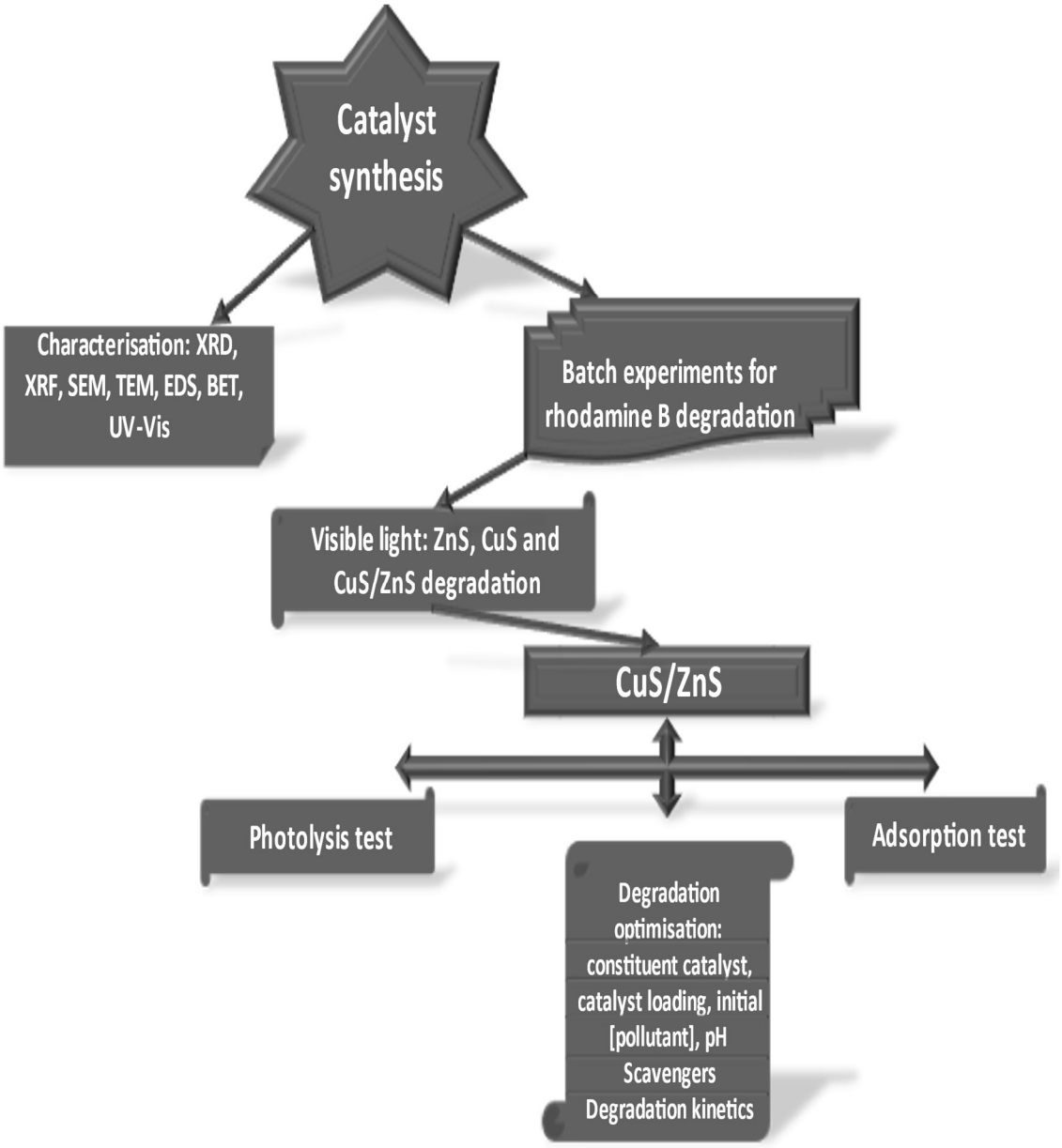

Figure 1.1: Research study plan outline.

© University of Pretoria

CHAPTER 2: LITERATURE REVIEW

2.1 Organic pollutants

Water contamination from industrial production has attracted a lot of attention as water is critical in sustaining all life forms. There is a rising need to extensively treat textile wastewater containing deleterious, recalcitrant compounds (Jain et al., 2007). Access to clean water has become a global concern due to demographic growth, and development of industries and technology, which leads to increased industrial wastewater discharges that directly affect water quality (Byrappa et al., 2006). These toxic pollutants/ substances constantly circulate in the environment and water bodies thereby continuously threatening the biosphere. Their presence in the environment even in minute quantities can pose detrimental health effects such as chronic toxicity, neurological and developmental disorders (Saravanan et al., 2021).

Dyes are a group of organic compounds used mostly in textile, cosmetic, pharmaceutical, printing, papermaking, and food processing industries with huge amounts applied during the colouring process (Ahmad et al., 2021). Textile industries use azo dyes which are highly water soluble to meet colour requirements and they generate approximately 17-20 % of wastewater effluents (Al-Mamun et al., 2019). The discharge of untreated effluents into water bodies includes synthetic dyes like rhodamine B, methyl red, Congo red, and methylene blue, which are lost during the dyeing process (Hanafi and Sapawe, 2020).

Rhodamine B (RhB) is an organic cationic basic dye which represents anthraquinone xanthene dyes used in industrial applications characterised by difficult biochemical degradation and high chromaticity (Xu and Ma, 2021). Xanthene dyes are composed of amino groups that are linked by glycosidic bonds formed through a process that connects both amino group units. RhB can be found in two distinct forms: an open/fluorescent form and a closed/non-fluorescent spirolactam form. These forms coexist in an equilibrium, with the open form being most favoured in acidic environments, while the closed form is favoured in basic environments (Al-Buriahi et al., 2022). The RhB dye molecular structure is depicted in Figure 2.1.

© University of Pretoria

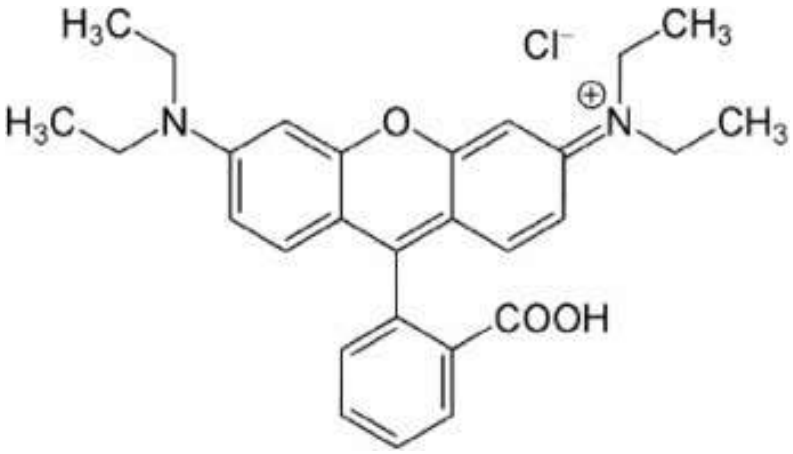

Figure 2.1: The molecular structure of rhodamine B dye (Al-Gheethi et al., 2022).

Even at low concentrations, various dyes like RhB dye exhibit distinct colours that can be easily observed on water surfaces, leading to water contamination. These dyes possess characteristics such as chemical stability, high aromaticity, low biodegradability, toxicity, carcinogenic properties, and the resulting generation of significant pollution on a large scale (Ahmad et al., 2021). Generated textile wastewater impacts the quality of the aquatic system, recipient water bodies, environmental biodiversity, and human health (Al-Mamun et al., 2019). Even in minute concentrations, the presence of dyes has an impact on the transparency and gas solubility of water. Dyes absorb and reflect sunlight that enters the water, thereby reducing the oxygen levels and affecting the growth of aquatic species and interfering with photosynthesis. Additionally, depending on the concentration and duration of exposure, dyes can have acute or chronic effects on organisms present in the water. RhB poses a significant health risk as it exhibits severe toxicity towards humans and animals. Exposure to this dye is carcinogenic and neurotoxic, and can lead to allergic dermatitis, skin irritations, mutations, and even cancer, highlighting the potential dangers associated with its use (Natarajan et al., 2018).

In fact, due to consumption of dye polluted water, the United Nations reports an estimated annual mortality of 1800 deaths of children under 5 years old globally (Samuel et al., 2021). This has urged regulatory bodies such as the Central Pollution Control Board (CPCB), Roman legal discharge standard (NTPA 011), and Federal Environmental Protection Agency (FEPA) to set maximum allowable values for textile water parameters such as pH (5.5-9.0), total

© University of Pretoria

dissolved solids (TDS; 1500-2000 mgL^{-1}), total suspended solids (TSS; 35-50 mgL^{-1}), biological oxygen demand (BOD; 15-30 mgL^{-1}) and chemical oxygen demand (COD; 100-250 mgL^{-1}) (Al-Buriahi et al., 2022). The variability and complexity of textile effluents promotes the implementation of advanced water recovery systems such as flocculation/ coagulation, membrane and biological processes and Advanced Oxidation Processes (AOPs) (Paździor et al., 2019). The wastewater effluent generation, toxicity, and treatment techniques are depicted in Figure 2.2.

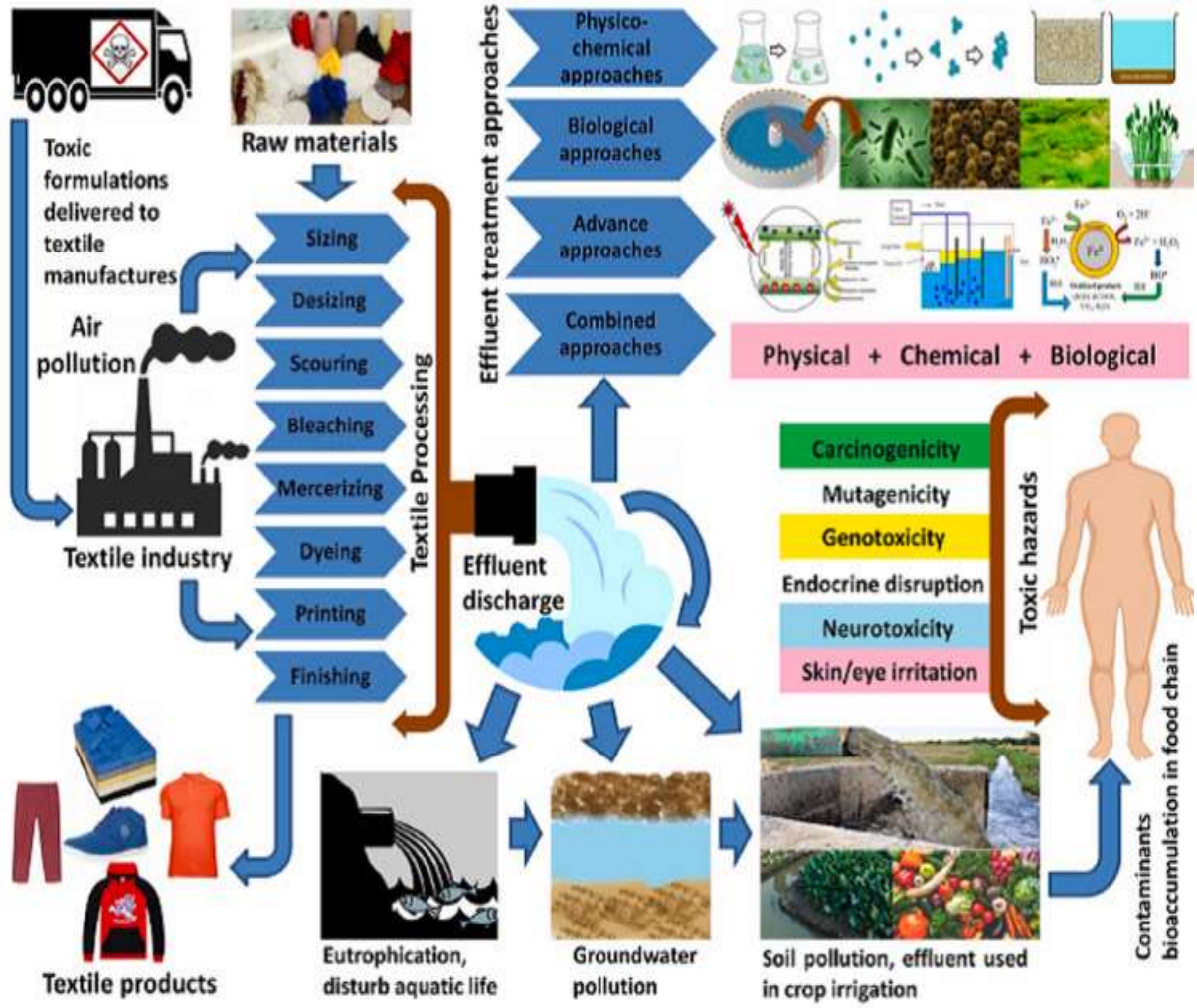

Figure 2.2: Textile industry: wastewater effluent generation, toxicity, and treatment techniques (Kishor et al., 2021).

© University of Pretoria

2.2 Current water treatment techniques and their drawbacks

Traditional conventional methods such as membrane separation, biological treatment, and chemical coagulation have been widely applied in the treatment of textile wastewater. However, these methods have experienced drawbacks such as long processing times, chemical instability, high operational costs, separation difficulties and high sludge generation (Mugumo et al., 2022). Physical techniques such as adsorption and membrane filtration involve the separation of one or more compounds from the waste stream, leading to the transfer of pollutants from one phase to another. However, additional treatment is necessary to degrade the contaminants present in the second phase (Mohajerani et al., 2009). Additionally, the use of chlorination as a tertiary treatment process can result in the creation of more toxic chlorinated organic compounds that are even more carcinogenic than the original organic molecules. Although anaerobic wastewater treatment has shown promise as an alternative, complete replacement of aerobic technology with anaerobic methods is not currently feasible (Xiao et al., 2019).

Other alternative chemical oxidation water treatment technologies include the Fenton process and ozonation. The Fenton process involves the use of a Fenton's reagent, which is a mixture of hydrogen peroxide and iron (II) ion. This reagent is considered one of the most effective oxidising agents for degrading organic pollutants in wastewater (Babuponnusami and Muthukumar, 2014). However, the Fenton-based oxidation processes have safety hazards associated with the use of H_2O_2, and the need to first lower the pH to very acidic levels before subsequently neutralising it (Matavos-Aramyan and Moussavi, 2017). Also, ozonation is a chemical technique dependant on the infusion of ozone into an aqueous state and then applied in wastewater treatment. However; several drawbacks to ozonation include high operational costs, significant energy consumption, and the need for trained professionals to maintain and operate the equipment (Al-Rubaiey, 2022).On the contrary, photocatalysis is a promising eco-friendly and sustainability technology for the efficient removal of toxic pollutants from wastewater due to its broad range of applicability (Samuel et al., 2021), its ability to use higher wavelengths than UV-based techniques and the use of affordable, non-toxic ambient inputs (Wang et al., 2017b).

© University of Pretoria

2.3 Advanced Oxidation Processes

Advanced oxidation processes (AOPs) encompass the in-situ production of hydroxyl radicals (•OH), which effectively oxidise both inorganic and organic substances, presenting the potential for complete degradation/mineralisation into carbon dioxide and water (Wang et al., 2007). To achieve this, AOPs follow a general trend as shown by the following redox reactions (Sirés et al., 2014):

$$organic\ pollutants\ +\bullet OH\ \rightarrow oxidation\ intermediates$$

$$intermediates\ +\bullet OH \rightarrow\rightarrow\ CO_2 + H_2O$$

The generation of •OH radicals in AOPs is intricately linked to the specific technique employed. Consequently, UV/H_2O_2, ozonation, and photocatalytic oxidation exhibit distinct mechanisms for •OH radical production, each with its own set of limitations. Among the extensively researched AOPs, three prominent ones are UV/H_2O_2, ozonation, and photocatalysis, which harness either ultraviolet (UV) or solar irradiation (Fujishima, 2000). Photocatalysis is the most promising viable alternatives as they have been developed for the degradation of organic water pollutants and their effectiveness in complete mineralisation of dyes and pesticides thereby causing a decrease in overall effluent toxicity (Naciri et al., 2018).

2.3.1 Factors Affecting Photocatalysis

2.3.1.1 Effect of catalyst loading

The photocatalytic degradation is influenced by increase in catalyst dosage, though there is a limit to this correlation. Increasing the dosage of the catalyst leads to provision of more active sites for photon absorption which results in more •OH radicals and positively charged holes generation when upon light irradiation exposure. Research conducted by Arjunan et al. (2016) revealed improved degradation efficacy at increased catalyst dosages however, increasing the loading beyond optimum resulted in decreased photocatalytic performance due to light scattering caused by the suspended particles which hinders light from reaching the catalyst. In

© University of Pretoria

another study by Mohammed et al. (2021), it was observed that increasing catalyst loading led to an enhanced photodegradation performance.

2.3.1.2 Effect of initial pH

The solution pH is an important parameter that affects the photocatalytic performance of photocatalysts. The surface charge of the photocatalyst and speciation of the target pollutant are influenced by pH, which in turn affects the subsequent adsorption and photocatalytic processes (Alshamsi et al., 2021). However, the interpretation of the effect of pH on dye photodegradation efficiency is challenging due to its multiple roles. There are three possible reaction mechanisms that contribute to dye degradation, including hydroxyl radical attack, direct oxidation by positively charged holes, and direct reduction by electrons in the conducting band (Mohammed et al., 2021).

2.3.1.3 Effect of initial pollutant concentration

The initial concentration is a significant factor to consider in photocatalytic performance since an increase in concentration will most likely promote competition between the pollutant molecules and available photogenerated radical species (Mohanty et al., 2022). In a study conducted by Saadati et al. (2016) which focused on the impact of initial reactive yellow 14 dye concentration, it was observed that increase in initial dye concentration led to a decrease in the photodegradation performance. This decrease can be attributed to a higher amount of adsorbed dye molecules, which hinder the reaction between dye molecules and photogenerated holes or hydroxyl radicals due to a lack of direct contact. Furthermore, increasing the dye concentration causes the dye molecules to absorb more light, thereby preventing photons from reaching the surface of the photocatalyst. As a result, photodegradation efficiency is reduced (Ahmad et al., 2021).

2.3.1.4 Effect of light intensity

Light irradiation intensity is directly related to the likelihood of electron excitation in photocatalysis; however, excessive irradiation intensities lead to fast recombination of

© University of Pretoria

photoinduced carrier charges, which subsequently impedes the photocatalytic activity (Koe et al., 2020).

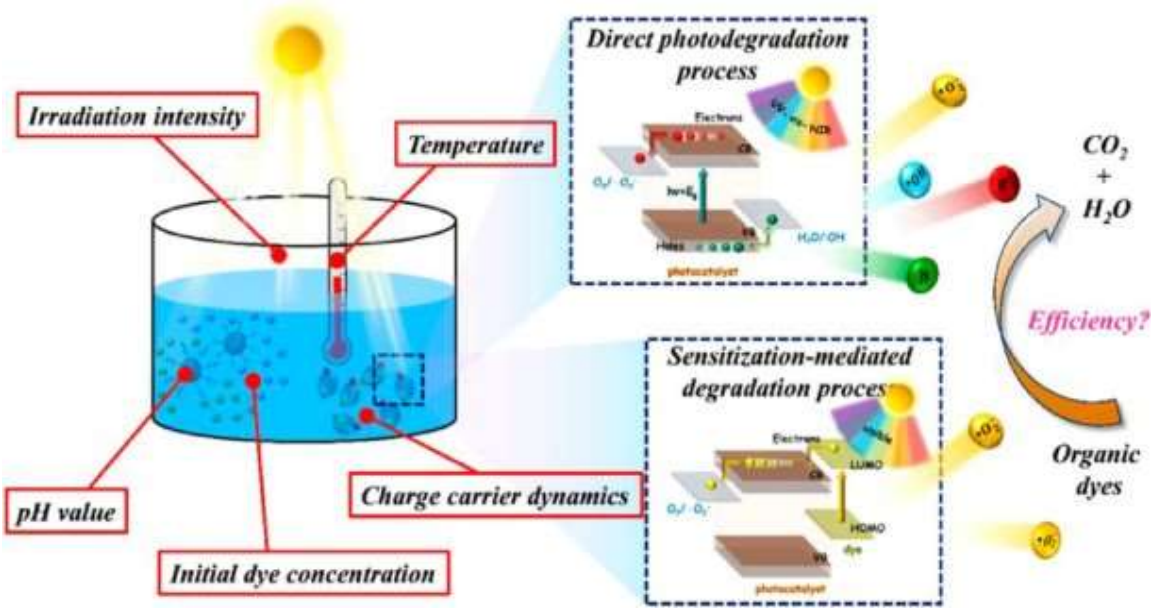

Figure 2.3: Operational parameters influencing the photocatalytic degradation of organanopollutants (Rafiq et al., 2021).

2.3.2 Homogeneous photocatalysis

Homogeneous photocatalysis involves reactions where the reactants and catalyst share similar states, predominantly in liquid form, and are initiated by light within a wavelength range of up to 600 nm. The efficiency of homogeneous photocatalysis is influenced by the dosage of oxidising chemical additives like ferrous salts or hydrogen peroxide (H_2O_2). In UV/H_2O_2 processes, the presence of carbonate ions within pH ranges of 8 to 9 serves as scavengers, while excessive addition of H_2O_2 hampers the oxidation rate by reducing the production of hydroxyl radicals (Chong et al., 2010). The effectiveness of UV-based methods is hindered by the presence of intense colouration and high turbidity in wastewater, as well as the high cost associated with artificial UV lamps. On the other hand, photo-Fenton processes can lead to the generation of sludge, elevated concentrations of sulphate or chlorine anions (depending on the type of ferrous salt used), and significant acid consumption for pH reduction. Overall, homogeneous processes tend to incur substantial operational expenses due to the need for sludge disposal and the use of chemical oxidants (Collivignarelli et al., 2017).

© University of Pretoria

2.3.3 Heterogeneous photocatalysis

Heterogeneous photocatalysis involves the utilisation of semiconductors that harness photons to enhance reactions without being consumed in the process. In this type of photocatalysis, the reactants (usually liquids and gases) and the photocatalyst (solid or liquid) exist in different states. The primary advantage of heterogeneous photocatalytic processes over homogeneous ones is the cost-effectiveness of catalyst recovery and recycling, as the reagents and semiconductor are in distinct phases. Additionally, operating costs are lower since ambient oxygen serves as the oxidant, eliminating the need for expensive oxidising chemicals like hydrogen peroxide (Wang et al., 2018b). Furthermore, semiconductors are highly recyclable and can be easily reused. They have the ability to utilise abundant visible irradiation, offering promising prospects for sustainable energy solutions. Additionally, semiconductors possess the capacity for self-regeneration, further enhancing their efficiency and longevity (Malefane et al., 2019).

2.3.3.1 Semiconductor photocatalysis

Semiconductor photocatalysis belongs to the category of heterogeneous AOPs where a catalytic surface facilitates photoreactions (Grabowska, 2016). Photocatalysis encompasses a diverse range of applications, including fuel regeneration (via carbon dioxide reduction and water splitting) and organic pollutant degradation. The field of semiconductor photocatalysis has experienced remarkable advancements since the ground-breaking discovery made by Fujishima and Honda. Their discovery highlighted the photocatalytic water splitting capability of titanium (IV) oxide (TiO_2) nanoparticles, propelling exponential progress in this area (Fujishima, 2000). Semiconductor photocatalysts are highly effective in the treatment of wastewater due to their easy instrumental procedure, simple controlled operation, cost effective, non-selective oxidation and organic dye complete degradation to harmless products (Ahmad et al., 2021).

When photons with an energy equal to or greater than the bandgap (E_g) of a semiconductor catalyst illuminate it, an electron (e^-) from the valence band (V_B) is promoted to the conduction band (C_B), leaving behind a positively charged hole (h^+) in the V_B. Normally, these excited state electrons and holes tend to recombine, dissipating the input energy as heat or emitted

© University of Pretoria

light. However, if the electrons and holes can migrate to the surface of the semiconductor without recombining, they can participate in electrochemical processes with species adsorbed on the surface of the semiconductor photocatalyst. The photogenerated electrons act as reductants, while the holes act as oxidants, as depicted in Figure 2.4. This redox ability of the electron-hole pairs can be harnessed for photocatalytic water and air remediation, as well as photocatalytic hydrogen production. Photoinduced holes play a crucial role in the environmental pollutants oxidative degradation, while photoinduced electrons are vital for water reduction (Adhikari, 2017).

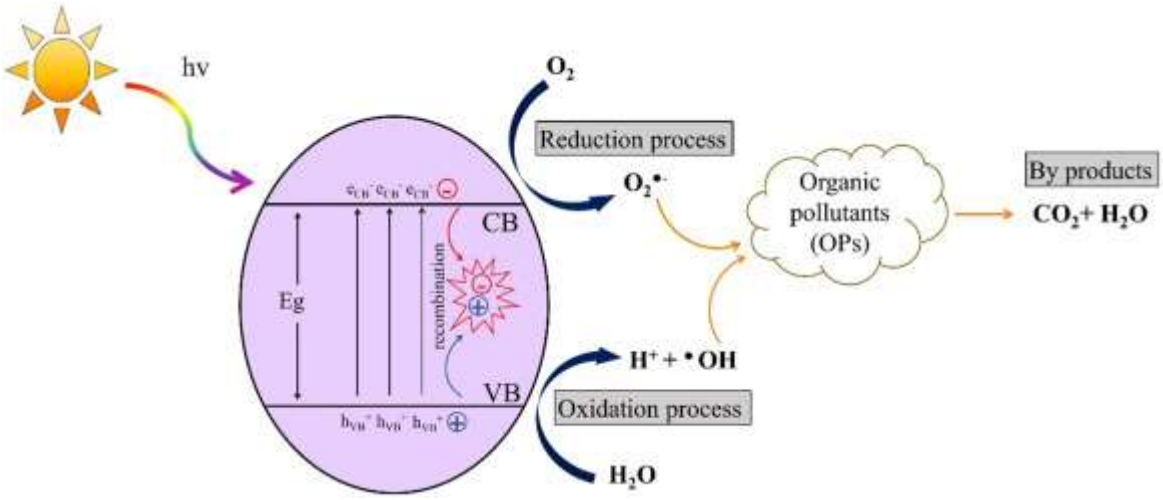

Figure 2.4: Basic schematic representation of photocatalytic degradation mechanism of organic pollutants under light irradiation (Kanakaraju and Chandrasekaran, 2023).

The overall quantum efficiency for interfacial charge transfer in semiconductor photocatalysis is influenced by the recombination of photoinduced charge carriers. This recombination process reduces the overall quantum efficiency thereby limiting photocatalysis in potential industrial applications. During recombination, the excited electron returns to the valence band without engaging in radiative or non-radiative reactions with adsorbed species, resulting in the dissipation of energy as light or heat. Recombination can take place either on the surface or within the bulk of the semiconductor. It is typically facilitated by defects, impurities, or any factors that introduce imperfections in the crystal's bulk or surface (Chen and Mao, 2007).

© University of Pretoria

2.3.3.2 Photocatalysis drawbacks and solutions

Commonly used chemical oxidation techniques are suitable for lowering and removal of high organic pollutant concentrations; however, they are faced with the limitation of undergoing incomplete mineralisation (Le et al., 2019). Furthermore, fast recombination of photogenerated electron/hole pairs, and the wide band-gap energy of most photocatalysts limits their excitation to ultraviolet or near-ultraviolet radiation, which accounts for only 4 % of the solar light spectrum reaching the Earth (Wang et al., 2014). In response to these significant limitations, there has been a growing high demand for the effective harnessing of sustainable renewable energy sources, particularly sunlight, which presents a green, cost-free, secure, and abundant energy resource (Chala et al., 2019). Moreover, numerous strategies have been devised to rationally design and fabricate heterojunction photocatalysts (Wang et al., 2014) with engineered narrow band gap energies for improved photocatalytic performance (Karthikeyan et al., 2020).

2.4 Strategies for optimising charge separation efficiency

Numerous methods have been proposed to enhance charge separation and migration, leading to reduced recombination and improved photocatalytic activity. The most employed strategies include: (i) surface modification through the deposition of a redox couple or noble metal, resulting in a metal/semiconductor heterostructure; (ii) constructing a semiconductor/semiconductor heterostructure by coupling two semiconductors with different band gap energies; (iii) concurrent scavenging of holes and electrons by redox species adsorbed on the surface; (iv) utilising charge carrier trapping mechanisms (Wang et al., 2014). These approaches aim to promote efficient charge transfer and minimise recombination, thereby enhancing the overall performance of photocatalytic systems.

2.4.1 Metal/semiconductor heterostructure nanocomposites

Depositing noble metals onto semiconductor surfaces is an effective technique to increase the lifespan of photogenerated electron-hole pairs and consequently reduce their recombination (Bumajdad and Madkour, 2014). Previous studies have demonstrated that combining metals

© University of Pretoria

with semiconductors enhances the efficiency of the photocatalytic process. In this process, the metal deposits, which vary based on their physicochemical properties, act as passive sinks for electrons or holes, effectively impeding their recombination. When metals and semiconductors come into contact, their different work functions create a space charge region. This space charge region, coupled with the built-in potential, facilitates the separation and transportation of photogenerated electron-hole pairs (Uddin, 2013).

2.4.2 Coupled semiconductor/semiconductor heterostructure nanocomposites

Another highly effective approach for enhancing charge separation and reducing charge-carrier recombination to improve photocatalytic activity is through the coupling of two semiconductors with different band gap energies, resulting in a heterostructure semiconductor (Uddin, 2013). Significant efforts have been devoted to synthesising various coupled semiconductors, such as the CdS/ZnS, ZnO/ZnS, and CuS/ZnS semiconductor photocatalysts. These materials present great potential for various applications, including water splitting, photovoltaic devices, and organic pollutant degradation (Leschkies et al., 2007). Moreover, they are considered promising candidates for developing high efficiency photocatalysts activated by visible light irradiation. One key advantage of coupled semiconductors is their ability to compensate for the limitations of the individual constituent semiconductor catalysts, leading to a synergistic effect. These characteristics are demonstrated through effective charge separation and enhanced photostability, resulting in improved photocatalytic performance (Deng et al., 2020).

© University of Pretoria

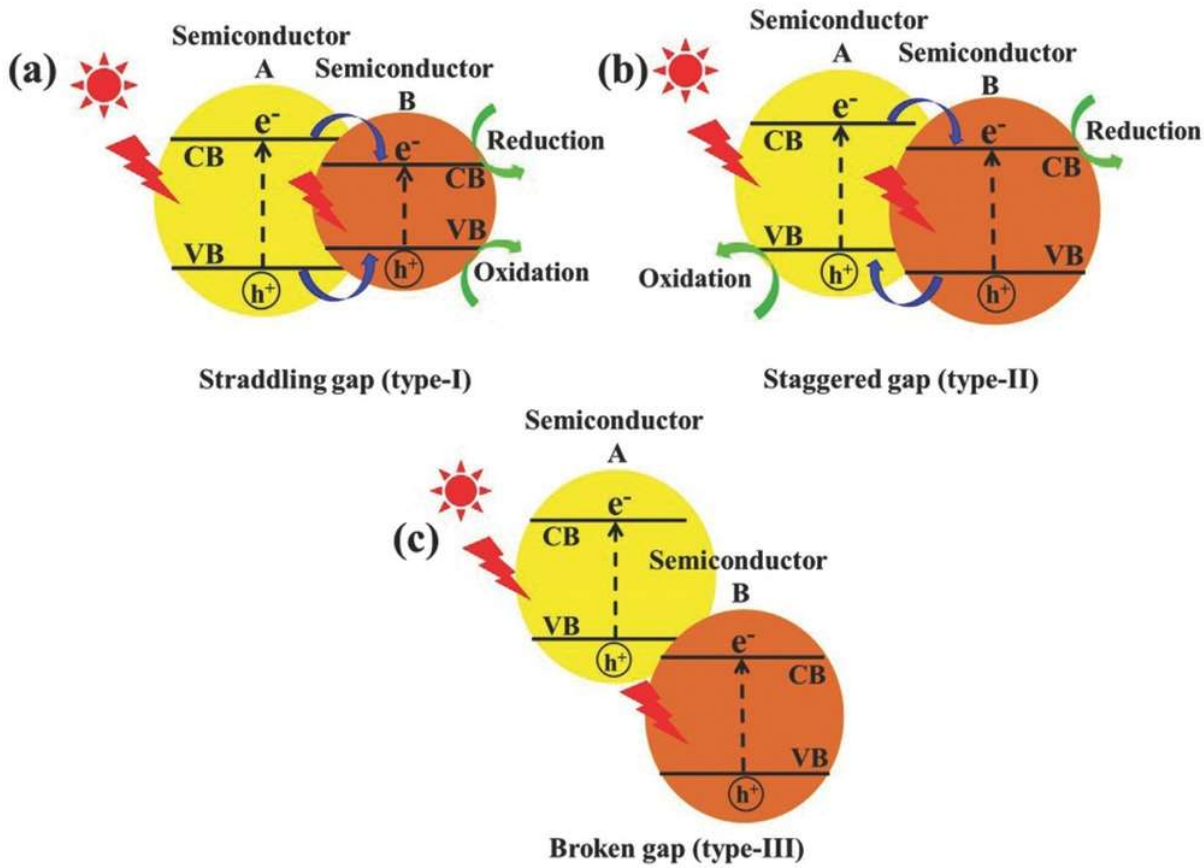

Figure 2.5: Schematic energy band forms of semiconductor heterojunctions (a) type-I, (b) type-II, and (c) type-III (Low et al., 2017).

The charge separation mechanisms of heterostructure photocatalysts is illustrated schematically in Figure 2.5. When a heterostructure photocatalyst is illuminated with UV/visible light irradiation, electrons in the V_B are excited to the C_B forming an electron-rich area, leaving the positively charged holes in the valence band forming a hole-rich area. This directional injection of electrons from one C_B to the next and holes from one V_B to the other enhances the rate of charge separation and reduces the recombination of electron-hole pairs.

© University of Pretoria

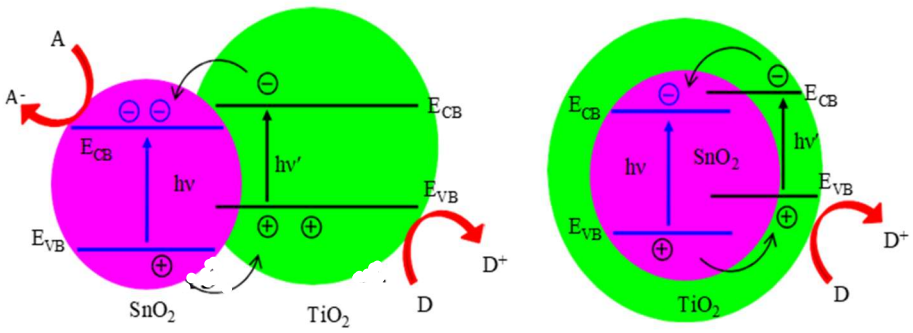

Figure 2.6: Schematic coupled heterostructure composites charge transfer illustration (Uddin, 2013).

Heterostructure photocatalysts can exhibit different morphologies, such as contact type or core/shell type, depending on their structure. While the charge separation mechanism remains the same in both contact type and core/shell type semiconductors, the interfacial charge transfer exhibits significant variations (Kuo et al., 2011). Figure 2.6 illustrates the charge transfer mechanisms involved in contact type and core/shell semiconductor systems. In contact type semiconductor systems, the two particles are in direct contact, enabling both electrons and holes to be accessible for selective reduction and oxidation processes on surfaces of the different particles. Conversely, in core/shell type heterostructures, electrons are injected into the energy levels of the core semiconductor (if its conduction band potential is lower than that of the shell). As a result, only one charge carrier is available at the surface in a core/shell type semiconductor system, facilitating selective charge transfer at the semiconductor-electrolyte interface. The other charge carrier becomes confined within the inner semiconductor particle, limiting its accessibility for the reduction reaction (Reiss et al., 2009). However, in coupled heterostructure composite nanoparticles, the charge separation is achieved without the need for an external electric field. Instead, charge separation occurs through the tunnelling of electrons between the coupled nanoparticles. This process allows for efficient charge transfer and reduces the chances of recombination (Reineck et al., 2012).

© University of Pretoria

2.5 Heterojunction photocatalysts

A heterojunction involves the combination of two semiconductors, typically with different electronic properties, to create a junction that facilitates charge separation and promotes photocatalytic reactions by improving the charge separation and transfer efficiency (Li et al., 2020). When two different semiconductors are joined, a built-in electric field is generated due to the band alignment differences between them, which drives the separation of photogenerated electron-hole pairs (Wang et al., 2017a). The photogenerated electrons and holes can move towards the interface of the two materials, where they are separated by the built-in electric field and transferred to different materials, leading to a reduction in the recombination rate and an increase in the photocatalytic efficiency (Li et al., 2020). Unlike single-phase photocatalysts, heterojunction semiconductors or integrated multi-semiconductor systems offer significant advantages in facilitating the separation of electron-hole pairs and enabling redox reactions to occur at separate reaction sites. The objective of designing heterostructured photocatalysts is to enhance the separation of photoinduced charge carriers by incorporating appropriate electronic structures within the same material, thereby establishing various carrier-transfer pathways (Wang et al., 2014).

2.5.1 p-n heterojunction photocatalysts

Within these heterojunctions, the p-type semiconductor exhibits a lower Fermi level compared to the n-type semiconductor. When the two semiconductors come in contact, they create a p-n junction with a space charge region. This region facilitates the transfer of electrons and holes in opposite directions, as depicted in Figure 2.7. Specifically, electrons are transferred to the n-type semiconductor C_B, while holes are transported to the p-type semiconductor V_B. This transfer of electron-hole pairs is driven by the electric field that forms within the space charge region (junction) (Adhikari, 2017). As a result, the p-side of the junction acquires a negative charge while the n-side becomes positively charged, establishing an electric field in the vicinity of the junction. In equilibrium, the region close to the junction lacks free carriers, leading to the formation of a space charge configuration characterised by a strong electric field. This configuration forms an electric dipole layer, with positive charge towards the junction of the n-type semiconductor and negative charge towards the interface of the p-type semiconductor.

© University of Pretoria

Consequently, the energy bands of the n-type semiconductor curve upwards, while those of the p-type semiconductor curve downwards (Low et al., 2017).

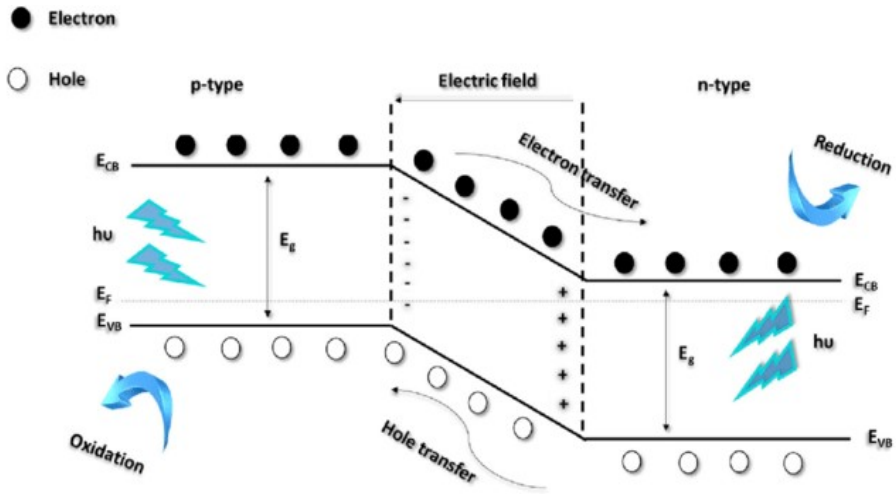

Figure 2.7: Schematic illustration of the energy band structure and electron-hole pair separation in the p-n heterojunction (Amaterz et al., 2020).

Semiconducting materials can be classified into either p-type or n-type based on their donor and acceptor properties, as illustrated in Table 2.1. When appropriately chosen p-type and n-type semiconductors with suitable band gaps and band positions are combined, following the mechanism depicted in Figure 2.7, they can form p-n heterojunction composites. Therefore, the synthesis method is a crucial step in achieving effective p-n junction-based composites. Simultaneously, the morphology of the synthesised heterojunction samples plays a significant role in determining the photocatalytic activity of the catalysts (Adhikari, 2017).

© University of Pretoria

Table 2.1: Some p-type and n-type semiconductors with their respective crystal structures and band gaps (eV).

p-type semiconductor				n-type semiconductor			
	Crystal structure	**Band gap, eV**	**Reference**		**Crystal structure**	**Band gap, eV**	**Reference**
Sr_2CuInO_3S	polyhedral	2.3	(Jia et al., 2014)	ZnO	hexagonal	3.4	(Zhang et al., 2010)
$CaFe_2O_2$	orthorhombic	1.9	(Liu et al., 2017)	WO_3	monoclinic	2.7	(Miyauchi et al., 2013)
Cu_2O	cubic	2.0	(Hu et al., 2008)	TiO_2	tetragonal	3.2	(Zelekew and Kuo, 2016)
$BiVO_4$	tetragonal	1.3	(Wang et al., 2019)	$FeNbO_4$	monoclinic	2.0	(Shi et al., 2016)
NiO	cubic	3.5	(Zhang et al., 2010)	BiOI	tetragonal	2.9	(Kwolek and Szaciłowski, 2013)
Bi_2O_3	monoclinic	2.8	(Yi et al., 2015)	CeO_2	cubic	3.2	(Yang et al., 2014)

An illustration of this is the work by Li et al. (2012) who synthesised a p-n junction-based composite in the form of hollow spheres using bismuth oxide and bismuth tungstate. The exceptional photocatalytic efficiency of this composite in harnessing visible light for photocatalysis was attributed to the efficient separation of charge carriers, facilitated by the formation of a p-n junction within the loosely packed hollow nanostructure.

© University of Pretoria

2.5.2 Metal-sulphide -based heterojunction photocatalysts

Metal sulphide-based semiconductors stand out as prominent photocatalysts for their ability to efficiently facilitate dyes degradation present in wastewater. These photocatalysts offer a cost-effective, eco-friendly, and sustainable solution for advancing environmental protection through wastewater treatment technologies owing to their broad photo-absorption ranges and tunable bandgaps (Ayodhya and Veerabhadram, 2018). Nonetheless, single-metal-sulphide photocatalysts lack the ability to exhibit both strong redox capabilities and rapid charge-separation properties; lack of sufficient active sites and suffer severe photocorrosion which significantly limits the photocatalysis efficiency (Varghese, 2021).

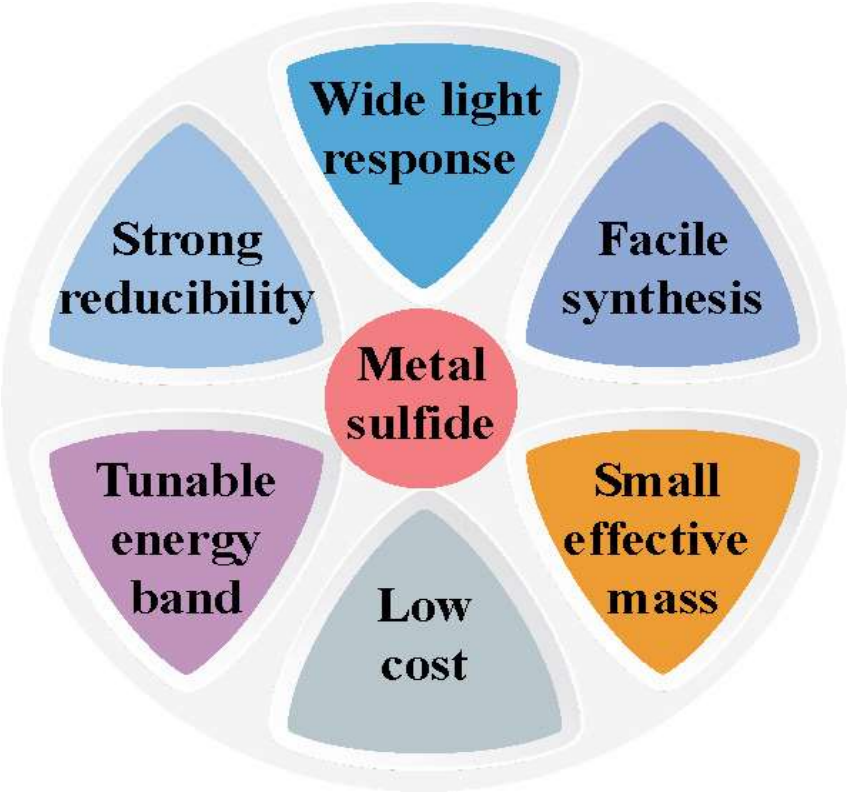

Figure 2.8: Metal sulphides advantages in photocatalytic applications (Zhang et al., 2023).

Consequently, it is therefore critically essential to construct heterojunctions by combining metal sulphides with other semiconductor materials with narrow bandgaps (Zhang et al., 2023).

© University of Pretoria

Abubshait et al. (2021) fabricated Co-NiS/S-g-C_3N_4 heterojunction photocatalysts via a hydrothermal synthesis technique which was tested on 10 mgL^{-1} methylene blue (MB) dye under visible light irradiation. At a catalyst loading of 1 gL^{-1}, an excellent 98 % MB dye removal was achieved by the NiS/S-g-C_3N_4 heterojunction composite compared to the 32 %, 55 % and 59 % yielded by NiS, Co-NiS and S-g-C_3N_4 single catalysts respectively. In another study conducted by Li et al. (2020), CdS/FeS heterojunction nanocomposites were synthesised through a liquid-phase thermal decomposition method. The degradation efficiency of the prepared material was tested on a 0.02 gL^{-1} RhB and 0.02 gL^{-1} MB dye removal under visible light irradiation. The results demonstrated an outstanding remarkable 99 % removal of both dyes using the binary CdS/FeS photocatalyst compared to the 50 % dye removal attained using the single CdS metal-sulphide photocatalyst.

Table 2.2: Comparative degradation efficacy of metal sulphide photocatalysts.

Metal-sulphide-based photocatalyst	Synthesis method	Light type	Degraded pollutant	Degradation efficiency	References
Ag_8S-ZnO (AZ)	hydrothermal	visible	Rhodamine B dye (RhB)	93 % AZ 55 % ZnO	(Venugopal et al., 2020)
Ag_2S-ZnO/rGO (AZ/rGO) 2 gL^{-1}	in-situ	visible	20 mgL^{-1} acetaminophen ACT	47 % AZ/rGO 27 % ZnO	(Khavar et al., 2019)
Ag_2S-ZnO/GO (AZ/GO) 0.16 gL^{-1}	sol-gel	UV	10 mgL^{-1} methyl orange (MO)	98 % AZ/GO 84 % AZ 66 % ZnO	(Khan et al., 2022)

© University of Pretoria

FeS/S-MgO (F/S-M) 0.2 gL^{-1}	high temperature sulphurisation	visible	40 mgL^{-1} tetracycline hydrochloride (TCH)	94 % F/S-M 70 % S-M	(Zheng et al., 2021)
NiS/ZnO (N/Z) 0.12 gL^{-1}	hydrothermal	UV	14 mgL^{-1} p-nitrophenol (PNP)	96 % N/Z 16 % NiS 65 % ZnO	(Pandey et al., 2022)
NiS-Mg/S-BC (NM/SBC) 0.4 gL^{-1}	high temperature sulphurisation	visible	400 mgL^{-1} rhodamine B dye (RhB)	97 % NM/S 30 % BC	(Zheng et al., 2023)
FeOOH/FeS (F/F) 0.7 gL^{-1}	one-pot hydrothermal	UV	20 mgL^{-1} Cr (VI) solution	91 % F/F 20 % FeOOH	(Guo et al., 2020)

2.5.2.1 ZnS photocatalyst

Zinc sulphide (ZnS) is an important transitional II-IV n-type group semiconductor photocatalyst. It is non-toxic, inexpensive, has good thermal stability and high electronic mobility (Isac and Enesca, 2022). ZnS has been extensively researched due to its excellent physicochemical properties, various nanosized morphologies and outstanding photocatalytic characteristics such as CO_2 photoreduction, water splitting and photodegradation of organic pollutants. ZnS has diverse applications in biodevices, flat panel displays, sensors, light-emitting diodes (LEDs), lasers, electroluminescence and infrared windows (Lee and Wu, 2017). ZnS nanocomposites effectively degrade organic pollutants under UV light irradiation (Isac and Enesca, 2022), however exhibit low photocatalytic performance under visible light irradiation (Fard et al., 2020) which makes it ineffective at longer wavelengths (Kanakaraju and Chandrasekaran, 2023). This is owing to its wide band gap energy (2.6-4.6 eV), fast charge recombination rates and is prone to photocorrosion under prolonged light irradiation (Sharma

© University of Pretoria

et al., 2021). To overcome these drawbacks, various strategies have been employed in adjustment of the band gap energy to improve its photocatalytic activity, including, metal/non-metal doping, morphology engineering, dye sensitization and heterostructures construction by combining ZnS with other semiconductors (e.g., CdS/ZnS, Ag_2S/ZnS and CuS/ZnS) (Isac and Enesca, 2022).

Table 2.3: Various degradation efficiencies of zinc sulphide photocatalysts.

ZnS-based photocatalyst	synthesis method	band gap (eV)	light type	degraded pollutant	degradation efficiency	reference
ZnS 0.5 gL^{-1}	chemical precipitation	3.21	visible	50 mgL^{-1} methy red (MR)	95 %	(Ye et al., 2018)
				Methyl orange (MO)	91 %	
				Xylenol orange (XO)	81 %	
				Methylene blue (MB)	78 %	
ZnS Ag2S/ZnS Ag2S/ZnS @rGO (AZ/rGO) 0.5 gL^{-1}	hydrothermal followed by Hummers	3.6 Z 2.7 AZ 2.4 AZ/rGO	visible	50 mgL^{-1} Cr (VI)	10 % Z 80 % AZ 95 % AZ/rGO	(Fard et al., 2020)

© University of Pretoria

ZnO/ZnS @AWA (ZZ/AWA) 0.4 gL^{-1}	vacuum impregnation	3.23	UV	40 mgL^{-1} congo red (CR)	99 %	(Zhang et al., 2022b)
ZnS/analcime (Z/a) 1 gL^{-1}	hydrothermal	2.50	UV	10 mgL^{-1} Methylene blue (MB)	98 % MB	(Abdelwahab et al., 2022)
				Orange G (OG)	71 % OG	

2.5.2.2 CuS photocatalyst

Copper sulphide (CuS) is a prominent transitional-metal I-VI p-type chalcogenide semiconductor group (Heidari et al., 2017). It has wide applications in various fields such as sensors, optical fibers, lithium-ion rechargeable batteries, solar cells, supercapacitors, photothermal conversions, thermoelectric cooling materials and as photocatalysts (Isac et al., 2019). CuS is utilised due to its remarkable ease of synthesis, morphological tunability, excellent electronic, optical and physicochemical properties (Alhaddad and Shawky, 2020). Different methods have been used to synthesise CuS (with various morphologies such as wires, rods, tubes and flowers) such as thermolysis, microwave-assistance, templating, sonochemical, spray pyrolysis and electrodeposition (Thuy et al., 2014). Copper sulphides poses multiple variants from CuS_2 (copper deficient) to Cu_2S (copper rich) including covellite CuS (Wang et al., 2020). The copper sulphide band gap energies are stoichiometry dependent, for instance, the band gaps of Cu_2S, $Cu_{1.8}S$ and CuS are 1.2 eV, 1.5 eV and 2.2 eV respectively (Yu et al., 2010). It is noteworthy that copper sulphide is active under visible light irradiation; however, rapid photogenerated charge recombination rate, instability, particle agglomeration and high susceptibility to photocorrosion are significant impediments (Alhaddad and Shawky, 2020). Therefore, strategies such as CuS encapsulation by materials with large band gap shells (Thuy et al., 2014) and heterojunction constructions with other semiconductors to overcome the aforementioned drawbacks is crucial for improved photocatalytic activity (Wang et al., 2020).

© University of Pretoria

Table 2.4: Various degradation efficiencies of copper sulphide photocatalysts.

ZnS-based photocatalyst	synthesis method	band gap (eV)	light type	degraded pollutant	degradation efficiency	reference
CuS rGO/CuS (rGO/C) 0.5 gL^{-1}	coprecipitation	2.08 C 1.90 rGO/C	visible	10 mgL^{-1} malachite green (MG)	88 % C 98 % rGO/C	(El-Hout et al., 2020)
CuS CNT/CuS (CNT/C) 3 gL^{-1}	coprecipitation	2.02 C 1.95 CNT/C	visible	5 mgL^{-1} rhodamine B (RhB)	79 % C 89 % CNT/C	(Wang et al., 2020)
CuS rGO/CuS (rGO/C) 0.8 gL^{-1}	sol-gel followed by Hummers	2.07 C 1.76 rGO/C	visible	50 mgL^{-1} atrazine (AZ)	60 % C 100 % rGO/C	(Alhaddad and Shawky, 2020)
CuS CuS/TiO2 (C/T) 1 gL^{-1}	precipitation	1.81 C 2.77 C/T	visible	30 mgL^{-1} Cr (VI)	65 % C 85 % C/T	(Wu et al., 2021)

© University of Pretoria

2.5.2.3 CuS/ZnS photocatalyst

Metal-sulphide-based nanocomposites are relatively cheap and offer exceptional physicochemical properties. ZnS and CuS among the various metal sulphides, stand out due to their low toxicity, environmental friendliness, facile preparation, and excellent optical and light-absorption properties (Varghese, 2021). A p-n heterojunction is constructed within a photocatalytic system when a p-type CuS semiconductor is combined with an n-type ZnS semiconductor. The formed p-n heterojunction promotes the interfacial charge transfer (IFCT) which consequently reduces the photoinduced charge carrier rates, and also extends the photo-absorption range which further enhances the photocatalytic performance (Harish et al., 2017). Furthermore, ZnS/CuS composites with various morphologies, such as microspheres, nanosheets, and nanoflowers, have been synthesised and demonstrated superior photocatalytic activities compared to single semiconductor photocatalysts (Feng et al., 2016). Some various CuS/ZnS fabrication methods have been extensively explored. Yu et al. (2010) and Mondal et al. (2015) synthesised CuS/ZnS composites via an ion-exchange method, while Thuy et al. (2014) and Harish et al. (2017) through a facile hydrothermal technique, and Adelifard et al. (2012) via the spray pyrolysis method. The synthesised CuS/ZnS heterojunction photocatalysts exhibited improved photocatalytic performance in the degradation of organic pollutants from wastewater.

Table 2.5: Various degradation efficiencies of CuS/ZnS photocatalysts.

CuS/ZnS-based photocatalyst	synthesis method	band gap (eV)	light type	degraded pollutant	degradation efficiency	reference
CuS/ZnS CuS/ZnS-G (CZ/G) 0.3 gL^{-1}	Hummers	3.04 CZ 2.87 CZ/G	visible	10 mgL^{-1} methylene blue (MB)	64 % CZ 90 % CZ/G	(Das et al., 2021)

© University of Pretoria

CuS/ZnS @PVP (CZ/PVP) 0.2 gL^{-1}	electrospinning	3.63 Z 2.21 C 2.01 CZ	visible	30 mgL^{-1} 4-nitrophenol (NTP)	30 % Z 70% C 100 % CZ/PVP	(Sitinjak et al., 2022)
CuS/ZnS (CZ) 0.5 gL^{-1}	cation exchange	1.45 C 3.31 Z 2.58 CZ	visible	10 mgL^{-1} tetracycline (TA)	91 % CZ	(Zhang et al., 2022a)
CuS/ZnS (CZ) 0.1 gL^{-1}	hydrothermal	3.9 Z 1.55 C 1.86 CZ	UV	10 mgL^{-1} methylene blue (MB)	4 % Z 84 % C 98 % CZ	(Feng et al., 2016)

© University of Pretoria

CHAPTER 3: MATERIALS AND METHODS

3.1 Materials

Copper (II) nitrate trihydrate [$Cu(NO_3)_2 \cdot 3H_2O$] (CAS: 10031-43-3) and thiourea [$(NH_2)_2CS$] (Batch No: 51378) were purchased from Sigma-Aldrich (St Louis, MO, United States). Zinc (II) nitrate hexahydrate [$Zn(NO_3)_2 \cdot 6H_2O$] (CAS: 10196-18-6) was purchased from Glassworld (Johannesburg, South Africa). These served as precursors for the synthesis of the ZnS, CuS, and CuS/ZnS nanocomposites. HPLC-grade rhodamine B (CAS: 81-88-9) was purchased from Sigma-Aldrich, while sodium hydroxide (NaOH, Batch No: SAAR5823200) and nitric acid (HNO_3, Batch No: OPCH000065235WO) used in pH adjustments were purchased from Glassworld. The scavenger tests were conducted using isopropyl alcohol (IPA, Batch No: 19/049) purchased from Glassworld, p-benzoquinone (pBZQ, Batch No: 1421039 55108019) purchased from Sigma—Aldrich, and benzoic acid (BA, Batch No: 1983/008079/07), and EDTA-2Na (Batch No: 83/08079/07) purchased from LabChem. All reagents were used without further purification. Deionised water (DI) was produced by an Elga Purelab Chorus unit purifier.

3.2 Catalyst synthesis

ZnS, CuS, and CuS/ZnS (5 % CuS:95 % ZnS) nanocomposites were synthesised using a novel and facile one-pot solid-phase method. In this method, stoichiometric amounts of $Zn(NO_3)_2 \cdot 6H_2O$, $(NH_2)_2CS$, and $Cu(NO_3)_2 \cdot 3H_2O$ were weighed out into a crucible using the following ratios 4: 1: 0.2 before calcining the mixture at 400 °C for 5 h. The resulting product was then ground using a pestle and mortar and sieved through a 25 µm mesh sieve to yield the final powdered photocatalyst. Pristine ZnS and CuS were synthesized in a similar fashion. Zinc (II) nitrate hexahydrate and thiourea were used to produce ZnS while copper (II) nitrate trihydrate and thiourea were mixed to form CuS. The following chemical reactions occurred, and the produced gases were emitted out and water vapourised out of the system leaving the desired products.

© University of Pretoria

$$\boldsymbol{ZnS}: Zn(NO_3)_2 \cdot 6H_2O_{(s)} + (NH_2)_2CS_{(s)} \rightarrow ZnS_{(s)} + N_2O_{(g)} + 2NO_{(g)} + 3H_2O_{(l)} \quad (1)$$

$$\boldsymbol{CuS}: Cu(NO_3)_2 \cdot 3H_2O_{(s)} + (NH_2)_2CS_{(s)} \rightarrow CuS_{(s)} + N_2O_{(g)} + CO_{2(g)} + 3H_2O_{(l)} \quad (2)$$

$$\boldsymbol{CuS/ZnS}: Zn(NO_3)_2 \cdot 6H_2O_{(s)} + Cu(NO_3)_2 \cdot 3H_2O_{(s)} + (NH_2)_2CS_{(s)} \rightarrow CuS/ZnS_{(s)} + N_2O_{(g)} + 2NO_{(g)} + 9H_2O_{(l)} \quad (3)$$

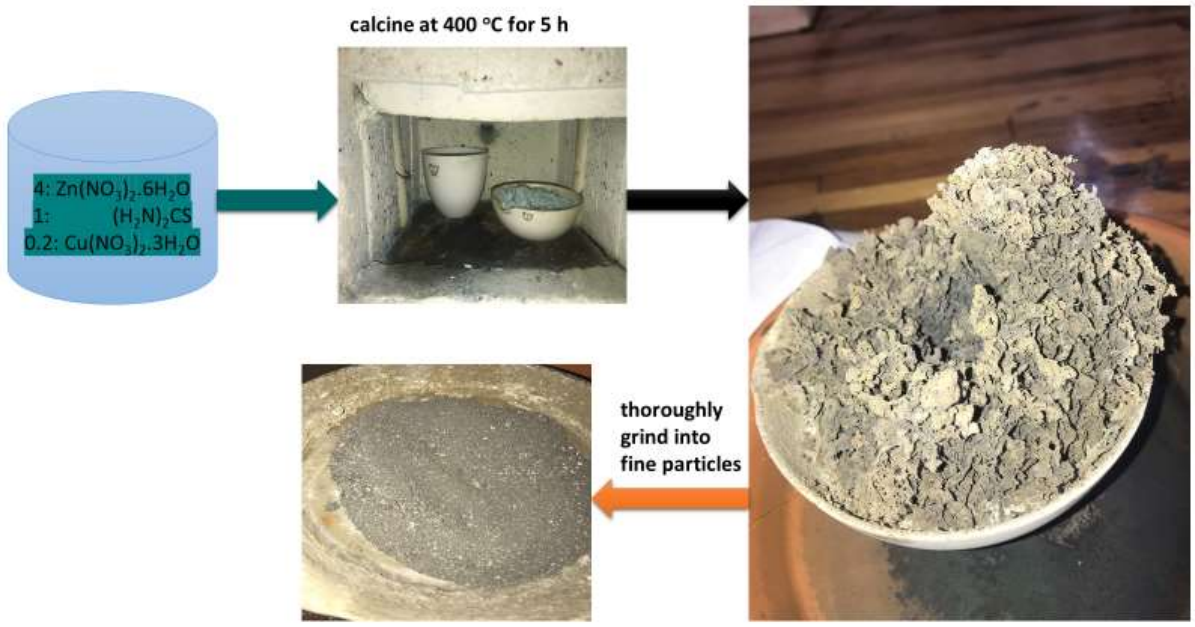

Figure 3.1: Solid phase one – pot CuS/ZnS catalyst synthesis.

3.3 Characterisation

3.3.1 X-Ray Diffraction analysis (XRD)

X-ray diffraction (XRD) spectra of catalysts were analysed using a PANalytical X'Pert Pro powder diffractometer in θ–θ configuration with an X'Celerator detector and variable-divergence and fixed receiving slits with Fe-filtered Co-Kα radiation (λ = 1.789 Å). The samples' mineralogy was determined by selecting the best-fitting pattern from the ICSD database to the measured diffraction pattern, using X'Pert Highscore plus software.

© University of Pretoria

3.3.2 X-Ray Fluorescence analysis (XRF)

The samples were prepared as pressed powders of 10 – 30 g samples mixed with 20 drops Moviol (PVA). The small aliquots of samples were prepared as boric acid pellets, pressed to 10 tons. The Thermo Fisher ARL Perform'X Sequential XRF instrument with Uniquant software was used for analyses. The software analyses for all elements in the periodic table between Na and U, but only elements found above the detection limits were reported. The values were normalised, as no loss of ignition (LOI) was done to determine crystal water and oxidation state changes. A standard sample material was prepared and analysed in the same manner as the samples and is reported as such.

3.3.3 Scanning Electron Microscopy and Energy Dispersive Spectroscopy (SEM/EDS)

The images of the structure and morphology of the synthesised nanoparticles were captured on a Zeiss Ultra PLUS FEG SEM using the Oxford instruments detector and Aztec 3.0 software SP1. The sample powders were uniformly dispersed on a carbon tape firmly attached to an aluminium plate and compressed air was used to blow off any excess. A SEM auto-coating unit E2500 (Palaron Equipment Ltd) sputter coater was then used three times for carbon coating. Elemental analysis and sum spectrum mapping of constituent elements were done using a SEM-EDS instrument with an APEX software.

3.3.4 Transmission Electron Microscopy (TEM)

The nanoparticles' high-resolution images were captured using a JOEL JEM 2100F, 200kV analytical electron microscope. The instrument has an electron gun device that illuminates electron beams which is integrated by a scanning device consisting of annular dark-field and bright field (A-DF/BF) detectors. The samples were then placed on a Formvar film used to

© University of Pretoria

support ultrathin sections on mesh grid. The film is coated with a light carbon layer for its stabilisation during electron beam exposure.

3.3.5 Brunauer-Emmett-Teller (BET)

A micrometrics Tristar II 3020 Version 3.02 BET system was used in measurement of the surface area and pore size distribution. The conditions included nitrogen analysis adsorptive with liquid nitrogen temperature of 77.350 K at equilibration interval of 5 sec. the samples were degassed and dried overnight prior BET analysis at 100 ºC under pure nitrogen flow for elimination of all water molecules.

3.3.6 Ultraviolet-Visible Spectrophotometer (UV-Vis)

A UV-Vis spectrophotometer Hitachi U-3900 single monochromatic double-beam system using UV-solutions software program was used to measure the optical absorption spectra of the synthesised particles. The wavelength scan recorded in the range 200 nm to 500 nm at a scan speed of 600 nmmin^{-1}, with sampling interval at 1 nm and lamp change wavelength at 340 nm. Nanopowders were suspended in deionised water prior analysis. Deionised water was initially added to clean cuvette then transferred to the sampling compartment to serve as a blank.

3.4 Analytical methods

3.4.1 UV-Vis spectrophotometer

RhB dye progressive degradation in water was measured using a Labotec UV/Vis Lightwave II spectrophotometer. The degradation of RhB dye was evaluated by referring to calibration curves of prepared standards, as illustrated in Figure 3.2.

© University of Pretoria

Table 3.1: Absorbance values of the prepared standards.

Concentration (ppm)	Run 1	Run 2	Run 3	Run 4	Run 5	Average absorbance (a.u.)
100	0.993	0.99	0.988	0.987	0.988	0.9892
70	0.744	0.743	0.741	0.74	0.741	0.7418
50	0.61	0.607	0.606	0.604	0.608	0.607
30	0.343	0.343	0.34	0.339	0.339	0.3408
10	0.132	0.13	0.131	0.129	0.127	0.1298
5	0.098	0.098	0.099	0.095	0.095	0.097

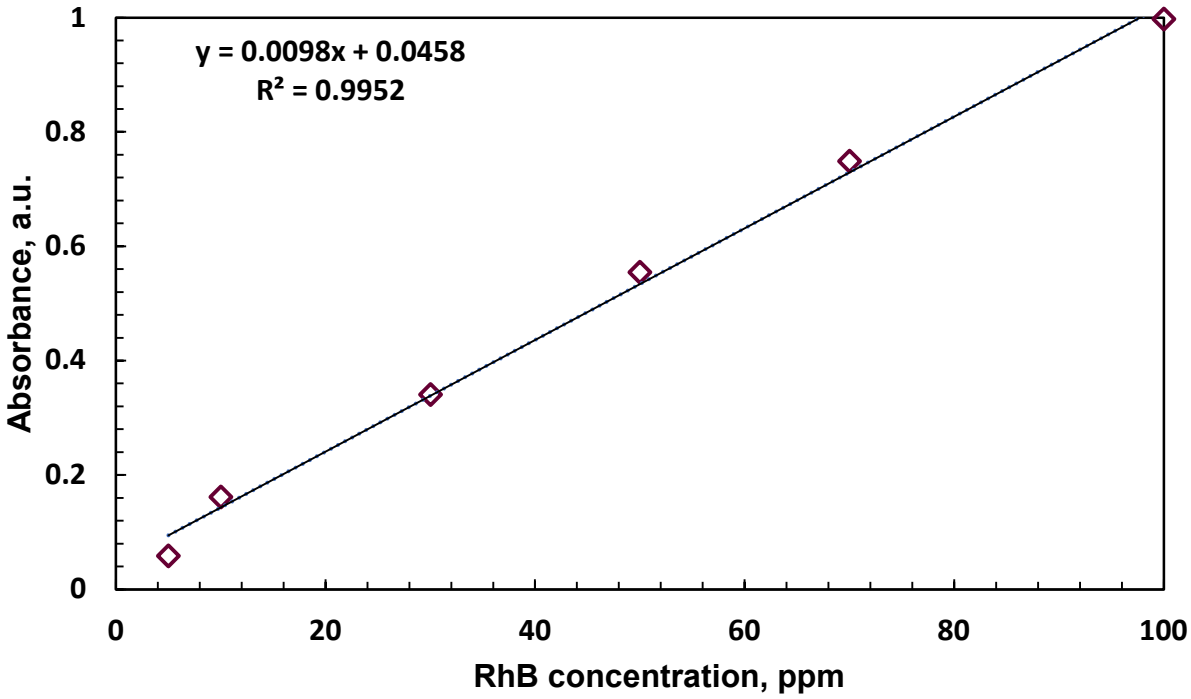

Figure 3.2: Calibration curve for RhB dye detection.

© University of Pretoria

3.5 Degradation studies

The photodegradation efficiency of the synthesised photocatalyst was investigated on the decontamination of textile wastewater in the presence of visible light. RhB dye was used as the model organic pollutant. The study utilises a modelled dispersed suspension reactor that was a designed for laboratory scale water treatment.

The photocatalytic activity of the synthesised nanomaterials was investigated by dispensing predetermined amounts of CuS/ZnS in 100 mL of 5 ppm RhB dye solution. This suspension was continuously stirred in the dark for 30 min in order to attain adsorption–desorption equilibrium prior to subsequent 4 h visible-light irradiation. Aliquot samples of 2 mL were withdrawn every 30 min and centrifuged. The resulting solution was passed through 0.45 µm simplepure filters before analysis. Control photolysis and adsorption tests were also conducted under the same conditions. Optimisation studies were conducted to determine optimum photodegradation conditions while varying CuS/ZnS loading (0–15 g L^{-1}), initial RhB dye concentration (5–100 ppm), and initial solution pH (1–13), which was adjusted using 0.1 M HNO_3 and 0.1 M NaOH. A WPA, LIGHT Wave, Labotech UV-vis spectrophotometer was used to analyse the change in RhB dye concentration at a characteristic wavelength of 554 nm using deionised water as a reference (blank). The achieved photodegradation percentage was determined using the following Equation (4):

$$\%\ Degradation = \frac{(C_o - C_t)}{C_o} \times 100 \quad (4)$$

Where C_o is the initial RhB concentration and C_t is RhB concentration after irradiation time, t.

Furthermore, various scavenger tests were conducted to determine the most reactive oxidation species. This was performed through the addition of 5 mmol L^{-1} of benzoic acid (BA for e^- C_B), isopropyl alcohol (IPA for OH• radicals), Ethylenediaminetetraacetic acid disodium (EDTA-2Na for h^+ V_B), and p-benzoquinone (p-BZQ for $O_2^{\bullet}$ radicals). Recyclability tests were

© University of Pretoria

conducted to investigate the stability of the binary CuS/ZnS. In these tests, a sample was withdrawn after each run for analysis whilst the remaining solution was centrifuged and decanted. The collected catalyst particles were dried at 50 °C overnight and then dispersed into a fresh RhB solution for another run.

© University of Pretoria

CHAPTER 4: PHOTOCATALYSTS CHARACTERISATION

A general and in-depth study of the synthesised photocatalysts physicochemical properties were characterised using several characterisation techniques. This investigation was conducted on pristine ZnS, CuS and CuS/ZnS composite catalyst to also validate the route of synthesis.

4.1 Catalyst Phase Analysis

Figure 4.1 shows the XRD patterns of the prepared ZnS, CuS, and CuS/ZnS nanoparticles. The ZnS XRD diffractogram exhibits diffraction peaks at 32°, 47°, and 56° corresponding to the (102), (112), and (205) planes of the cubic ZnS phase (JCPDS card no: 89-2194). CuS possessed peaks at 29°, 31°, 47°, and 58° corresponding to the (016), (103), (107), and (116) planes of the hexagonal CuS phase (JCPDS card no: 24-0060). The noted diffraction peaks between 12° and 29° and at 80° (represented by asterisks) in the CuS/ZnS nanocomposite corresponding to the (100), (101), and (102) planes (JCPDS card no: 78-0876) can be identified as characteristic CuS peaks. It is noteworthy that the characteristic peaks of pristine ZnS and the CuS/ZnS composite catalyst were almost identical. This was attributed to the low concentrations of the CuS, which is the dopant material used in the synthesis of the binary composite. The CuS nanoparticles were highly amorphous with smeared broad diffraction peaks caused by small crystalline sizes estimated to be about 11 nm. The broadened CuS peaks and reduced intensities suggest a decline in particle size and crystallinity (Hong et al., 2015). The CuS/ZnS spectra reveal a combination of both CuS and ZnS nanomaterials, indicating the successful formation of the CuS/ZnS nanocomposite (Mondal et al., 2015). The characteristic distinct diffraction peaks of the materials confirmed the crystalline nature and the relative purity of the synthesised catalysts. The average crystallite size (D) of the nanomaterials was calculated using the Debye–Scherrer equation.

$$D = \frac{k\lambda}{\cos\theta} \qquad (5)$$

© University of Pretoria

where k is a constant (0.96), λ is the wavelength of the X-ray (0.15418 nm) Cu Kα radiation (1.5406 Å), β denotes the full width at half maximum (FWHM) in radians of the specific peaks, and Θ designates the Braggs diffraction angle in degrees. The average crystallite sizes of the ZnS, CuS, and CuS/ZnS nanocomposites are approximately 14 nm, 7 nm, and 17 nm, respectively. The broadening observed in the diffraction peaks, particularly the CuS spectra, is attributed to the small crystallite size (Yu et al., 2010). Additionally, an increase in the diffraction peak intensity implies a decrease in FWHM and vice versa. This produces crystal defects in the dopant region and, consequently, a generation of charge imbalance (Sreelekha et al., 2016).

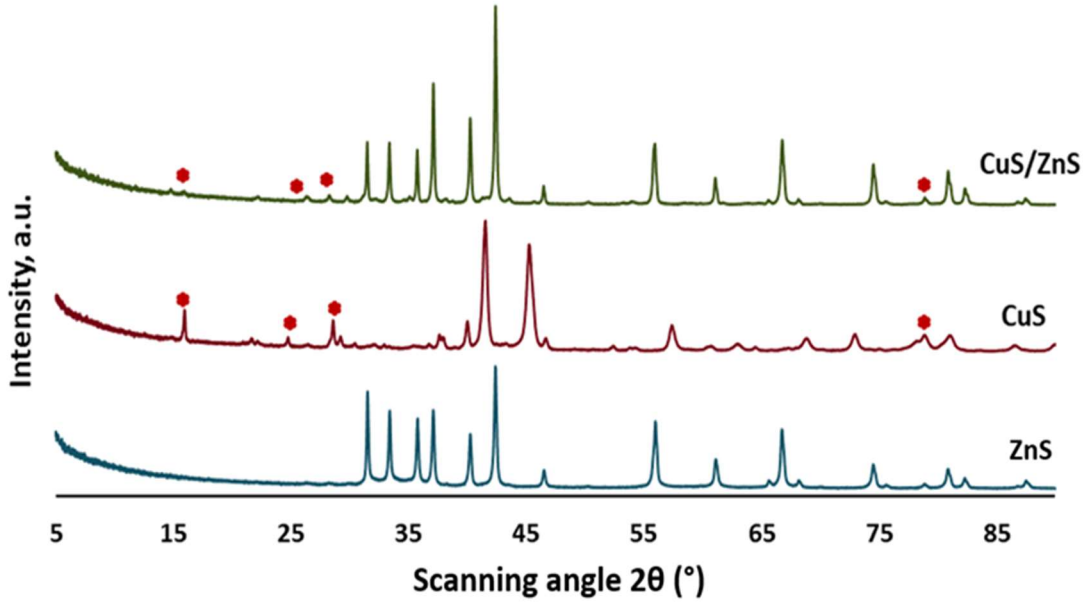

Figure 4.1: XRD patterns of the pristine ZnS and CuS as well as the CuS/ZnS composite.

4.2 Elemental composition

XRF was used to determine the elemental composition and purity of the synthesised catalyst materials, and the results were reported in Table 4.1. The analysis showed that the catalysts had a relative high purity of about 99 % from the composition of the main components of the nanomaterials. The observed XRF material results ratios matched those used during material

© University of Pretoria

synthesis, confirming the successful synthesis of ZnS, CuS, and the binary CuS/ZnS nanocomposites with ratios of 4:1 (Zn:S), 1:5 (Cu:S), and 4:1:0.2 (Zn:S:Cu), respectively.

The covellite catalyst was found to have a high copper content of approximately 80.30 %, while the binary CuS/ZnS catalyst had a low copper content of 3.87 %. This supports the presence of copper, which had little detection in the XRD analysis.

Table 4.1: X-ray florescence data for synthesised materials.

Component	ZnS	CuS	CuS/ZnS
Zn	79.38	3.08	76.02
Cu	0.04	80.30	3.87
S	19.79	16.01	18.88
Na_2O	0.46	0.51	0.95
MgO	0.21	-	0.20
Al_2O_3	0.07	0.07	0.04
CaO	0.05	0.03	0.04
TOTAL	100	100	100

4.3 Catalyst morphology

Scanning electron microscopy was used to capture and analyse the morphologies of the synthesised ZnS, CuS, and CuS/ZnS as illustrated in Figure 4.2. The insets in Figure 4.2a–c depict the synthesised ZnS, CuS, and CuS/ZnS nanomaterials as mixtures of porous agglomerates covering their surfaces with wide particle size distribution. The agglomeration evidenced in all the materials was likely due to high-temperature annealing conditions used during catalysts synthesis (Mondal et al., 2015). The TEM images presented in Figure 4.2d–f confirm that these agglomerates were in fact composed of a mixture of nanosphere- and nanoplatelet-shaped primary particles. The captured TEM images further reveal successful CuS/ZnS heterojunction formation as the CuS nanospheres were auspiciously embedded in the ZnS nanoplatelet nanostructures. It has been reported that particle morphology plays an important role in photocatalytic activity as it influences the rate of electron–hole recombination (Moja et al., 2021). Additionally, the nanosized nature of the particles enhances the specific

© University of Pretoria

surface area of the catalysts, which in turn affects the photodegradation efficacy (Varghese, 2021).

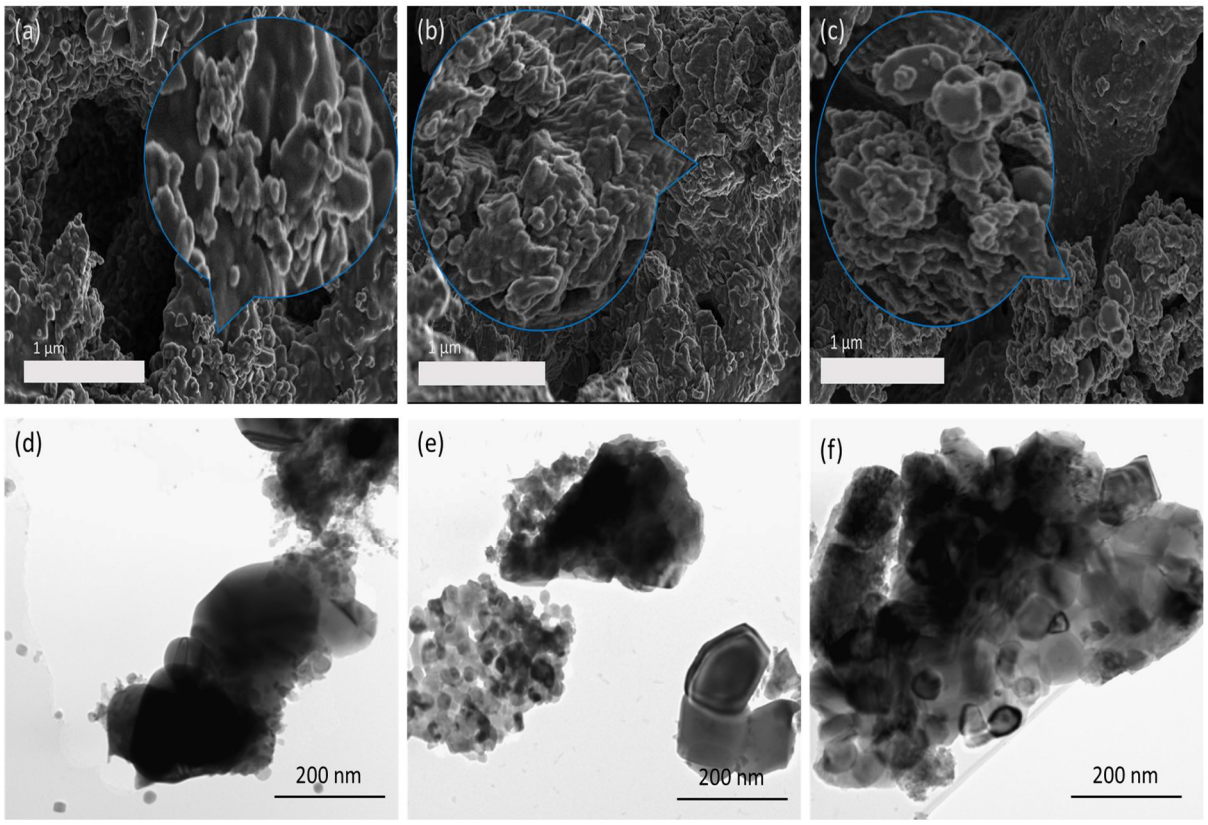

Figure 4.2: SEM images of (a) ZnS, (b) CuS, and (c) CuS/ZnS, and TEM images of (d) ZnS, (e) CuS, and (f) CuS/ZnS.

4.3 Elemental mapping and distribution analysis

Figures 4.3 depict the results derived from employing EDS analysis for the assessment of EDS spectra and elemental mapping. The EDS spectra analysis in Figure 4.3 (a) confirms the presence of zinc and sulphur, Figure 4.3 (b) validates the presence of copper and sulphur, while Figure 4.3 (c) attests to the existence of zinc, copper, and sulphur within the synthesised ZnS, CuS, and the binary CuS/ZnS catalysts. Notably, the EDS spectra provide supplementary evidence of the presence of copper in the synthesised CuS/ZnS, which was barely detectable in its XRD spectra, that was predominantly dominated by ZnS. Furthermore, the mapping

© University of Pretoria

images of the different synthesised nanocomposites vividly illustrate the homogeneous even distribution of elements within the material.

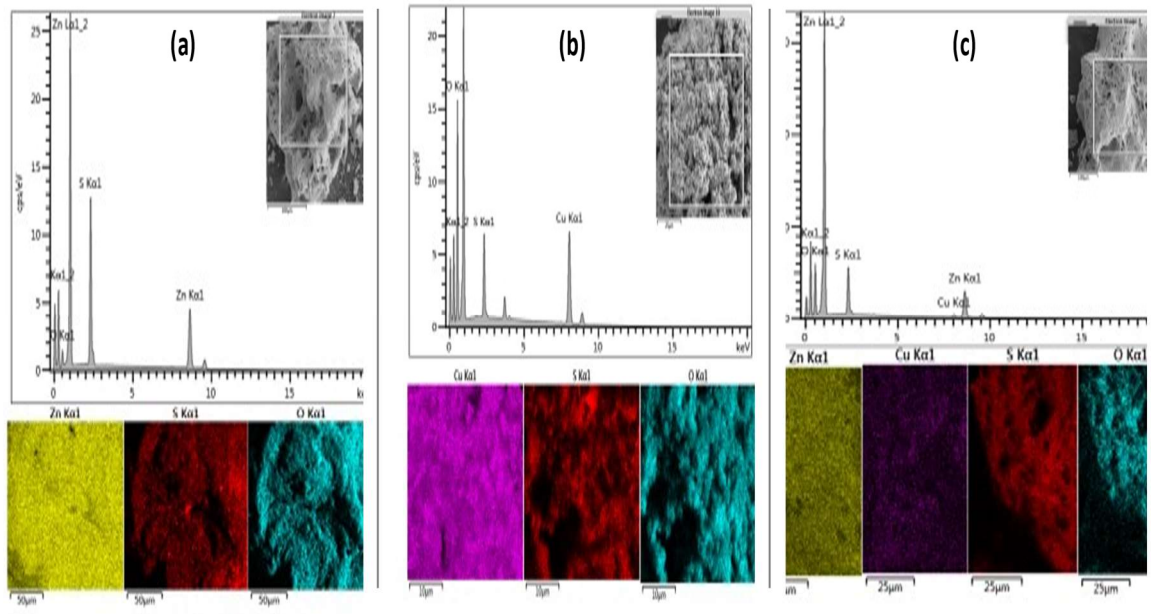

Figure 4.3: EDS elemental analysis and mapping of (a) ZnS, (b) CuS, and (c) CuS/ZnS.

4.4 Surface area and pore size analysis

The surface area and the pore size distribution of the ZnS, CuS, and CuS/ZnS nanocomposites were analysed using the BET analysis. The results presented in Table 4.2 further prove that the synthesised materials contained a mixture of mesoporous structures, which supports the mixture of pores observed in the SEM image insets. Large mesopores were observed, recording an average pore size of 12.03 nm (ZnS) and 11.22 nm (CuS); however, smaller mesospheres with an average pore size of 8.57 nm were obtained for the composite CuS/ZnS catalyst. Additionally, the surface areas for the pristine ZnS and CuS were 4.06 m^2 g^{-1} and 8.73 m^2 g^{-1}, while that of the CuS/ZnS was 2.72 m^2 g^{-1}. Rameshbabu et al. (2019) reported similar observations with pure ZnS having a high surface area that decreased upon loading CuS onto the surface of ZnS. According to Hong et al. (2015), as the CuS dopant amount increases beyond 3 %, the pore size and surface area decrease, resulting in pore blockage when loaded with increased CuS. In the synthesis of the CuS/ZnS binary composite for this study, about 5 % of CuS as the dopant material was utilised based on stoichiometric calculations. The decrease

© University of Pretoria

could also be a result of the high calcination temperatures used in the combustion synthesis method, and hence particle fusion resulting from the formation of agglomerates as depicted by the catalyst surface characterisation (Mzimela et al., 2022). The broad characteristic peaks observed in the XRD spectra of the constituent materials suggest a decreased crystallinity, which can be attributed to their high surface area and pore size. The specific surface area and porosity of photocatalysts significantly influence the visible-light activity and pollutant absorption of CuS/ZnS, thus improving its overall photocatalytic performance (Varghese, 2021).

Table 4.2: BET analysis surface area and pore size distribution of sorbents.

Materials	Surface area (m^2g^{-1})	Average pore size (nm)	BJH Adsorption (4V/Å)*	BJH Desorption (4V/Å)*
ZnS	4.06	12.03	73.47	75.61
CuS	8.73	11.22	60.68	82.43
CuS/ZnS	2.72	8.57	51.35	54.38

*Average pore width

Figure 4.4 depicts the nitrogen adsorption–desorption isotherms of the prepared catalysts. The isotherms of these catalysts can be characterised using the International Union of Pure and Applied Chemistry (IUPAC) classification as Type 4 with H3 hysteresis loops, which confirm the synthesis of mesoporous materials whilst the step-down of the curves represent the spontaneous evaporation of the metastable pore liquid, also known as “cavitation” (Ichipi et al., 2022). The isotherms shown in Figure 4.4 demonstrate high adsorption levels, particularly in the hysteresis loops observed at high relative pressures ranging between 0.8 and 1.0 p/po. These hysteresis loops are characterized as type H3, which indicates the presence of non-rigid aggregates of plate-like particles giving rise to slit-like pores in the materials (Yu et al., 2010).

© University of Pretoria

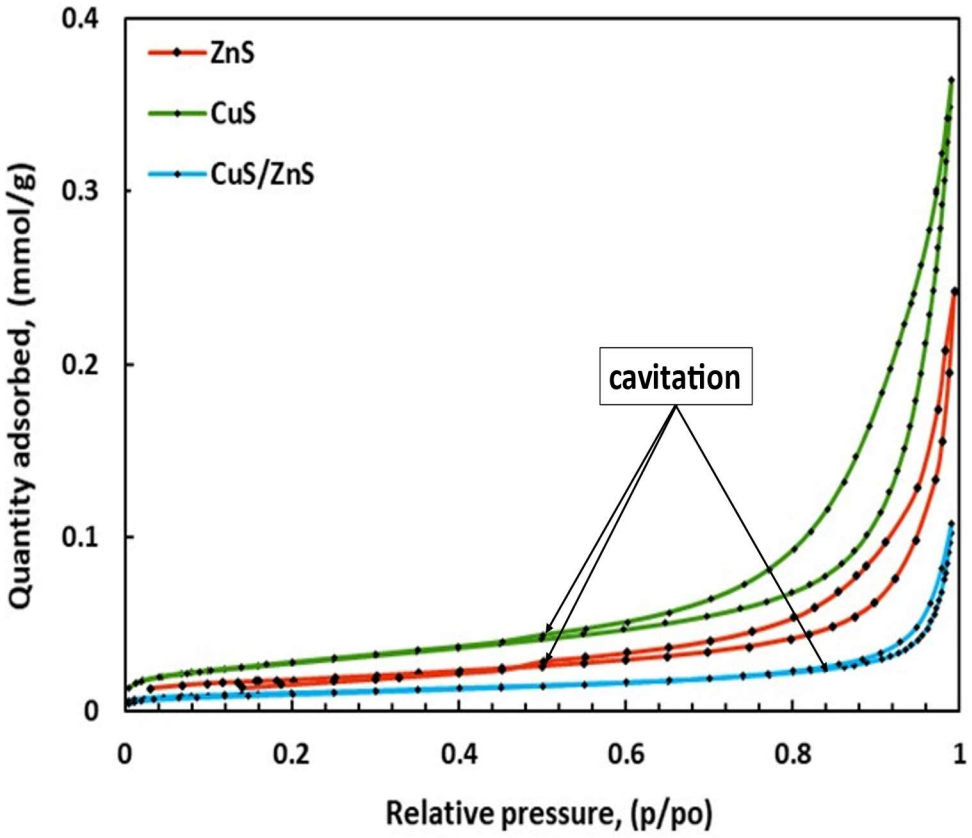

Figure 4.4: N_2 adsorption – desorption isotherm of synthesised catalysts.

4.4 Photo-absorption and band gap analysis

The optical absorption properties of the prepared photocatalysts were analysed by a UV-Vis diffuse reflectance spectroscopy (DRS) and the results are shown in Figure 4.5. The broad peaks between 339 nm and 378 nm can be attributed to the intrinsic bandgap absorption of ZnS due to transition of electrons from the valence band to the conduction band. The absorption edge for CuS ranges from 300 nm to 800 nm with an infinitesimally slight peak observed at about 588 nm, which is in the visible-light region and can be attributed to Cu^{2+} d-d transition as closely reported by Yu et al. (2015), Huang et al. (2015), and Rameshbabu et al. (2019). The coupling of minute CuS quantities to ZnS enhanced the visible-light absorption properties of ZnS and resulted in improved photocatalytic activity noted from the binary CuS/ZnS photocatalyst. It can therefore be postulated that the heterojunction formation between ZnS and CuS resulted in increased absorption in the visible range.

© University of Pretoria

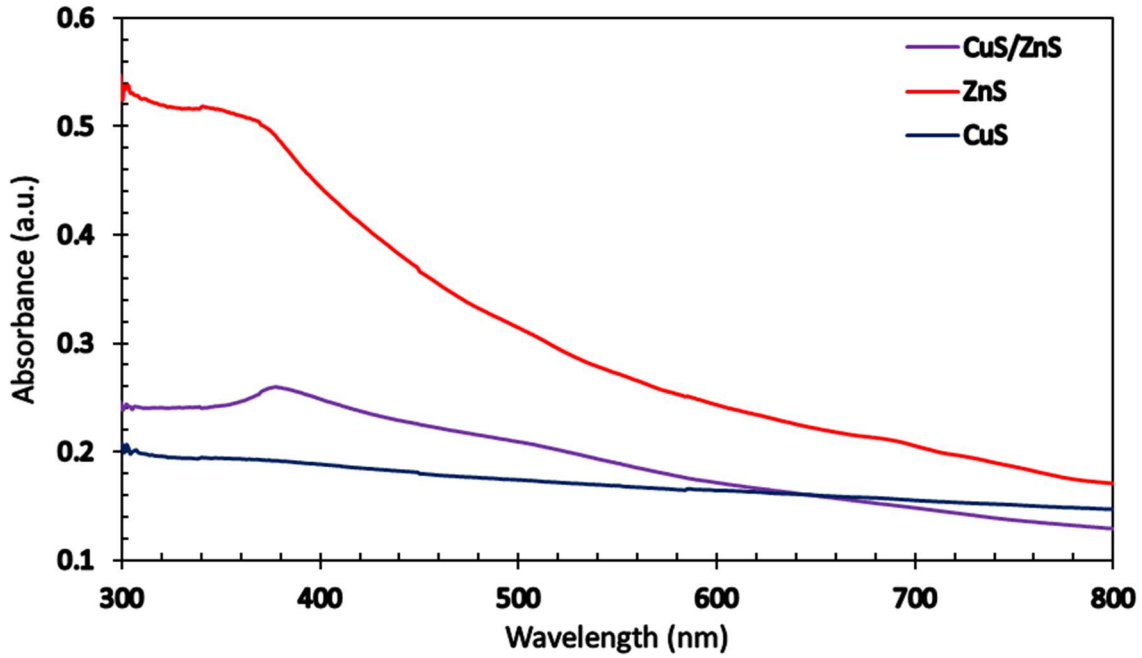

Figure 4.5: UV – vis absorption spectra of synthesised nanoparticles.

4.4.1 Optical band gap measurement

The electronic state and bandgap energies of the synthesised nanocomposites were determined from the obtained spectrum data using the UV-Vis DRS differential curves as depicted in Figures 4.6 – 4.8. Band gap energies of each catalyst material were estimated using absorbance Tauc plots based on equation 6.

$$(\alpha hv)^n = A(hv - E_g) \qquad (6)$$

where α is the absorption coefficient, h is Plank's constant, v is the photon frequency, A is the proportionality constant, hv is photon energy, E_g is the bandgap energy, and n is semiconductor electronic transition where n = 2 for direct allowed transitions and n = $1/2$ for indirect allowed transitions. The bandgap energy for each of the catalysts was estimated using plots of $(\alpha hv)^{1/2}$ against E_g as they all had indirect bandgaps.

© University of Pretoria

The bandgap energies of the synthesised ZnS, CuS, and CuS/ZnS were determined to be 2.55 eV, 1.7 eV, and 2.0 eV, respectively. These values are consistent with those reported by Rameshbabu et al. (2019) for ZnS at 2.54 eV and CuS at 1.70 eV. The improved visible-light photocatalytic activity of CuS/ZnS can be attributed to the incorporation of Cu^{2+} ions into the ZnS lattice, which leads to the formation of CuS nuclei on the surface of ZnS and the subsequent production of a CuS/ZnS heterojunction. This effect has also been observed by Mondal et al. (2015), who reported a reduced bandgap energy from 3.35 eV up to 1.21 eV for the prepared CuS/ZnS composites. It is possible that this shift in bandgap energy is a result of the quantum non-confinement effect of CuS/ZnS nanocomposites, as reported by Adelifard et al. (2012).

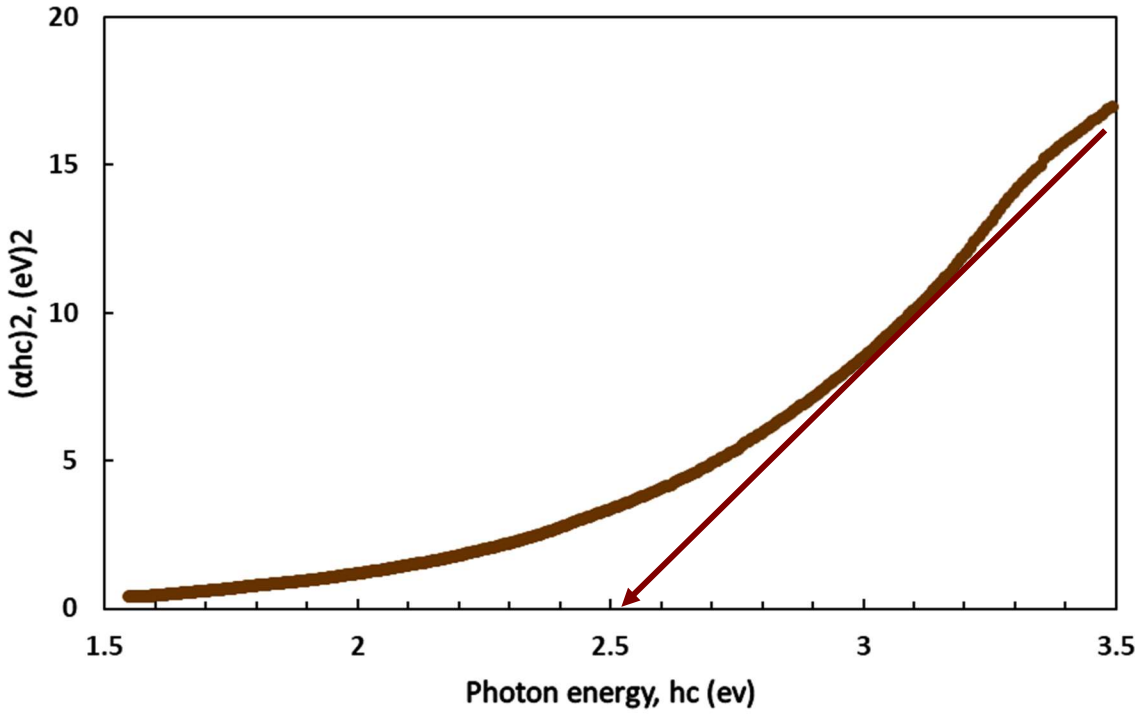

Figure 4.6: Tauc plot and estimated band gap for ZnS.

© University of Pretoria

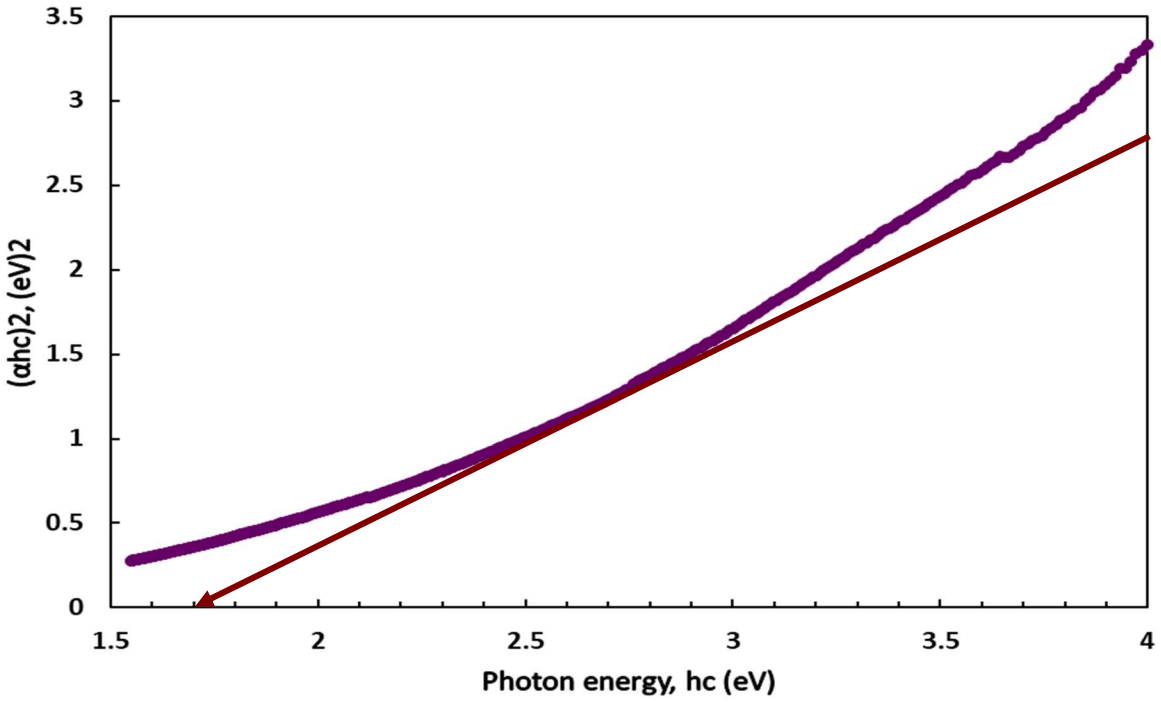

Figure 4.7: Tauc plot and estimated band gap for CuS.

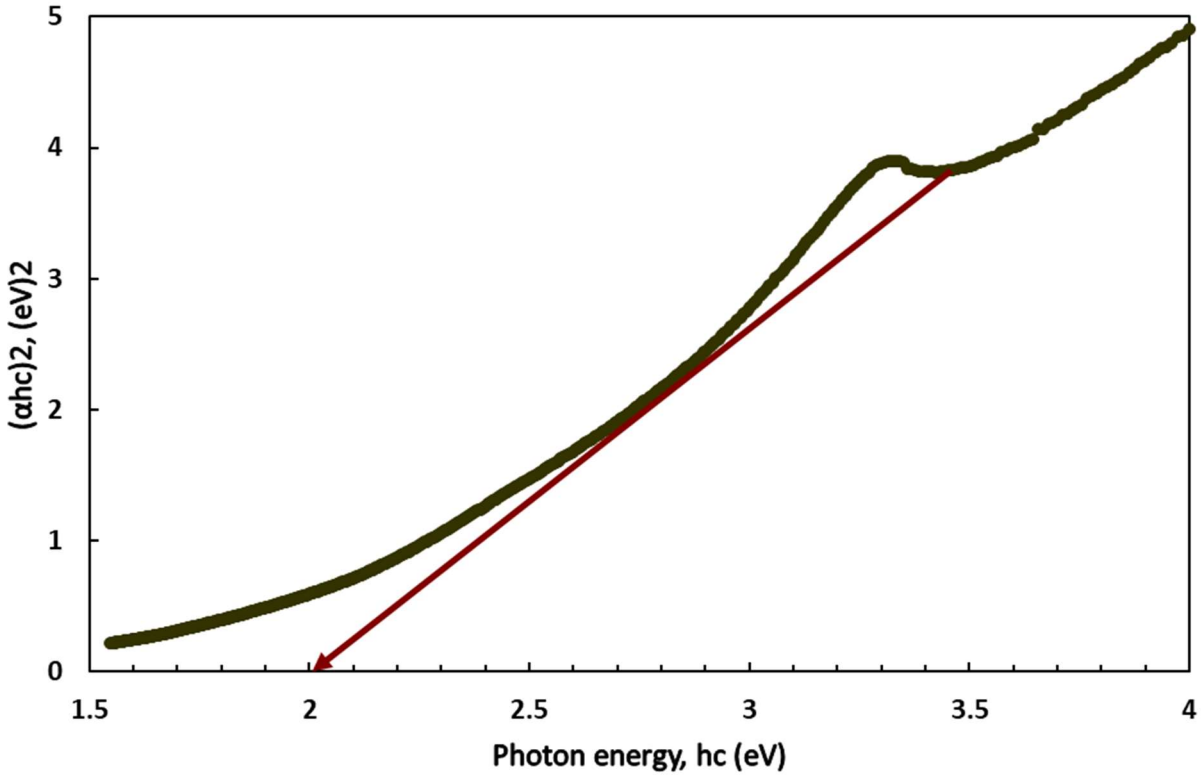

Figure 4.8: Tauc plot and estimated band gap for CuS/ZnS.

© University of Pretoria

CHAPTER 5: DEGRADATION IN-DEPTH STUDIES

The photocatalytic potential of the synthesised catalysts was evaluated in RhB dye degradation under visible light irradiation (ZnS, CuS and CuS/ZnS). Each synthesised catalyst has a unique band gap energy that is activated by different light types based on the spectrum wavelength.

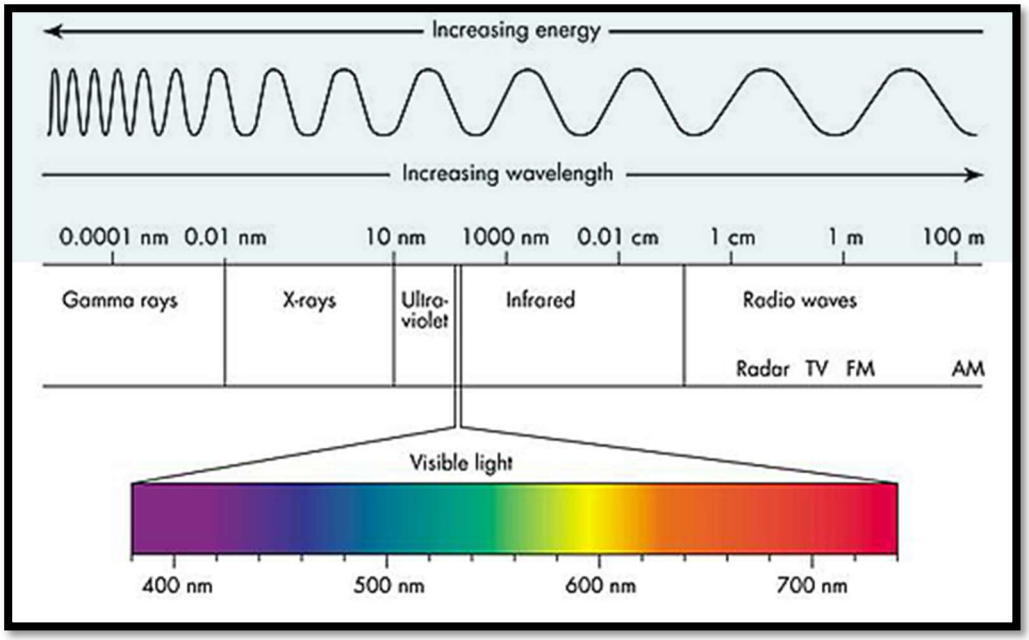

Figure 5.1: Solar spectrum with respective wavelengths (Cyberphysics- Electromagnetic Spectrum, 2022).

5.1 Visible light photodegradation study

All experiments were tested using only visible light for 4.5 h in congruence with the hypothesis of this research. Three 18 W fluorescent day-light lamps (500 nm – 650 nm) were employed which served as the visible light irradiation source. The effect catalyst constituents and effect of intrinsic parameters such as catalyst loading, initial solution concentration and pH was investigated on the model pollutant, RhB dye.

© University of Pretoria

5.2 Photocatalytic performance

The photocatalytic activity of the synthesized catalyst was evaluated by investigating its ability to degrade RhB under visible-light irradiation. Control experiments were performed to assess the impact of visible light alone (photolysis) and the adsorption capacity of the catalyst in the absence of light on RhB dye. The photolysis test did not result in any degradation, while the adsorption experiment showed significant dye removal, with 67 % removed after 4.5 h of contact time. However, the CuS/ZnS photocatalyst exhibited a remarkable degradation efficiency of 97 % under photocatalytic conditions with visible-light irradiation for the same duration. These findings (Figure 5.2) suggest that the degradation of RhB dye depends on the presence of a photocatalyst and exposure to light, both of which are crucial components of the photocatalytic degradation process. Light provided the necessary energy to generate reactive electron–hole pairs, whereas the prepared photocatalyst proved capable of absorbing light energy and utilising it to promote surface chemical reactions.

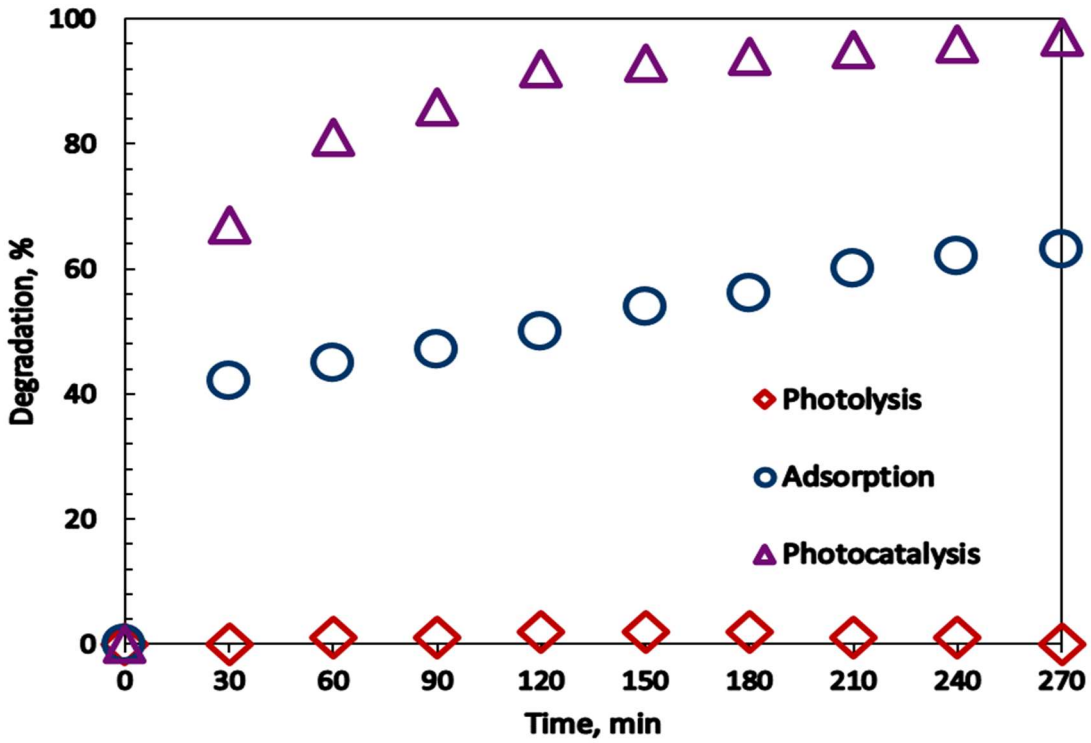

Figure 5.2: Control tests and photocatalysis of CuS/ZnS under visible light irradiation.

© University of Pretoria

5.2.1 Effect of individual catalyst composites

The photocatalytic degradation efficiencies of the composite catalysts as well as those of the individual constituents were investigated using 10 g L^{-1} loading of the relevant catalyst on a 5 ppm RhB solution at pH 5. The resulting slurry was stirred continuously for 30 min in the dark in order to establish adsorption–desorption equilibrium prior to a subsequent 4 h of visible-light irradiation. All three catalysts presented fairly high adsorption capacities, with CuS resulting in 23 % dye removal after the initial 30 min in the dark which increased to 91 % upon visible-light irradiation, followed by ZnS with 40 % dye removal, which increased to 67 %, and CuS/ZnS adsorbing 67 % of the RhB dye, which further increases to 97 % upon visible-light irradiation (Figure 5.3). The results showed that the constituent materials (CuS and ZnS), however, performed well in the dark as adsorbents due to their surface chemical properties, selective adsorption properties, and high surface area (supported by Table 4.2). Additionally, the achieved high surface-area-to-volume ratio implies an adsorption of large contaminant (RhB dye) amounts per unit mass. The photocatalytic enhancement of CuS/ZnS can be attributed to several effects: (i) reduced e^{-}/h^{+} pair recombination rate because of interface existence between these two phases due to C_B and V_B energy level differences, and (ii) the composite possesses a nanoporous structure that allows for more efficient transport of the reactant molecules of RhB dye onto the available active sites (Yu et al., 2010). Harish et al. (2017) reported the same phenomena where the photoactivity of the nanomaterials was tested on MB dye under visible light and the results reported 89.70 % removal with ZnS, 61.05 % with CuS, and a significant 95.51 % MB dye degradation after incorporating CuS into the composition in a heterojunction formation.

© University of Pretoria

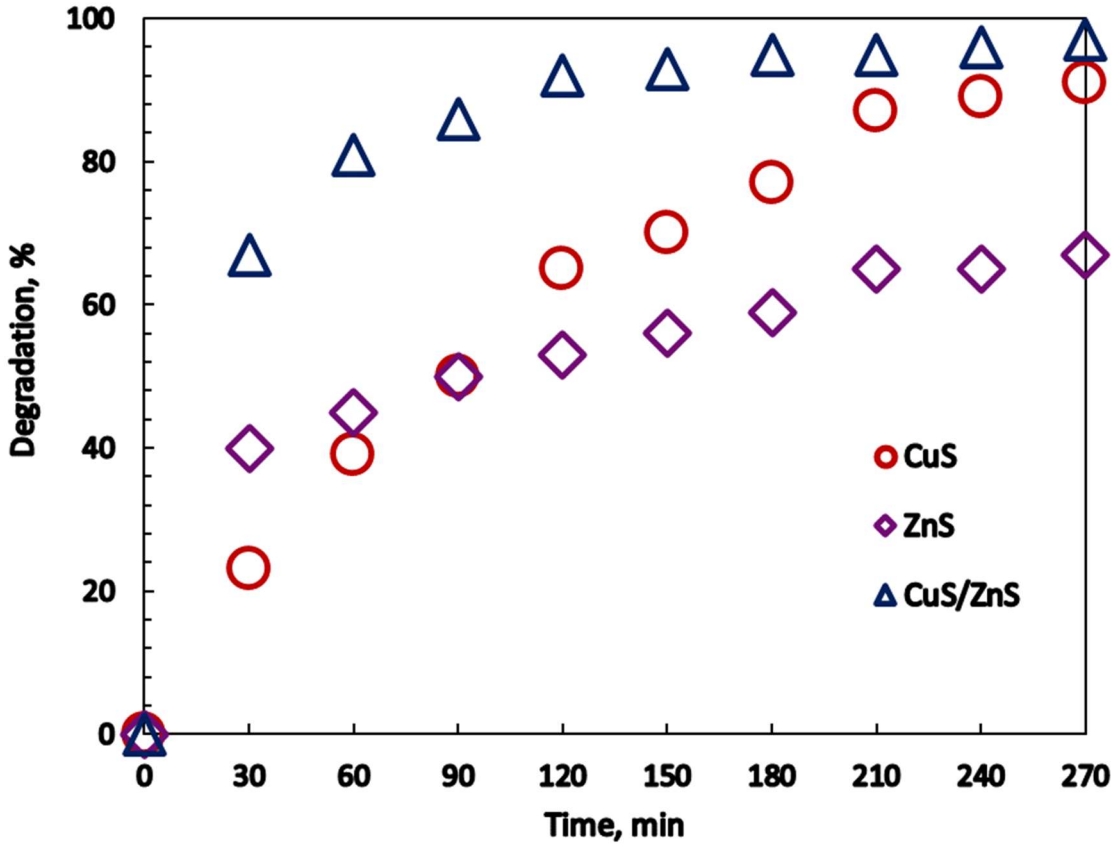

Figure 5.3: Performance of 10 gL^{-1} constituent catalyst on 5 ppm RhB dye solution.

5.2.2 Effect of initial pH

The solution pH is an important parameter that affects the photocatalytic performance of semiconducting metal sulphides. The surface charge of the photocatalyst and speciation of the target pollutant are influenced by pH, which in turn affects the subsequent adsorption and photocatalytic processes (Alshamsi et al., 2021). Figure 5.4 illustrates the effect of varying initial solution pH from acidic to basic conditions. The initial RhB solution pH is adjusted by adding an appropriate amount of NaOH or HNO_3. The photocatalytic performance of the prepared CuS/ZnS nanocomposites is investigated at pH 1, 3, 5, 7, 9, 11 and 13. The highest degradation was achieved at pH 1 with complete (100 %) RhB removal. The pH of 11 had the next best degradation (98 %) followed by pH 13 (91 %), then pH 3, pH 5 and pH 7 having the same degradation (89 %) and pH 9 achieving the least removal. Photocatalysis can be described as surface phenomenon initiated mostly through adsorption followed by catalysis under light

© University of Pretoria

irradiation (Anjum et al., 2017). Depending on the net surface charge of the catalyst surface, adsorption can either be low due to repulsion between the surface of the catalyst and pollutant with the same polarity or high due to opposite charges attraction (Tichapondwa et al., 2020). More H• radicals are formed in acidic conditions due to H^+-electron interaction thereby leading to highly reactive HO^- radicals formation due to hydrogen peroxide dissociation. These highly reactive hydroxyl radicals yielded outstanding effective RhB degradation. The hydroxyl ion concentration increases in basic conditions thereby reacts with h^+ (positively charged holes) to form highly reactive •OH. The presence of these hydroxyl radicals directly affects RhB removal (Varghese, 2021).

The kinetic analysis was subsequently conducted to further assess the synthesised photocatalysts' degradation proficiency. The Langmuir–Hinshelwood kinetic model expression shown in Equation (7) was used to determine the k_{max} values.

$$k_{max}t = In\left(\frac{C_o}{C_t}\right) \quad (7)$$

where k_{max} is the pseudo-first-order rate constant, and C_o and C_t are RhB concentrations at t = 0 and time "t", respectively. The dye degradation kinetics are best described using a pseudo-first-order model in the pH range of 3 to 11, with R^2 values higher than 0.96 being observed. However, extreme pH values of 1 and 13 did not fit this model well, with R^2 values less than 0.84 reported (Figure 5.4). The average rate constant was 0.0106 min^{-1}, although some outliers at pH 1 and pH 11 were observed around 0.0224 min^{-1} and 0.0137 min^{-1}, respectively.

© University of Pretoria

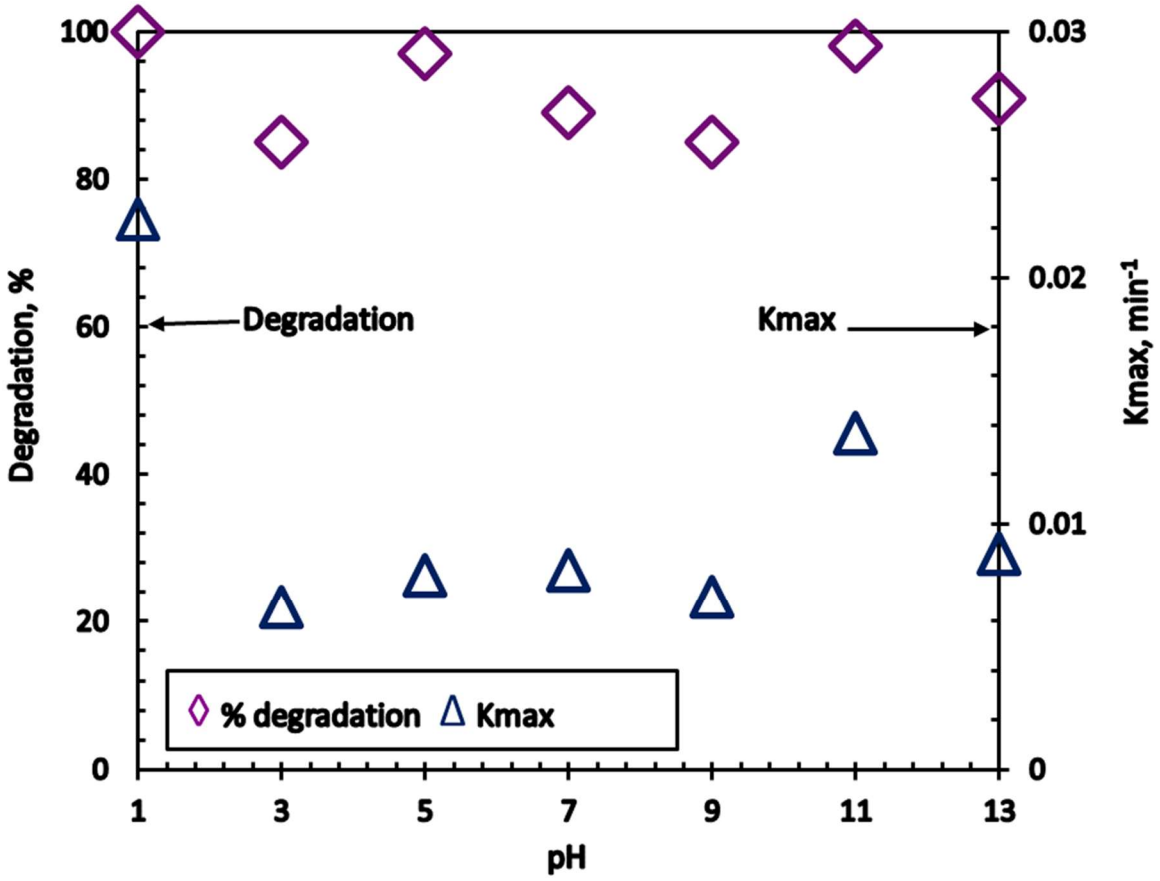

Figure 5.4: Reaction kinetics and effect of initial pH in RhB dye degradation with CuS/ZnS photocatalyst.

5.2.3 Effect of catalyst loading

Catalyst dosage has a significant impact on the efficiency of the photocatalytic process. Figure 5.5 shows how the photocatalytic activity of CuS/ZnS nanocomposites in RhB dye removal varies with different catalyst loadings. The results demonstrate a clear enhancement in the photocatalytic activity of CuS/ZnS with an increase in catalyst loading. The optimum catalyst loading was found to be 10 g L^{-1} as per the conducted investigation, beyond which there was a decrease in the photodegradation efficiency. The increase in efficiency with increasing catalyst loading up to the optimum value can be attributed to an increase in the quantity of absorbed photons and the quantity of adsorbed RhB dye molecules. However, beyond the optimum value, particle agglomeration and high suspension turbidity hindered light penetration, resulting in a reduction in RhB dye removal. This can be attributed to the scarcity

© University of Pretoria

and low production of free radical species for the reaction due to the blockage of surface-active sites in the photocatalyst.

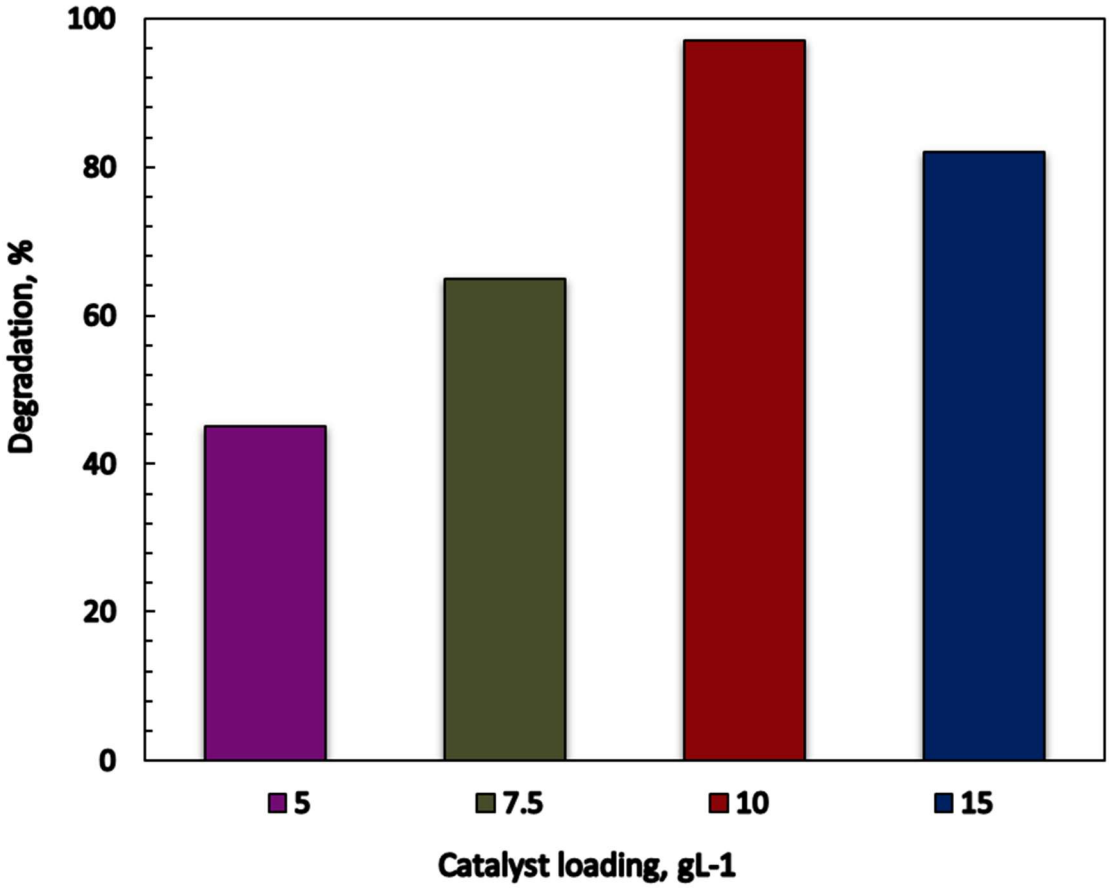

Figure 5.5: Effect of CuS/ZnS catalyst loading in RhB dye degradation.

The rate constants presented in Table 5.1 followed a similar trend to the degradation results depicted in Figure 5.5. The k_{max} values increased five-fold from 0.0034 min^{-1} for 5 g L^{-1} to 0.0186 min^{-1} for 10 g L^{-1}. Increasing the catalyst loading to 15 g L^{-1} decreased the rate constant by half. It is likely that the aforementioned particle agglomeration and shielding effects, which hinder the availability of active sites for reaction, were the cause of this decrease. It is important to note that the Langmuir–Hinshelwood kinetic model best fit the results at a 10 g L^{-1} loading with an R^2 value of 0.99, with loadings of 5 g L^{-1} and 15 g L^{-1} recording R^2 values of ca. 0.90.

© University of Pretoria

Table 5.1: Photodegradation reaction kinetic parameters for varying binary CuS/ZnS nanocomposite catalyst loading in RhB dye degradation.

Catalyst loading (gL^{-1})	Linear regression (R^2)	K_{max} (min^{-1})
0	0.097	0.0000
5	0.897	0.0034
7.5	0.947	0.0058
10	0.986	0.0186
15	0.905	0.0094

5.2.4 Effect of initial rhodamine B concentration

The initial concentration is a significant factor to consider in photocatalytic performance since an increase in concentration will most likely promote competition between the pollutant molecules and the available photogenerated radical species (Sitinjak et al., 2022). In this study, the initial RhB dye concentrations were varied from 5 ppm to 100 ppm while maintaining a 10 g L^{-1} catalyst loading. Figure 5.6 depicts 97 % RhB dye removal at 5 ppm, which drastically declined with increased initial RhB dye concentration, showing 42 %, 27 %, 14 %, 7 %, and 3 % RhB dye photodegradation performance at initial dye solution concentrations of 10 ppm, 30 ppm, 50 ppm, 70 ppm, and 100 ppm. This expected decrease in degradation efficiency with increasing initial RhB dye concentrations is due to increased RhB dye molecules saturating the CuS/ZnS photocatalyst active sites. Increased pollutant concentrations also result in a more darkened colour that restricts electron–hole separation within the catalyst due to light adsorption by the RhB dye solution before reaching the material surface. Furthermore, this can be postulated to reduce the generation of hydroxyl radicals, which ultimately reduces the photodegradation performance (Wang et al., 2014).

The highest RhB dye removal and fastest reaction rate of 0.01299 min^{-1} was achieved at an initial pollutant concentration of 5 ppm. The rate constant values decreased with increased RhB dye concentration, reporting a k_{max} value of 0.0001128 min^{-1} at an initial RhB concentration of 100 ppm.

© University of Pretoria

.

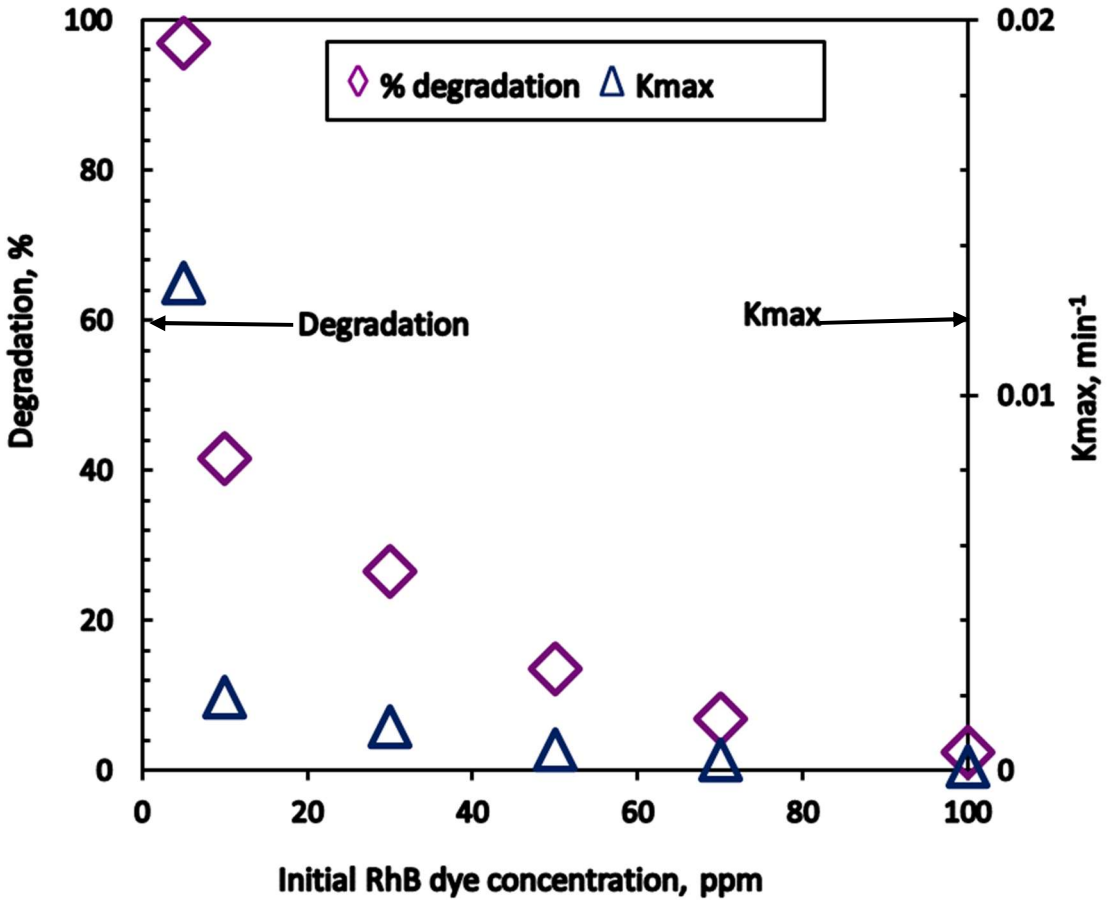

Figure 5.6: Reaction kinetics and effect of catalyst loading in rhodamine B dye degradation with CuS/ZnS photocatalyst.

5.3 Radical scavenging test

Reactive oxygen species (ROS) such as superoxide radicals ($O_2^{\bullet-}$) and hydroxyl radicals (•OH) play a vital role in the photodegradation of organic pollutants as they are regarded as strong, non-selective oxidants (Alshamsi et al., 2021). In order to determine which reactive species was responsible for dye degradation in this study, radical scavenger tests were conducted. The following scavengers were used to target specific reactive species: benzoic acid (e^-), EDTA-2A (h^+), IPA (OH•), and pBZQ ($O_2^{\bullet-}$). These tests were conducted using the optimum conditions: 10 g L^{-1} CuS/ZnS loading, 5 ppm RhB dye concentration, and initial pH

© University of Pretoria

of 5. The results as illustrated in Figure 5.7 revealed that the superoxide radicals ($O_2^{\bullet-}$) were the dominant reactive species as the addition of p-Benzoquinone resulted in a 53 % decrease in dye degradation efficiency. Hydroxyl free radicals and holes (h^+) also played a role in the degradation mechanism. The removal of these species from the aqueous media yielded degradation efficiencies of 59 % and 63 % compared to the 97 % removal observed when no scavenger was added. The presence of electrons did not significantly retard the performance of the catalyst. This was somewhat surprising since the formation of superoxide free radicals ($O_2^{\bullet-}$) occurs through the reaction of the photogenerated electrons with dissolved oxygen. These results were similar to those reported in studies by Mohanty et al. (2022), who credited positively charged holes and superoxide free radical as the dominant reactive species responsible for the degradation of RhB and malachite green (MG) dye when using g-C_3N_4/$Bi_4Ti_3O_{12}$ as a photocatalyst illuminated with visible-light irradiation.

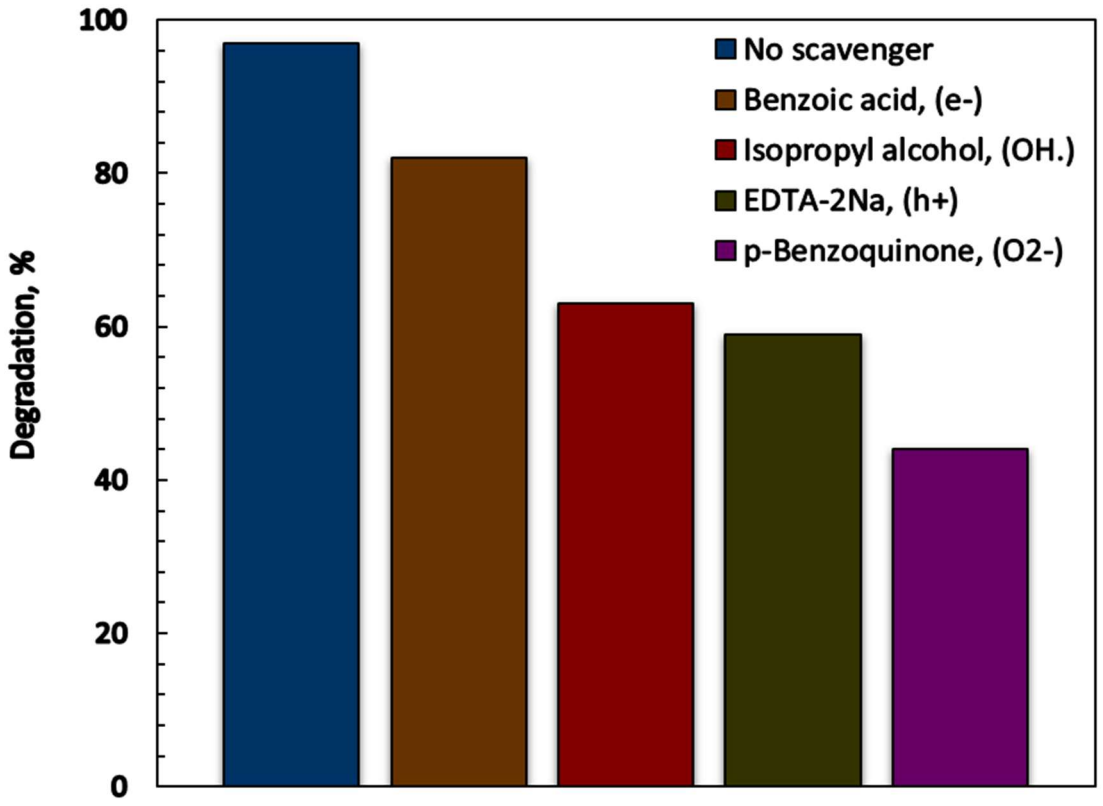

Figure 5.7: Effect of BA, IPA, EDTA – 2Na and pBZQ scavengers rhodamine B dye degradation efficacy using CuS/ZnS photocatalyst.

© University of Pretoria

5.4 Photocatalytic mechanism

CuS has a narrow bandgap energy (1.7 eV), which makes it highly visible-light-photosensitive unlike ZnS (2.5 eV), which has a wide forbidden bandgap energy. The proposed photocatalytic mechanism for the CuS/ZnS heterostructure involves several steps. Firstly, upon irradiation, visible light (hv) excites CuS/ZnS, generating electrons (e^-) and holes (h^+). These electrons and holes are then available to participate in subsequent reactions. The electrons generated in the conduction band of CuS are captured by O_2 to form superoxide anion radicals, contributing to both direct pollutant degradation and indirect RhB removal via reactions with H_2O to generate (•OH) radicals. As shown in Figure 5.8, the flow of electrons from the conduction band (C_B) of ZnS to CuS is impeded because of a mismatch between their respective bandgap energy levels. Consequently, the isolated electrons in ZnS do not participate in the reduction of O_2, as the photodegradation redox potential is determined by the energy levels of the bandgap (Feng et al., 2016, Wang et al., 2018a). Additionally, studies by Hong et al. (2015) suggest that the electrons in the CuS C_B may lead to a partial reduction of CuS to produce CuS/Cu_2S nanoparticles that serve as electron traps to enhance the separation and migration of photogenerated carriers (Hong et al., 2015). The positively charged holes react with water molecules, generating hydrogen ions (H^+) and hydroxyl radicals (•OH) which are powerful oxidants that can react with and degrade organic pollutants. According to the interfacial charge transfer (IFCT) mechanism and the presence of Zn vacancies in both ZnS and at the interface, some of the positively charged holes on the valence band of CuS are transferred to the vacancies of ZnS and the heterojunction. Finally, the hydroxyl radical or superoxide radical anion reacts with the organic pollutant, leading to the formation of oxidised products and water. This reaction represents the degradation of the pollutant and is the ultimate goal of the photocatalytic process.

© University of Pretoria

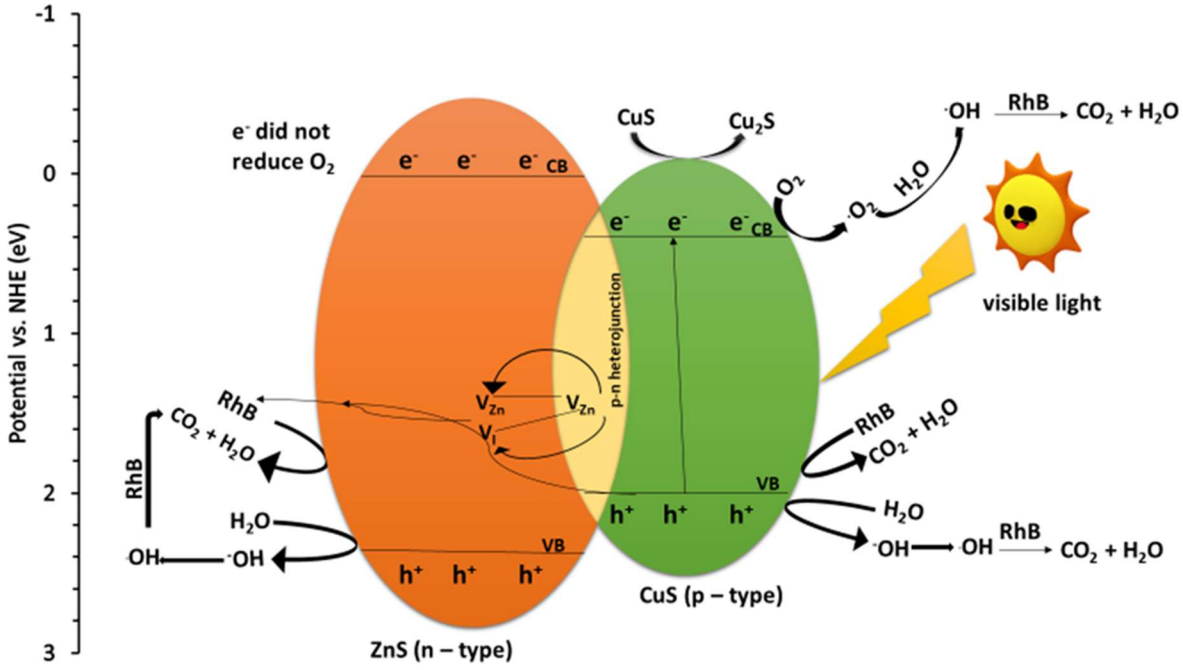

Figure 5.8: Proposed schematic representation of a p-n CuS/ZnS heterojunction photocatalytic mechanism.

This proposed mechanism is similar to the photocatalytic mechanism reported by Feng et al. (2016). The major photocatalytic mechanism steps under visible light irradiation are summarised by the following equations:

$$Excitation: CuS/ZnS + hv \rightarrow CuS/ZnS\ (h^+{}_{VB} + e^-{}_{CB}) \quad (8)$$

$$Recombination: h^+ + e^- \rightarrow energy \quad (9)$$

$$Oxidation: h^+{}_{VB} + H_2O \rightarrow \bullet OH + H^+ \quad (10)$$

$$h^+ + OH^- \rightarrow \bullet OH \quad (11)$$

$$\bullet OH + RhB \rightarrow (intermediates) \rightarrow CO_2 + H_2O \quad (12)$$

$$Reduction: e^-{}_{CB} + O_2 \rightarrow O_2{}^{\bullet -} \quad (13)$$

$$O_2{}^{\bullet -} + H^+ \rightarrow HO_2{}^{\bullet} \quad (14)$$

$$2H_2O + O_2{}^{\bullet -} + e^- \rightarrow \bullet OH + 2OH^- \quad (15)$$

© University of Pretoria

$$\bullet OH/O_2^{\bullet-} + RhB \rightarrow (intermediates) \rightarrow CO_2 + H_2O \quad (16)$$

In conclusion, the presence of IFCT in heteronanostructures has been found to enhance photogenerated charge separation, leading to increased photocatalytic activity. The effective separation of photogenerated electrons and holes is achieved through multistep charge transfer at p-n heterojunctions. Moreover, the suggested mechanism is consistent with the radical forensic test conducted (depicted in Figure 5.7), which indicated that the process of photodegradation was decelerated upon the addition of p-benzoquinone ($O_2^{\bullet-}$ scavenger) and EDTA-2Na (h^+ scavenger). This indicates that the degradation mechanism is primarily driven by superoxide radicals and photogenerated holes.

5.5 Catalyst recyclability

The reusability of photocatalysts is an important factor in determining their cost-effectiveness, as replacements can be quite expensive. To test the stability of the nanocatalyst, five RhB degradation cycles using a recovered catalyst were conducted. After each cycle, the catalyst particles were recovered by centrifugation and then washed with deionised water, ethanol, and deionised water three times prior to thermal reactivation. The catalyst was then oven-dried at 50 °C for 12 h and ground to a powder before reuse. The results depicted in Figure 5.9 show that the CuS/ZnS nanocatalyst exhibited a high level of photostability, with no significant decrease in photodegradation efficiency after five cycles. Following each cycle, the catalytic activity slightly decreased, resulting in a 14 % activity reduction (from 97 % in cycle 1 to 83 % in cycle 5). It can be concluded that the CuS/ZnS nanomaterial did not lose its degradation properties but demonstrated excellent chemical stability, recyclability utilisation, and sustainability.

© University of Pretoria

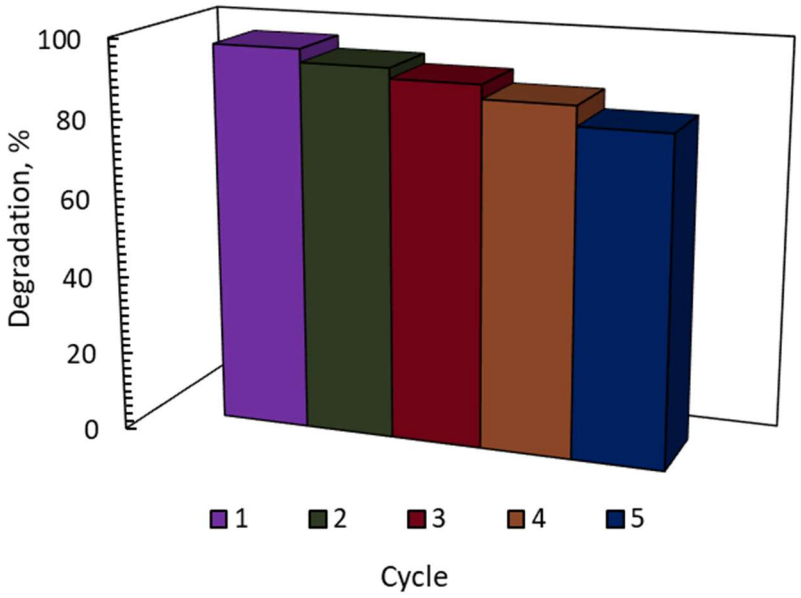

Figure 5.9: Stability and recyclability of CuS/ZnS photocatalyst during 5 cycles.

Figure 5.10 shows scanning electron microscope (SEM) images of the CuS/ZnS photocatalyst before and after five cycles of reuse in the photodegradation of the rhodamine B pollutant. The images reveal that the surface of the hollow porous material, with a varied pore size distribution, remained consistent before and after reuse. However, the morphology of the material changed during recycling from clustered agglomerates to a mixture of morphologies, including flower-like particles, nanosheets, and nanoplates. This suggests that the photoactivity of the catalyst used in this study was not greatly influenced by the particle morphology.

© University of Pretoria

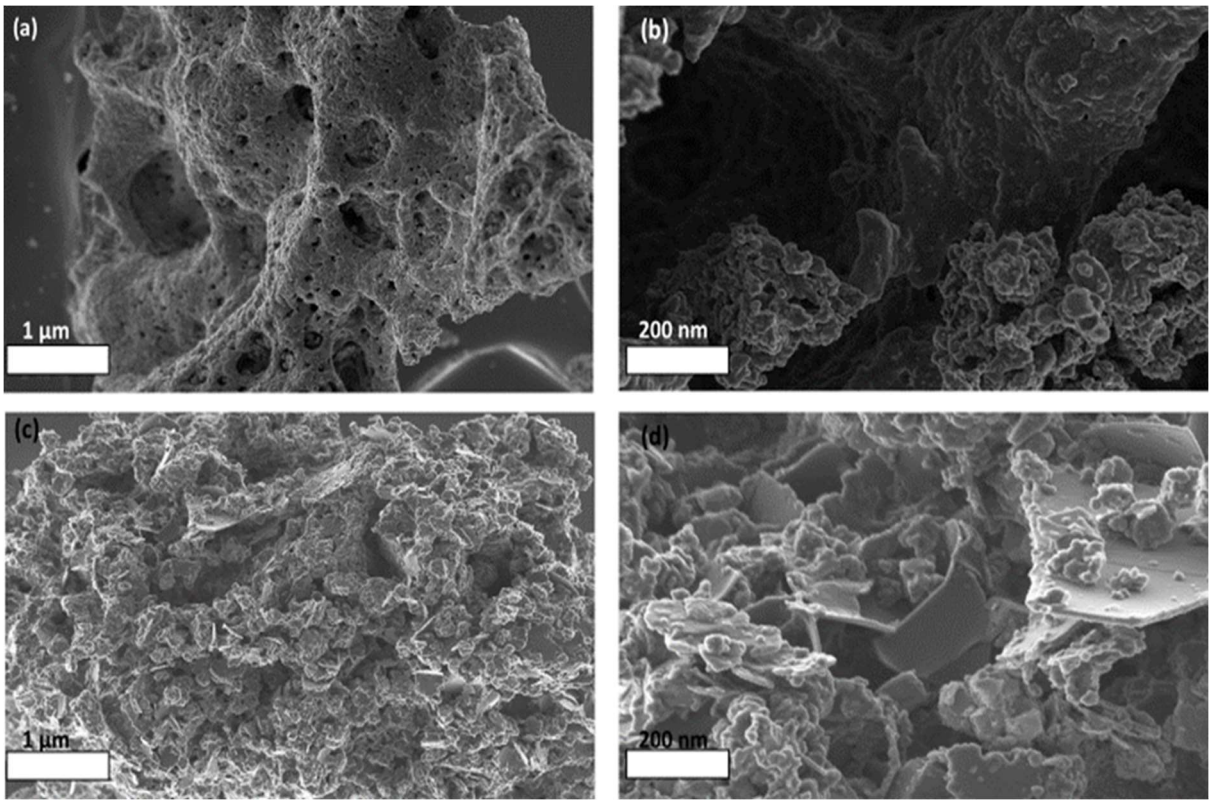

Figure 5.10: (a) Zoomed-out and (b) zoomed-in CuS/ZnS SEM images before use and (c) zoomed-out and (d) zoomed-in CuS/ZnS SEM images after 5 recycles.

© University of Pretoria

CHAPTER 6: CONCLUSIONS AND RECOMMENDATIONS

This study presents a novel and facile one-pot thermal decomposition method for synthesizing CuS, ZnS, and hybrid CuS/ZnS p-n heterojunctions with porous morphologies, which significantly improved their photodegradation efficacy by reducing the rate of charge carrier transfer. The binary CuS/ZnS heterojunction demonstrated exceptional RhB dye photodegradation under visible-light irradiation due to its ability to absorb visible light and the inhibition of the photoinduced e^-/h^+ recombination rate. Photodegradation scavenger tests revealed the superoxide radicals to be the primary reactive species responsible for the efficient degradation of RhB dye. Additionally, recycling investigations proved the CuS/ZnS photocatalysts' outstanding durability and excellent chemical stability after five cycles of use. The results of this study highlight the promising potential of the novel synthesis method and resulting CuS/ZnS heterojunction for cost-effective and efficient industrial treatments using photocatalysis. This process can be further optimised by varying other extrinsic factors that may likely affect the degradation efficiency such as the degree of mineralisation achieved by the catalyst and potential for use in a continuous reactor setup. Further studies may explore the applicability of this method to other photocatalytic systems and applications.

© University of Pretoria

REFERENCES

ABDELWAHAB, M. A., EL RAYES, S., KAMEL, M. M. & ABDELRAHMAN, E. A. 2022. Encapsulation of NiS and ZnS in analcime nanoparticles as novel nanocomposites for the effective photocatalytic degradation of orange G and methylene blue dyes. *International Journal of Environmental Analytical Chemistry*, 1-18.

ABUBSHAIT, S. A., IQBAL, S., ABUBSHAIT, H. A., ALOBAID, A. A., AL-MUHIMEED, T. I., ABD-RABBOH, H. S., BAHADUR, A. & LI, W. 2021. Effective heterointerface combination of 1D/2D Co-NiS/Sg-C3N4 heterojunction for boosting spatial charge separation with enhanced photocatalytic degradation of organic pollutants and disinfection of pathogens. *Colloids and Surfaces A: Physicochemical and Engineering Aspects,* 628**,** 127390.

ADELIFARD, M., ESHGHI, H. & MOHAGHEGHI, M. M. B. 2012. Synthesis and characterization of nanostructural CuS–ZnS binary compound thin films prepared by spray pyrolysis. *Optics Communications,* 285**,** 4400-4404.

ADHIKARI, S. P. 2017. *Visible-Light-Active Semiconductor Heterojunctions for Enhanced Photocatalytic Activity*, Wake Forest University.

AHMAD, F., ZHU, D. & SUN, J. 2021. Environmental fate of tetracycline antibiotics: degradation pathway mechanisms, challenges, and perspectives. *Environmental Sciences Europe,* 33**,** 1-17.

AJIBOYE, T. O., OYEWO, O. A. & ONWUDIWE, D. C. 2021. Adsorption and photocatalytic removal of Rhodamine B from wastewater using carbon-based materials. *FlatChem,* 29**,** 100277.

AL-BURIAHI, A. K., AL-GHEETHI, A. A., KUMAR, P. S., MOHAMED, R. M. S. R., YUSOF, H., ALSHALIF, A. F. & KHALIFA, N. A. 2022. Elimination of rhodamine B from textile wastewater using nanoparticle photocatalysts: a review for sustainable approaches. *Chemosphere,* 287**,** 132162.

AL-GHEETHI, A. A., AZHAR, Q. M., KUMAR, P. S., YUSUF, A. A., AL-BURIAHI, A. K., MOHAMED, R. M. S. R. & AL-SHAIBANI, M. M. 2022. Sustainable approaches for removing Rhodamine B dye using agricultural waste adsorbents: A review. *Chemosphere,* 287**,** 132080.

AL-MAMUN, M., KADER, S., ISLAM, M. & KHAN, M. 2019. Photocatalytic activity improvement and application of UV-TiO2 photocatalysis in textile wastewater treatment: A review. *Journal of Environmental Chemical Engineering,* 7**,** 103248.

AL-RUBAIEY, N. A. 2022. A trends in Ozone Treatment of Wastewater: a Review. *Iraqi Journal of Oil and Gas Research (IJOGR),* 2**,** 55-64.

ALHADDAD, M. & SHAWKY, A. 2020. CuS assembled rGO heterojunctions for superior photooxidation of atrazine under visible light. *Journal of molecular liquids,* 318**,** 114377.

ALSHAMSI, H. A., BESHKAR, F., AMIRI, O. & SALAVATI-NIASARI, M. 2021. Porous hollow Ag/Ag2S/Ag3PO4 nanocomposites as highly efficient heterojunction photocatalysts for the removal of antibiotics under simulated sunlight irradiation. *Chemosphere,* 274**,** 129765.

AMATERZ, E., TARA, A., BOUDDOUCH, A., TAOUFYQ, A., BAKIZ, B., BENLHACHEMI, A. & JBARA, O. 2020. Photo-electrochemical degradation of

© University of Pretoria

wastewaters containing organics catalysed by phosphate-based materials: a review. *Reviews in Environmental Science and Bio/Technology,* 19**,** 843-872.

ANJUM, M., KUMAR, R. & BARAKAT, M. 2017. Visible light driven photocatalytic degradation of organic pollutants in wastewater and real sludge using ZnO–ZnS/Ag2O–Ag2S nanocomposite. *Journal of the Taiwan Institute of Chemical Engineers,* 77**,** 227-235.

ARJUNAN, S., KAVITHA, H. P., PONNUSAMY, S., MANI, N. & HAYAKAWA, Y. 2016. ZnS/CuS nanocomposites: an effective strategy to transform UV active ZnS to UV and Vis light active ZnS. *Journal of Materials Science: Materials in Electronics,* 27**,** 9022-9033.

AYODHYA, D. & VEERABHADRAM, G. 2018. A review on recent advances in photodegradation of dyes using doped and heterojunction based semiconductor metal sulfide nanostructures for environmental protection. *Materials today energy,* 9**,** 83-113.

BABUPONNUSAMI, A. & MUTHUKUMAR, K. 2014. A review on Fenton and improvements to the Fenton process for wastewater treatment. *Journal of Environmental Chemical Engineering,* 2**,** 557-572.

BUMAJDAD, A. & MADKOUR, M. 2014. Understanding the superior photocatalytic activity of noble metals modified titania under UV and visible light irradiation. *Physical Chemistry Chemical Physics,* 16**,** 7146-7158.

BYRAPPA, K., SUBRAMANI, A., ANANDA, S., RAI, K. L., DINESH, R. & YOSHIMURA, D. M. 2006. Photocatalytic degradation of rhodamine B dye using hydrothermally synthesized ZnO. *Bulletin of materials science,* 29**,** 433-438.

CARMEN, Z. & DANIELA, S. 2012. *Textile organic dyes-characteristics, polluting effects and separation/elimination procedures from industrial effluents-a critical overview*, IntechOpen Rijeka.

CASHMAN, M. A., KIRSCHENBAUM, L., HOLOWACHUK, J. & BOVING, T. B. 2019. Identification of hydroxyl and sulfate free radicals involved in the reaction of 1, 4-dioxane with peroxone activated persulfate oxidant. *Journal of hazardous materials,* 380**,** 120875.

CHALA, T. F., WU, C.-M. & MOTORA, K. G. 2019. RbxWO3/Ag3VO4 nanocomposites as efficient full-spectrum (UV, visible, and near-infrared) photocatalysis. *Journal of the Taiwan Institute of Chemical Engineers,* 102**,** 465-474.

CHEN, X. & MAO, S. S. 2007. Titanium dioxide nanomaterials: synthesis, properties, modifications, and applications. *Chemical reviews,* 107**,** 2891-2959.

CHONG, M., JIN, B., CHOW, C. & SAINT, C. 2010. New developments in photocatalytic water treatment technology: a review. *Water Res,* 44**,** 2997-3027.

COLLIVIGNARELLI, M. C., PEDRAZZANI, R., SORLINI, S., ABBÀ, A. & BERTANZA, G. 2017. H2O2 based oxidation processes for the treatment of real high strength aqueous wastes. *Sustainability,* 9**,** 244.

CRINI, G. & LICHTFOUSE, E. 2019. Advantages and disadvantages of techniques used for wastewater treatment. *Environmental Chemistry Letters,* 17**,** 145-155.

DAS, P., TANTUBAY, K., GHOSH, R., DAM, S. & BASKEY, M. 2021. Transformation of CuS/ZnS nanomaterials to an efficient visible light photocatalyst by ‘photosensitizer’graphene and the potential antimicrobial activities of the nanocomposites. *Environmental Science and Pollution Research,* 28**,** 49125-49138.

© University of Pretoria

DENG, Y., ZHANG, Z., DU, P., NING, X., WANG, Y., ZHANG, D., LIU, J., ZHANG, S. & LU, X. 2020. Embedding ultrasmall Au clusters into the pores of a covalent organic framework for enhanced photostability and photocatalytic performance. *Angewandte Chemie,* 132**,** 6138-6145.

EL-HOUT, S. I., EL-SHEIKH, S. M., GABER, A., SHAWKY, A. & AHMED, A. I. 2020. Highly efficient sunlight-driven photocatalytic degradation of malachite green dye over reduced graphene oxide-supported CuS nanoparticles. *Journal of Alloys and Compounds,* 849**,** 156573.

FARD, Z. M., BAGHERI, M., RABIEH, S. & MOUSAVI, H. Z. 2020. Efficient visible light-driven core–shell-structured ZnS@ Ag2S nanoparticles-anchored reduced graphene oxide for the reduction of Cr (VI). *New Journal of Chemistry,* 44**,** 14670-14678.

FENG, C., MENG, X., SONG, X., FENG, X., ZHAO, Y. & LIU, G. 2016. Controllable synthesis of hierarchical CuS/ZnS hetero-nanowires as high-performance visible-light photocatalysts. *RSC advances,* 6**,** 110266-110273.

FUJISHIMA, A. 2000. TN RAO and DA TRYK. *J. Photochem. Photobiol. C: Photochem. Rev,* 1**,** 1.

GEDDA, G., BALAKRISHNAN, K., DEVI, R. U., SHAH, K. J., GANDHI, V., GANDH, V. & SHAH, K. 2021. Introduction to conventional wastewater treatment technologies: limitations and recent advances. *Mater. Res. Found,* 91**,** 1-36.

GRABOWSKA, E. 2016. Selected perovskite oxides: Characterization, preparation and photocatalytic properties—A review. *Applied Catalysis B: Environmental,* 186**,** 97-126.

GUO, J., LIANG, Y., LIU, L., HU, J., WANG, H., AN, W. & CUI, W. 2021. Core-shell structure of sulphur vacancies-CdS@ CuS: Enhanced photocatalytic hydrogen generation activity based on photoinduced interfacial charge transfer. *Journal of Colloid and Interface Science,* 600**,** 138-149.

GUO, Y., LI, C., GONG, Z., GUO, Y., WANG, X., GAO, B., QIN, W. & WANG, G. 2020. Photocatalytic decontamination of tetracycline and Cr (VI) by a novel α-FeOOH/FeS2 photocatalyst: one-pot hydrothermal synthesis and Z-scheme reaction mechanism insight. *Journal of hazardous materials,* 397**,** 122580.

GUO, Y., LI, J., GAO, Z., ZHU, X., LIU, Y., WEI, Z., ZHAO, W. & SUN, C. 2016. A simple and effective method for fabricating novel p–n heterojunction photocatalyst g-C3N4/Bi4Ti3O12 and its photocatalytic performances. *Applied Catalysis B: Environmental,* 192**,** 57-71.

HANAFI, M. F. & SAPAWE, N. 2020. A review on the water problem associate with organic pollutants derived from phenol, methyl orange, and remazol brilliant blue dyes. *Materials Today: Proceedings,* 31**,** A141-A150.

HARISH, S., ARCHANA, J., NAVANEETHAN, M., PONNUSAMY, S., SINGH, A., GUPTA, V., ASWAL, D., IKEDA, H. & HAYAKAWA, Y. 2017. Synergetic effect of CuS@ ZnS nanostructures on photocatalytic degradation of organic pollutant under visible light irradiation. *RSC advances,* 7**,** 34366-34375.

HEIDARI, G., RABANI, M. & RAMEZANZADEH, B. 2017. Application of CuS–ZnS PN junction for photoelectrochemical water splitting. *International Journal of Hydrogen Energy,* 42**,** 9545-9552.

HONG, Y., ZHANG, J., HUANG, F., ZHANG, J., WANG, X., WU, Z., LIN, Z. & YU, J. 2015. Enhanced visible light photocatalytic hydrogen production activity of CuS/ZnS nanoflower spheres. *Journal of Materials Chemistry A,* 3**,** 13913-13919.

© University of Pretoria

HU, C.-C., NIAN, J.-N. & TENG, H. 2008. Electrodeposited p-type Cu2O as photocatalyst for H2 evolution from water reduction in the presence of WO3. *Solar energy materials and solar cells,* 92**,** 1071-1076.

HUANG, C., HU, J., CONG, S., ZHAO, Z. & QIU, X. 2015. Hierarchical BiOCl microflowers with improved visible-light-driven photocatalytic activity by Fe (III) modification. *Applied Catalysis B: Environmental,* 174**,** 105-112.

ICHIPI, E. O., TICHAPONDWA, S. M. & CHIRWA, E. M. 2022. Plasmonic effect and bandgap tailoring of Ag/Ag2S doped on ZnO nanocomposites for enhanced visible-light photocatalysis. *Advanced Powder Technology,* 33**,** 103596.

ISAC, L., CAZAN, C., ENESCA, A. & ANDRONIC, L. 2019. Copper sulfide based heterojunctions as photocatalysts for dyes photodegradation. *Frontiers in chemistry,* 7**,** 694.

ISAC, L. & ENESCA, A. 2022. Recent Developments in ZnS-Based Nanostructures Photocatalysts for Wastewater Treatment. *International journal of molecular sciences,* 23**,** 15668.

JAIN, R., MATHUR, M., SIKARWAR, S. & MITTAL, A. 2007. Removal of the hazardous dye rhodamine B through photocatalytic and adsorption treatments. *Journal of environmental management,* 85**,** 956-964.

JIA, Y., YANG, J., ZHAO, D., HAN, H. & LI, C. 2014. A Novel Sr2CuInO3S p-type semiconductor photocatalyst for hydrogen production under visible light irradiation. *Journal of energy chemistry,* 23**,** 420-426.

KANAKARAJU, D. & CHANDRASEKARAN, A. 2023. Recent advances in TiO2/ZnS-based binary and ternary photocatalysts for the degradation of organic pollutants. *Science of The Total Environment,* 868**,** 161525.

KARTHIKEYAN, C., ARUNACHALAM, P., RAMACHANDRAN, K., AL-MAYOUF, A. M. & KARUPPUCHAMY, S. 2020. Recent advances in semiconductor metal oxides with enhanced methods for solar photocatalytic applications. *Journal of Alloys and Compounds,* 828**,** 154281.

KHAN, A. U., AROOJ, A., TAHIR, K., IBRAHIM, M. M., JEVTOVIC, V., AL-ABDULKARIM, H. A., SALEH, E. A. M., AL-SHEHRI, H. S., AMIN, M. A. & LI, B. 2022. Facile fabrication of novel Ag2S-ZnO/GO nanocomposite with its enhanced photocatalytic and biological applications. *Journal of Molecular Structure,* 1251**,** 131991.

KHAVAR, A. H. C., MOUSSAVI, G., MAHJOUB, A. R., LUQUE, R., RODRÍGUEZ-PADRÓN, D. & SATTARI, M. 2019. Enhanced visible light photocatalytic degradation of acetaminophen with Ag2S-ZnO@ rGO core-shell microsphere as a novel catalyst: Catalyst preparation and characterization and mechanistic catalytic experiments. *Separation and Purification Technology,* 229**,** 115803.

KISHOR, R., PURCHASE, D., SARATALE, G. D., SARATALE, R. G., FERREIRA, L. F. R., BILAL, M., CHANDRA, R. & BHARAGAVA, R. N. 2021. Ecotoxicological and health concerns of persistent coloring pollutants of textile industry wastewater and treatment approaches for environmental safety. *Journal of Environmental Chemical Engineering,* 9**,** 105012.

KOE, W. S., LEE, J. W., CHONG, W. C., PANG, Y. L. & SIM, L. C. 2020. An overview of photocatalytic degradation: photocatalysts, mechanisms, and development of photocatalytic membrane. *Environmental Science and Pollution Research,* 27**,** 2522-2565.

KUO, C.-H., YANG, Y.-C., GWO, S. & HUANG, M. H. 2011. Facet-dependent and Au nanocrystal-enhanced electrical and photocatalytic properties of Au− Cu2O

© University of Pretoria

core− shell heterostructures. *Journal of the American Chemical Society,* 133**,** 1052-1057.

KWOLEK, P. & SZACIŁOWSKI, K. 2013. Photoelectrochemistry of n-type bismuth oxyiodide. *Electrochimica Acta,* 104**,** 448-453.

LE, S., LI, W., WANG, Y., JIANG, X., YANG, X. & WANG, X. 2019. Carbon dots sensitized 2D-2D heterojunction of BiVO4/Bi3TaO7 for visible light photocatalytic removal towards the broad-spectrum antibiotics. *Journal of hazardous materials,* 376**,** 1-11.

LEE, G.-J. & WU, J. J. 2017. Recent developments in ZnS photocatalysts from synthesis to photocatalytic applications—A review. *Powder technology,* 318**,** 8-22.

LESCHKIES, K., DIVAKAR, R. & BASU, J. 2007. EE–Pommer, JE Boercker, CB Carter, UR Kortshagen, DJ Norris, ES Aydil. *Nano Lett,* 7**,** 1793.

LI, G., DENG, X., CHEN, P., WANG, X., MA, J., LIU, F. & YIN, S.-F. 2022. Sulphur vacancies-VS2@ C3N4 drived by in situ supramolecular self-assembly for synergistic photocatalytic degradation of real wastewater and H2 production: Vacancies taming interfacial compact heterojunction and carriers transfer. *Chemical Engineering Journal,* 433**,** 134505.

LI, X., HUANG, R., HU, Y., CHEN, Y., LIU, W., YUAN, R. & LI, Z. 2012. A templated method to Bi2WO6 hollow microspheres and their conversion to double-shell Bi2O3/Bi2WO6 hollow microspheres with improved photocatalytic performance. *Inorganic Chemistry,* 51**,** 6245-6250.

LI, Y., CHEN, S., ZHANG, K., GU, S., CAO, J., XIA, Y., YANG, C., SUN, W. & ZHOU, Z. 2020. Highly efficient and stable photocatalytic properties of CdS/FeS nanocomposites. *New Journal of Chemistry,* 44**,** 14695-14702.

LIN, H.-F., LIAO, S.-C. & HUNG, S.-W. 2005. The dc thermal plasma synthesis of ZnO nanoparticles for visible-light photocatalyst. *Journal of photochemistry and photobiology A: Chemistry,* 174**,** 82-87.

LIU, X., ZHANG, Y., JIA, Y., JIANG, J., WANG, Y., CHEN, X. & GUI, T. 2017. Visible light-responsive carbon-decorated p-type semiconductor CaFe2O4 nanorod photocatalyst for efficient remediation of organic pollutants. *Chinese Journal of Catalysis,* 38**,** 1770-1779.

LOW, J., YU, J., JARONIEC, M., WAGEH, S. & AL-GHAMDI, A. A. 2017. Heterojunction photocatalysts. *Advanced materials,* 29**,** 1601694.

MAHAMUNI, N. N. & ADEWUYI, Y. G. 2010. Advanced oxidation processes (AOPs) involving ultrasound for waste water treatment: a review with emphasis on cost estimation. *Ultrasonics sonochemistry,* 17**,** 990-1003.

MALEFANE, M. E., NTSENDWANA, B., MAFA, P. J., MABUBA, N., FELENI, U. & KUVAREGA, A. T. 2019. In-situ synthesis of Tetraphenylporphyrin/Tungsten (VI) Oxide/Reduced Graphene Oxide (TPP/WO3/RGO) nanocomposite for visible light photocatalytic degradation of Acid Blue 25. *ChemistrySelect,* 4**,** 8379-8389.

MATAVOS-ARAMYAN, S. & MOUSSAVI, M. 2017. Advances in Fenton and Fenton based oxidation processes for industrial effluent contaminants control-a review. *Int. J. Environ. Sci. Nat. Resour,* 2**,** 1-18.

MIYAUCHI, M., NUKUI, Y., ATARASHI, D. & SAKAI, E. 2013. Selective growth of n-type nanoparticles on p-type semiconductors for Z-scheme photocatalysis. *ACS applied materials & interfaces,* 5**,** 9770-9776.

© University of Pretoria

MOHAJERANI, M., MEHRVAR, M. & EIN-MOZAFFARI, F. 2009. An overview of the integration of advanced oxidation technologies and other processes for water and wastewater treatment. *International Journal of Engineering,* 3**,** 120-146.

MOHAMMED, N., PALANIANDY, P. & SHAIK, F. 2021. Pollutants removal from saline water by solar photocatalysis: a review of experimental and theoretical approaches. *International Journal of Environmental Analytical Chemistry***,** 1-21.

MOHANTY, L., PATTANAYAK, D. S., PRADHAN, D. & DASH, S. K. 2022. Synthesis of novel p-n heterojunction g-C3N4/Bi4Ti3O12 photocatalyst with improved solar-light-driven photocatalytic degradation of organic dyes. *Environmental Quality Management*.

MOJA, M. M., CHIRWA, E. & TICHAPONDWA, S. M. 2021. Visible light activated photocatalytic degradation of 2, 4-dichlorophenol using silver halide photocatalysts.

MONDAL, C., SINGH, A., SAHOO, R., SASMAL, A. K., NEGISHI, Y. & PAL, T. 2015. Preformed ZnS nanoflower prompted evolution of CuS/ZnS p-n heterojunctions for exceptional visible-light driven photocatalytic activity. *New Journal of Chemistry,* 39**,** 5628-5635.

MUGUMO, R., TICHAPONDWA, S. M. & CHIRWA, E. M. 2022. Photocatalytic Degradation of Rhodamine B Using CuS-doped ZnS Under Visible Light Irradiation. *Chemical Engineering Transactions,* 94**,** 1447-1452.

MZIMELA, N., TICHAPONDWA, S. & CHIRWA, E. 2022. Visible-light-activated photocatalytic degradation of rhodamine B using WO 3 nanoparticles. *RSC advances,* 12**,** 34652-34659.

NACIRI, Y., AHSAINE, H. A., CHENNAH, A., AMEDLOUS, A., TAOUFYQ, A., BAKIZ, B., EZAHRI, M., VILLAIN, S. & BENLHACHEMI, A. 2018. Facile synthesis, characterization and photocatalytic performance of Zn3 (PO4) 2 platelets toward photodegradation of Rhodamine B dye. *Journal of Environmental Chemical Engineering,* 6**,** 1840-1847.

NATARAJAN, S., BAJAJ, H. C. & TAYADE, R. J. 2018. Recent advances based on the synergetic effect of adsorption for removal of dyes from waste water using photocatalytic process. *Journal of Environmental Sciences,* 65**,** 201-222.

PANDEY, S. K., MISHRA, P. K. & TIWARY, D. 2022. Enhanced photocatalytic performance of NiS/ZnO nanocomposite for the remediation of PNP and RhB dye. *Journal of Environmental Chemical Engineering,* 10**,** 107459.

PAŹDZIOR, K., BILIŃSKA, L. & LEDAKOWICZ, S. 2019. A review of the existing and emerging technologies in the combination of AOPs and biological processes in industrial textile wastewater treatment. *Chemical Engineering Journal,* 376**,** 120597.

RAFIQ, A., IKRAM, M., ALI, S., NIAZ, F., KHAN, M., KHAN, Q. & MAQBOOL, M. 2021. Photocatalytic degradation of dyes using semiconductor photocatalysts to clean industrial water pollution. *Journal of Industrial and Engineering Chemistry,* 97**,** 111-128.

RAMESHBABU, R., RAVI, P. & SATHISH, M. 2019. Cauliflower-like CuS/ZnS nanocomposites decorated g-C3N4 nanosheets as noble metal-free photocatalyst for superior photocatalytic water splitting. *Chemical Engineering Journal,* 360**,** 1277-1286.

REINECK, P., LEE, G. P., BRICK, D., KARG, M., MULVANEY, P. & BACH, U. 2012. A solid-state plasmonic solar cell via metal nanoparticle self-assembly. *Advanced Materials,* 24**,** 4750-4755.

© University of Pretoria

REISS, P., PROTIERE, M. & LI, L. 2009. Core/shell semiconductor nanocrystals. *small,* 5**,** 154-168.

ROBLES-MOLINA, J., GILBERT-LÓPEZ, B., GARCÍA-REYES, J. F. & MOLINA-DÍAZ, A. 2014. Monitoring of selected priority and emerging contaminants in the Guadalquivir River and other related surface waters in the province of Jaén, South East Spain. *Science of the Total Environment,* 479**,** 247-257.

SAADATI, F., KERAMATI, N. & GHAZI, M. M. 2016. Influence of parameters on the photocatalytic degradation of tetracycline in wastewater: a review. *Critical reviews in environmental science and technology,* 46**,** 757-782.

SAIGL, Z. M. 2021. Various adsorbents for removal of rhodamine b dye: A review. *Indonesian Journal of Chemistry,* 21**,** 1039-1056.

SAMUEL, M. S., SAVUNTHARI, K. V. & ETHIRAJ, S. 2021. Synthesis of a copper (II) metal–organic framework for photocatalytic degradation of rhodamine B dye in water. *Environmental Science and Pollution Research,* 28**,** 40835-40843.

SARAVANAN, A., KUMAR, P. S., JEEVANANTHAM, S., KARISHMA, S., TAJSABREEN, B., YAASHIKAA, P. & RESHMA, B. 2021. Effective water/wastewater treatment methodologies for toxic pollutants removal: Processes and applications towards sustainable development. *Chemosphere,* 280**,** 130595.

SHARIFZADE, G., ASGHARI, A. & RAJABI, M. 2017. Highly effective adsorption of xanthene dyes (rhodamine B and erythrosine B) from aqueous solutions onto lemon citrus peel active carbon: characterization, resolving analysis, optimization and mechanistic studies. *RSC advances,* 7**,** 5362-5371.

SHARMA, K., RAIZADA, P., HASIJA, V., SINGH, P., BAJPAI, A., NGUYEN, V.-H., RANGABHASHIYAM, S., KUMAR, P., NADDA, A. K. & KIM, S. Y. 2021. ZnS-based quantum dots as photocatalysts for water purification. *Journal of Water Process Engineering,* 43**,** 102217.

SHI, L., LI, P., ZHOU, W., WANG, T., CHANG, K., ZHANG, H., KAKO, T., LIU, G. & YE, J. 2016. n-Type boron phosphide as a highly stable, metal-free, visible-light-active photocatalyst for hydrogen evolution. *Nano Energy,* 28**,** 158-163.

SIRÉS, I., BRILLAS, E., OTURAN, M. A., RODRIGO, M. A. & PANIZZA, M. 2014. Electrochemical advanced oxidation processes: today and tomorrow. A review. *Environmental Science and Pollution Research,* 21**,** 8336-8367.

SITINJAK, E. M., MASMUR, I., MARBUN, N. V. M. D., HUTAJULU, P. E., GULTOM, G. & SITANGGANG, Y. 2022. Direct Z-scheme of n-type CuS/p-type ZnS@ electrospun PVP nanofiber for the highly efficient catalytic reduction of 4-nitrophenol and mixed dyes. *RSC advances,* 12**,** 16165-16173.

SREELEKHA, N., SUBRAMANYAM, K., REDDY, D. A., MURALI, G., RAMU, S., VARMA, K. R. & VIJAYALAKSHMI, R. 2016. Structural, optical, magnetic and photocatalytic properties of Co doped CuS diluted magnetic semiconductor nanoparticles. *Applied Surface Science,* 378**,** 330-340.

THUY, U. T. D., LIEM, N. Q., PARLETT, C. M., LALEV, G. M. & WILSON, K. 2014. Synthesis of CuS and CuS/ZnS core/shell nanocrystals for photocatalytic degradation of dyes under visible light. *Catalysis Communications,* 44**,** 62-67.

TICHAPONDWA, S. M., NEWMAN, J. & KUBHEKA, O. 2020. Effect of TiO2 phase on the photocatalytic degradation of methylene blue dye. *Physics and Chemistry of the Earth, Parts A/B/C,* 118**,** 102900.

UDDIN, M. T. 2013. *Metal oxide heterostructures for efficient photocatalysts.* Université Sciences et Technologies-Bordeaux I; Technische Universität ….

© University of Pretoria

VARGHESE, J. 2021. CuS–ZnS decorated graphene nanocomposites: Synthesis and photocatalytic properties. *Journal of Physics and Chemistry of Solids,* 156**,** 109911.

VENUGOPAL, G., THANGAVEL, S., VASUDEVAN, V. & ZOLTÁN, K. 2020. Efficient visible-light piezophototronic activity of ZnO-Ag8S hybrid for degradation of organic dye molecule. *Journal of Physics and Chemistry of Solids,* 143**,** 109473.

WANG, C., LI, J., MELE, G., YANG, G.-M., ZHANG, F.-X., PALMISANO, L. & VASAPOLLO, G. 2007. Efficient degradation of 4-nitrophenol by using functionalized porphyrin-TiO2 photocatalysts under visible irradiation. *Applied Catalysis B: Environmental,* 76**,** 218-226.

WANG, H., ZHANG, L., CHEN, Z., HU, J., LI, S., WANG, Z., LIU, J. & WANG, X. 2014. Semiconductor heterojunction photocatalysts: design, construction, and photocatalytic performances. *Chemical Society Reviews,* 43**,** 5234-5244.

WANG, J., SONG, Y., HU, J., LI, Y., WANG, Z., YANG, P., WANG, G., MA, Q., CHE, Q. & DAI, Y. 2019. Photocatalytic hydrogen evolution on P-type tetragonal zircon BiVO4. *Applied Catalysis B: Environmental,* 251**,** 94-101.

WANG, J., TANG, L., ZENG, G., DENG, Y., LIU, Y., WANG, L., ZHOU, Y., GUO, Z., WANG, J. & ZHANG, C. 2017a. Atomic scale g-C3N4/Bi2WO6 2D/2D heterojunction with enhanced photocatalytic degradation of ibuprofen under visible light irradiation. *Applied Catalysis B: Environmental,* 209**,** 285-294.

WANG, L., ZHAO, J., LIU, H. & HUANG, J. 2018a. Design, modification and application of semiconductor photocatalysts. *Journal of the Taiwan Institute of Chemical Engineers,* 93**,** 590-602.

WANG, R., LU, K.-Q., TANG, Z.-R. & XU, Y.-J. 2017b. Recent progress in carbon quantum dots: synthesis, properties and applications in photocatalysis. *Journal of Materials Chemistry A,* 5**,** 3717-3734.

WANG, Y., JIANG, F., CHEN, J., SUN, X., XIAN, T. & YANG, H. 2020. In situ construction of CNT/CuS hybrids and their application in photodegradation for removing organic dyes. *Nanomaterials,* 10**,** 178.

WANG, Y., SUZUKI, H. & XIE, J. 2018b. O, Tomita, DJ Martin, M. Higashi, D. Kong, R. Abe, and J. Tang. *Chem. Rev,* 118**,** 5201-5241.

WU, S., SHEN, X., ZHU, G., ZHOU, H., JI, Z., CHEN, K. & YUAN, A. 2016. Synthesis of ternary Ag/ZnO/ZnFe2O4 porous and hollow nanostructures with enhanced photocatalytic activity. *Applied Catalysis B: Environmental,* 184**,** 328-336.

WU, Z., LIU, X., YU, C., LI, F., ZHOU, W. & WEI, L. 2021. Construct interesting CuS/TiO2 architectures for effective removal of Cr (VI) in simulated wastewater via the strong synergistic adsorption and photocatalytic process. *Science of The Total Environment,* 796**,** 148941.

XIAO, Q., YU, S., LI, L., ZHANG, Y. & YI, P. 2019. Degradation of bromate by Fe (II) Ti (IV) layered double hydroxides nanoparticles under ultraviolet light. *Water research,* 150**,** 310-320.

XU, D. & MA, H. 2021. Degradation of rhodamine B in water by ultrasound-assisted TiO2 photocatalysis. *Journal of Cleaner Production,* 313**,** 127758.

XU, Q., ZHANG, L., CHENG, B., FAN, J. & YU, J. 2020. S-scheme heterojunction photocatalyst. *Chem,* 6**,** 1543-1559.

YANG, Z.-M., HOU, S.-C., HUANG, G.-F., DUAN, H.-G. & HUANG, W.-Q. 2014. Electrospinning preparation of p-type NiO/n-type CeO2 heterojunctions with enhanced photocatalytic activity. *Materials Letters,* 133**,** 109-112.

© University of Pretoria

YE, Z., KONG, L., CHEN, F., CHEN, Z., LIN, Y. & LIU, C. 2018. A comparative study of photocatalytic activity of ZnS photocatalyst for degradation of various dyes. *Optik,* 164**,** 345-354.

YI, S., YUE, X., XU, D., LIU, Z., ZHAO, F., WANG, D. & LIN, Y. 2015. Study on photogenerated charge transfer properties and enhanced visible-light photocatalytic activity of p-type Bi 2 O 3/n-type ZnO heterojunctions. *New Journal of Chemistry,* 39**,** 2917-2924.

YU, J., ZHANG, J. & LIU, S. 2010. Ion-exchange synthesis and enhanced visible-light photoactivity of CuS/ZnS nanocomposite hollow spheres. *The Journal of Physical Chemistry C,* 114**,** 13642-13649.

YU, S., LIU, J., ZHU, W., HU, Z.-T., LIM, T.-T. & YAN, X. 2015. Facile room-temperature synthesis of carboxylated graphene oxide-copper sulfide nanocomposite with high photodegradation and disinfection activities under solar light irradiation. *Scientific reports,* 5**,** 16369.

ZELEKEW, O. A. & KUO, D.-H. 2016. A two-oxide nanodiode system made of double-layered p-type Ag 2 O@ n-type TiO 2 for rapid reduction of 4-nitrophenol. *Physical Chemistry Chemical Physics,* 18**,** 4405-4414.

ZHANG, H., WANG, Z., ZHANG, J. & DAI, K. 2023. Metal-sulfide-based heterojunction photocatalysts: Principles, impact, applications, and in-situ characterization. *Chinese Journal of Catalysis,* 49**,** 42-67.

ZHANG, H., ZHANG, Z., LIU, Y., FANG, X., XU, J., WANG, X. & XU, X. 2021. Band-Gap engineering: a new tool for tailoring the activity of semiconducting oxide catalysts for CO oxidation. *The Journal of Physical Chemistry Letters,* 12**,** 9188-9196.

ZHANG, L., GE, L., DENG, L. & TU, X. 2022a. Dual Application: p-CuS/n-ZnS Nanocomposite Construction for High-Efficiency Colorimetric Determination and Photocatalytic Degradation of Tetracycline in Water. *Nanomaterials,* 12**,** 4123.

ZHANG, W., LI, L., ZHANG, X., LIU, H., AN, Y., ZHONG, Y., HU, Z., SHAN, X., WU, J. & WHITE, M. 2022b. Adsorption of Zn (II) on amination@ wood-aerogel and high-value reuse to ZnO/ZnS as an efficient photocatalyst. *Journal of Materials Chemistry A,* 10**,** 18644-18656.

ZHANG, Z., SHAO, C., LI, X., WANG, C., ZHANG, M. & LIU, Y. 2010. Electrospun nanofibers of p-type NiO/n-type ZnO heterojunctions with enhanced photocatalytic activity. *ACS applied materials & interfaces,* 2**,** 2915-2923.

ZHENG, X., WANG, L., ZHOU, Y., LUO, M., LI, H., BO, Z., ZHENG, W., CHANG, C., WEN, J. & DONG, J. 2023. In-situ synthesis of NiS-modified MgO/S-doped biochar for boosting the adsorption-photocatalytic activity. *Journal of Industrial and Engineering Chemistry*.

ZHENG, X., ZHOU, Y., PENG, H., WEN, J. & LIU, Y. 2021. Efficient solar-light photocatalytic activity of FeS/S-doped MgO composites for tetracycline removal. *Colloids and Surfaces A: Physicochemical and Engineering Aspects,* 626**,** 127123.

© University of Pretoria

© University of Pretoria